UNIVERSITY OF CALIFORNIA SAN DIEGO

# Improved wave runup forecasts using remote observations and numerical models

A dissertation submitted in partial satisfaction of the
requirements for the degree Doctor of Philosophy

in

Oceanography

by

Athina Maya Zoé Lange

Committee in charge:

Mark A. Merrifield, Chair
Grant Deane
Julia Fiedler
Sarah Giddings
Robert T. Guza
Ryan Kastner

2023

The Dissertation of Athina Maya Zoé Lange is approved, and it is acceptable in quality and form for publication on microfilm and electronically.

University of California San Diego

2023

DEDICATION

To Papa and Mama.

# EPIGRAPH

Research is making mistakes, finding them, fixing them, and moving on.

There are an infinite number of ways to say the same thing.

*Guza*

TABLE OF CONTENTS

LIST OF FIGURES

LIST OF TABLES

ACKNOWLEDGEMENTS

To Papa, I would have never made it to this point without the tireless number of hours you've spent with me, teaching me math, history, geography as a 7 year old who wanted to be doing anything else every night, to helping me be comfortable going to school in Germany, to guiding me to a path in physics and to the countless hours you have supported me during this PhD, whether it's going to the beach with the Zoé rode, figuring out the linear algebra of photogrammetry over Christmas, to teaching me about neural networks. You always said the beach would be far away one day, but somehow I've ended up right back at that very same beach. To Mama, for being my support system my whole life, for listening to me talk about my work and rereading everything I've written. I appreciate everything you've done behind the scenes.

Thank you to Mark, Guza and Julia for all your time and energy that you have put into teaching me and helping me to grow as a person and scientist. I am so thankful for all of your support and belief in me. Guza, your emails, with their pockets of cultural references, wisdoms and inside jokes has never failed to make me smile. Julia, without you I would have been stuck in so many rabbit holes and your endless willingness to help me has been incredible. Mark, thank you for trusting in me and letting me explore what I wanted to do.

To the whole field crew, thank you for all the tireless work you all do to get our remarkable datasets. When we asked for 25 instruments to be deployed and weekly surveys for RuBy2D, none of you balked and we got an incredible dataset. And a special thank you to Rob, you have always been so willing to help answer any of my drone or imagery questions, I would not have been able to get the data I needed without your incredible help.

Thank you to my PhD cohort, for all the fun adventures we've had and all the support you've given me. Thank you to our Local Support Group 301, without which I don't think anyone of us would have gotten through the first year. Thank you to our

Wednesday crew, for all the fun chats and baked goods throughout the years and especially to Duncan for being my rubber duck throughout this whole process.

Chapter 2, in full, is a reprint of the paper "Estimating runup with limited bathymetry" published in Coastal Engineering by A.M.Z. Lange, J.W. Fiedler, J.M. Becker, M.A. Merrifield and R.T. Guza in 2022. The dissertation author was the primary investigator and author of this paper.

Chapter 3, in full, has been submitted for publication as it may appear in Coastal Engineering 2023. A.M.Z. Lange, J.W. Fiedler, M.A. Merrifield, and R.T. Guza. The dissertation author was the primary investigator and author of this paper.

Chapter 4, in part, is currently being prepared for submission for publication of the material. A.M.Z. Lange, J.W. Fiedler, M.A. Merrifield, and R.T. Guza. The dissertation author was the primary investigator and author of this material.

## VITA

| | |
|---|---|
| 2018 | Bachelor of Science, Theoretical Physics - University College Dublin, Ireland |
| 2019 | Master of Science, Oceanography - University of California San Diego, USA |
| 2023 | Doctor of Philosophy, Oceanography - University of California San Diego, USA |

## PUBLICATIONS

*Relating Offshore Wave Conditions to Incident Waves and Shoreline Water Levels at Ipan, Guam during Extreme Events* Lange, A.M.Z.; Becker, J.M.; Merrifield, M.A.; Behres, J.; and Terrill, E. Ocean Sciences Meeting 2020, San Diego, CA

*An early warning system for wave-driven coastal flooding at Imperial Beach, CA* Merrifield, M.A.; Johnson, M.; Guza, R.T.; Fiedler, J.W.; Young, A.P.; Henderson, C.; Lange, A.M.Z.; O'Reilly, W.C.; Ludka, B.C.; Okihiro, M.; Pappas, K.; Engeman, L.; Behrens, J.; and Terrill, E. Natural Hazards (2021)

*Estimating runup with limited bathymetry* Lange, A.M.Z.; Fiedler, J.W.; Becker, J.M.; Merrifield, M.A.; and Guza, R.T. Coastal Engineering (2022) 172

*Estimating surfzone bathymetry remotely* Lange, A.M.Z.; Fiedler, J.W.; Merrifield, M.A.; and Guza, R.T. Ocean Sciences Meeting 2022

*UAV video-based estimates of nearshore bathymetry - Combining cBathy and timestacks* Lange, A.M.Z.; Fiedler, J.W.; Merrifield, M.A.; and Guza, R.T. CIRN Workshop 2023, Duck, NC

*UAV video-based estimates of nearshore bathymetry* Lange, A.M.Z.; Fiedler, J.W.; Merrifield, M.A.; and Guza, R.T. *in review Coastal Engineering*

ABSTRACT OF THE DISSERTATION

Improved wave runup forecasts using remote observations and numerical models

by

Athina Maya Zoé Lange

Doctor of Philosophy in Oceanography

University of California San Diego, 2023

Mark A. Merrifield, Chair

The accuracy of flood forecasting models depends crucially on understanding wave runup. I use theory, insitu and remote observations, numerical modeling, computer vision, and deep learning to (1) investigate numerically the runup dependence on bathymetry and incident wave conditions, (2) improve video-based bathymetry estimates, and (3) characterize infragravity waves in 10m depth, for use in boundary conditions of runup models. Implementation into operational runup observing systems and models is ongoing.

A numerical modeling (SWASH) study used 138 hindcast historical storm waves, two offshore boundary conditions, and 24 representative eroded beach bathymetries from a Southern California beach. The runup 2% exceedance level varied by more than 30% in

response to changes in bathymetry or infragravity wave boundary conditions. An empirical parameterization trained on this dataset includes both a foreshore beach slope $\beta_f$ and an effective mid-surfzone slope $\beta_{eff}$ (Chapter 2, Lange et al., 2022). Subaqueous bathymetry is usually unknown because of the large expense of insitu jetski surveys, but $\beta_f$ and $\beta_{eff}$ can be estimated approximately and cost-effectively from images.

The new 2-slope runup models have smaller errors than 1-slope models, but lack generality and have fundamentally limited accuracy. I show that useful bathymetry can be extracted from video collected during a single 17-minute quadcopter hover. The existing cBathy algorithm is extended with a crest-tracking algorithm that significantly reduces large cBathy errors near the breakpoint. The crest-tracking algorithm uses a deep-learning neural network to annotate timestacks for celerity estimates, and the depth inversion includes a nonlinear correction. This approach reduces RMSE surfzone depth errors to 0.17m, from $\sim$ 0.81m with cBathy (Chapter 3, Lange et al. 2023, revision submitted to Coastal Engineering).

The infragravity offshore ($\sim$10m depth) boundary condition is another potential error source in the runup model estimates. Several years of observations show that free infragravity waves are often much larger (up to x10) than the bound waves often used as a boundary condition. A parameterization of the incident-free IG wave field is combined with the predicted boundwave energy into a sea surface elevation timeseries of the incident IG energy suitable for use in numerical models (Chapter 4).

# Chapter 1

# Introduction

Around 250 million people living in low-lying coastal areas could be affected by rising sea levels and increasingly frequent inundations during storms (Kulp, Strauss, 2019). Accurate wave runup predictions are an invaluable part of early warning flood forecasting systems or flood mapping that enables precautionary measures to be taken (Stephens, Cloke, 2014; Stokes et al., 2019; Jordi et al., 2019; Stokes et al., 2021; Merrifield et al., 2021; FEMA, 2021; USGS, 2022).

The thesis goal is to develop methods that improve the presently limited skill of runup and overtopping forecasts in Southern California. Each of the three thesis chapters is a self-contained research paper with a literature review and extensive references. Key concepts, wave runup, nearshore bathymetry and infragravity waves, are now reviewed briefly.

## 1.1 Wave runup

Wave runup is the maximum elevation of the uprush from individual waves at the shoreline (Figure 1.1). Breaking waves transfer mean momentum into the water column, elevating the mean water level (wave setup $\eta$, Longuet-Higgins, Stewart (1964)). Wave energy is partially dissipated by wave breaking but some reaches the shoreline and oscillates (swash) around the wave setup (Miche, 1951; Guza, Thornton, 1982; Battjes,

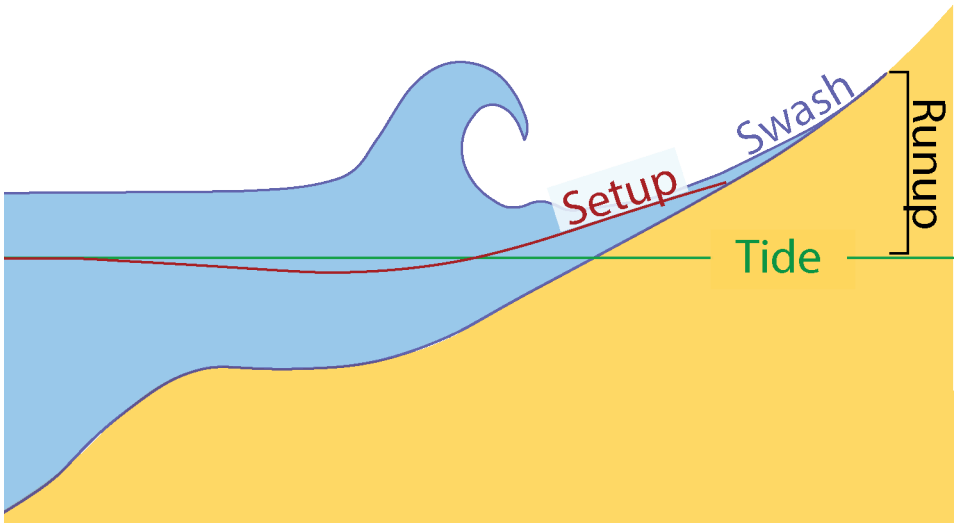


**Figure 1.1.** Schematic of wave runup at the shoreline. The still water level is affected by the tide and sea-level anomalies such as storm surge and climatic cycles. Breaking waves force an elevated water level (setup) with a maximum at the shoreline. Wave runup is measured as a vertical elevation.

1988; Martins et al., 2018). Swash oscillations on ocean beaches can be energetic at periods of incident sea-swell waves ($4 < T_p < 25$s) and at longer 'infragravity' periods ($25 < T_p < 250$s) (Stockdon et al., 2006). The flooding potential of an irregular wave field during a given time period is often quantified with $R_{2\%}$, the vertical elevation exceeded by 2% of maximum runup from individual waves (FEMA, 2021). Assuming Gaussian statistics, $R_{2\%,G}$ from waves equals the mean elevation (wave setup, $\eta$) plus two standard deviations of the vertical swash oscillations:

$$R_{2\%,G} = \eta + S/2 \qquad S = \sqrt{S_{IG}^2 + S_{SS}^2}, \tag{1.1}$$

where $S_f = 4 * \sqrt{\int_f E_{runup}(f)df}$, $E_{runup}(f)$ is the runup energy spectrum, separated into infragravity (IG) [$0.004 < f < 0.04$Hz] and sea-swell (SS) [$0.04 < f < 0.25$Hz] frequency bands. The 0.04Hz limit includes long swell sometimes present in Southern California (Okihiro et al., 1992; Fiedler et al., 2018).

There are different ways to estimate either wave runup or $R_{2\%}$. Given the beach profile and incident wave conditions, wave runup time series can be obtained with computationally intensive numerical models, such as SWASH (Guimarães et al., 2015; Nicolae Lerma et al., 2017; Liu et al., 2021) or XBeach (Gallien, 2016; Beer de et al., 2021; Roelvink et al., 2018). In wave flumes (Ruju et al., 2014, 2019), or on relatively featureless bathymetry with weak alongshore variations (Fiedler et al., 2018; Henderson et al., 2022) numerical models can accurately predict runup. However, these numerical models require bathymetry (extending from above the waterline across the surf zone to offshore) that can change over time and is rarely available. Furthermore, the spectral properties of waves incident to the beach from deep water (a model boundary condition) are usually known only approximately. Runup overtopping warnings are therefore often driven with numerically simple empirical parameterizations of $R_{2\%,G}$, that require only a shoreline beach slope and bulk incident wave statistics readily obtained from buoys (Behrens et al., 2019) or regional wave forecasts.

Hunt (1959) related runup to offshore wave height and wavelength $H_0$ and $L_0 = \frac{g}{2\pi}T_p^2$ respectively and a linear slope $\beta$, by $R \sim \beta\sqrt{H_0 L_0}$. The most widely used empirical equation, Stockdon et al. (2006), retains the $H_0 L_0$ variable of Hunt, with individual parameterizations for setup, IG and SS swash

$$R_{2\%,G} = 1.1\left(H_0 L_0\right)^{0.5}\left(0.35\beta_f + \frac{1}{2}\left[0.004 + 0.56\beta_f^2\right]^{0.5}\right), \tag{1.2}$$

where $\beta_f$ is the beach slope in the swash zone. Many other, sometimes conflicting, parameterizations use different (from Eq. 1.2) dependencies on $H_0$, $L_0$, and $\beta$, (non-exhaustive lists are given in Silva Gomes da et al., 2020; O'Grady et al., 2019; Dodet et al., 2019). A recent parameterization (IPA, Fiedler et al. (2020)) replaces the incident wave bulk parameter $\sqrt{H_0 L_0}$ with a frequency-weighted integral $\int_{SS} E_{offshore}(f)^a f^b df$ that includes additional information about the incident wave spectral shape. Many empirical runup

models use only the foreshore slope $\beta_f$ but others use the offshore slope. The constants $(a, b)$ are determined using the numerical wave model SWASH. A parameterization developed in Chapter 2 uses both foreshore and surf zone slopes.

## 1.2 Bathymetry

Bathymetry, the water depth relative to NAVD88 in the current work, defines the subaqueous terrain. While the effect of bathymetry on surf zone processes and in turn on wave runup is at least partially understood using numerical and empirical models, natural bathymetry is difficult to observe. Sandy beach bathymetry can change on timescales ranging from hourly (e.g. during storm events, Seymour et al., 2005; Henderson et al., 2022) to seasonally. San Diego subaerial beaches are typically narrow (eroded) in winter and wider in summer, (Aubrey, 1979; Larson, Kraus, 1994; Yates et al., 2009), but also vary inter-annually in response to El Niño (Ranasinghe et al., 2004; Ruggiero et al., 2016; Doria et al., 2016; Young et al., 2018).

Sandbars, ubiquitous on sandy beaches, affect runup. However, bars move on-offshore and grow and decay over times as short as a few days (Thornton et al., 1996; Gallagher et al., 1998; Hoefel, 2003; Bender, Dean, 2003; Trombetta et al., 2020). Sandbars are poorly understood, and monitored quantitatively at a handful of sites worldwide. Model predictions of beach profile evolution are generally inaccurate. The lack of accurate (historical, real-time, and forecast) bathymetry necessarily reduces the skill of runup models hindcasts and forecasts.

For a given set of incident wave conditions, bathymetry controls the evolution of waves and wave-driven currents across the surf and swash zone. Focusing of wave energy in certain areas can, for example, lead to pronounced flooding during storms on some streets in Imperial Beach, CA, while neighboring streets remain dry (Merrifield et al., 2021).

Shallow, subaqueous nearshore bathymetry can be measured with a jet ski equipped

with acoustic sonar, sea surface thermistor, and GNSS-RTK (Global Navigation Satellite System - Real-time Kinematic) antenna (Ludka et al., 2019). However, jet ski surveys are labor intensive, restricted to daylight and low-moderate waves, require meticulous and expensive attention to hardware maintenance, and can be halted by poor water quality (Merrifield et al., 2021; Henderson et al., 2022).

Remote sensing is an attractive alternative to insitu bathymetry measurements. Remote methods include data from satellites (Vanderstraete et al., 2003; Mallet, Bretar, 2009; Gao, 2009; Jing, Datt, 2010; Abileah, Trizna, 2010; Hodúl et al., 2018; Zuckerman, Anderson, 2018; Legleiter, Harrison, 2019; Li et al., 2019; Geyman, Maloof, 2019), fixed-wing airplanes, small drones and quadcopters, and fixed (ground-based) instruments mounted with LiDAR (Irish, White, 1998; Fiedler et al., 2021; Martins et al., 2023), hyperspectral imagery (Sandidge, Holyer, 1998; Ma et al., 2014; Maas et al., 2019; Alevizos, 2020) or cameras (Stockdon, Holman, 2000; Holman, Stanley, 2007; Catálan, Haller, 2008; Wengrove et al., 2013; Bergsma et al., 2016; Brodie et al., 2019; Stringari, Power, 2019; Tsukada et al., 2020; Holman, Bergsma, 2021). In clear water, bathymetry can be directly obtained with LiDAR or hyperspectral imaging. However, in Southern California, as well as many other coastal regions, the water is too opaque to usefully observe the bottom. A thesis goal is to improve the accuracy of remotely sensed bathymetry.

In recent decades, camera images of the runup and sea surface are increasingly used for low-cost near-continuous nearshore monitoring. Fixed camera stations have been used to observe runup, beach topography and bathymetry (Holman, Haller, 2013, , and references therein). Two surface signatures used for depth estimation from RGB (red-green-blue) imagery are wave dissipation and wave celerity.

Wave dissipation methods are applied to time-average images, such as *timex* image products from ARGUS stations (5-camera fixed systems, Holman, Stanley, 2007) and the high-intensity peaks are correlated to depth-limited wave breaking. Although useful for studying sandbar morphology evolution qualitatively, the depth profiles needed in runup

models are not estimated. Dissipation patterns can be used in data assimilation models, by comparing them to patterns computed by numerical models on a known bathymetry and updating said bathymetry (Aarninkhof, 2005; Dongeren van et al., 2008). These model- and observation-intensive approaches are not pursued here.

Alternate methods obtain a bathymetry estimate by exploiting the dependency of wave celerity ($c = \omega/k$) on depth as given by the linear dispersion relation ($\omega^2 = gk \tanh(kh)$) (Suhayda, Pettigrew, 1977; Catálan, Haller, 2008; Yoo et al., 2011; Stringari, Power, 2019). cBathy (Holman et al., 2013) fits wavenumber EOFs to Fourier transformed pixel intensity timeseries (Stockdon, Holman, 2000; Plant et al., 2009; Wengrove et al., 2013; Radermacher et al., 2014; Bergsma et al., 2016; Rutten et al., 2017; Bergsma et al., 2019; Holman, Bergsma, 2021; Rodríguez-Padilla et al., 2022). Other work obtains the mean celerity using a cross-correlation technique (Almar et al., 2009; Bergsma et al., 2019; Tsukada et al., 2020).

## 1.3 Infragravity Waves

Infragravity waves were first observed by Munk (1949) and Tucker (1950) as long-period undulations lagging behind the higher-frequency sea-swell wave groups, with an amplitude proportional to the incident waves, and named 'surf beats'. Since then, multiple theories on the generation mechanisms of these waves have been put forth, including Longuet-Higgins, Stewart (1962, 1964) and Hasselmann (1962) who mathematically showed that in deep and intermediate water depths, SS wave groups that follow the linear dispersion relationship force a 2nd order 'bound wave' at the group frequency that is 180° out of phase with the group and does not follow the linear dispersion relationship. As the wave group propagates into shallow water, the bound wave lags behind the wave group as it is no longer in equilibrium. The increasing shallow water allows for energy to be transferred from the incident sea-swell frequencies of the group to lower (IG) frequencies through

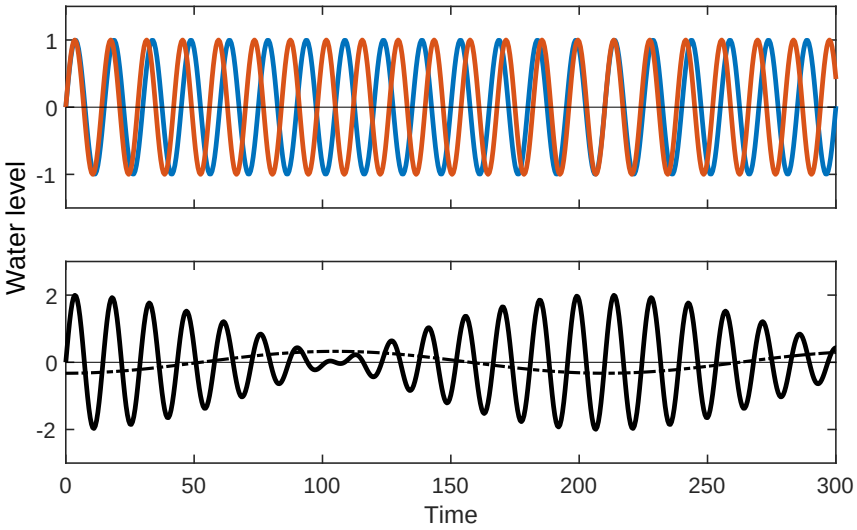


**Figure 1.2.** Schematic of an infragravity bound wave propagating over a flat bottom. (Upper) Time series of two sinusoidal waves with periods of 15s (blue) and 14s (orange). (Lower) Short-wave sea surface elevation (solid) and resulting (scaled) boundwave (dashed) (figure adapted from Bertin et al. (2018), and using Hasselmann (1962) theory).

nonlinear triad difference interactions (Hasselmann, 1962; Herbers, Burton, 1997).

This shoreward propagating IG wave, considered 'free' because it approximately satisfies the free-wave dispersion relation, can reflect at the shore and propagate seaward (Sheremet et al., 2002). These reflected IG waves, given a certain combination of frequency and direction, are trapped in the nearshore due to refraction and can propagate up- and down-coast and decay offshore (Okihiro et al., 1992; Herbers et al., 1995b). The free IG waves that are not trapped can radiate seaward past the continental shelf ('leaky waves') and are able to propagate across deep water (Ardhuin et al., 2014; Rijnsdorp et al., 2021). These deep-water IG waves can contribute to the total incident IG waves at a different site, particularly evident on low-energy swell days (Webb et al., 1991; Herbers et al., 1995b; Sheremet et al., 2002).

## 1.4 Research Outline

The goal of this thesis is to improve the accuracy of runup estimates on sandy San Diego County beaches by incorporating bathymetric information obtained from remote imaging and an observation-driven infragravity wave boundary condition. This is done in the following chapters:

Chapter 2: Estimating runup with limited bathymetry

*Research questions*: What is the effect of poorly known bathymetry on runup models? How can limited bathymetric information be incorporated into empirical wave runup models?

*Approach*: Numerical modeling isolates the effects of different bathymetries on runup with identical incident waves A parameter describing the subaqueous bathymetry is determined and incorporated into the empirical models.

Chapter 3: UAV video-based estimates of nearshore bathymetry

*Research questions*: Can remotely sensed bathymetry estimates be improved. particularly in the dynamic surf zone region?

*Approach*: Video imagery from Uncrewed Aerial Vehicles (UAVs) at Torrey Pines and Cardiff, CA is used to develop an improved method that combines the cBathy algorithm (Holman et al., 2013) and new crest-tracking methods from timestack imagery.

Chapter 4: Free infragravity waves on the inner shelf: Observations and Parameterizations at two Southern California beaches

*Research questions*: What is the distribution of bound versus free IG waves at the wave model offshore boundary ($\sim$ 10m)? How can this distribution be

parameterized as a function of the incident SS wave field, and what does this imply about the generation mechanisms and source of the IG waves? How can the 2D distribution of IG energy be incorporated into the SWASH 1D numerical model?

*Approach*: Use pressure and velocity measurements at two locations in San Diego County and IG wave theory to determine the ratio of bound to free IG energy, during energetic storm conditions as well as low incident sea-swell energy conditions.

# Chapter 2

# Estimating runup with limited bathymetry

## 2.1 Abstract

Wave runup estimates are used in erosion and overtopping models, and in coastal structure design. However, runup depends on often incompletely known surf and swash bathymetry. The many existing runup parameterizations characterizing bathymetry with only the foreshore (swash zone) beach slope $\beta_f$ are necessarily of limited accuracy. Here, an empirical model relating runup to incident wave spectra is extended to include an effective, mid-surf zone slope, $\beta_{\text{eff}}$, that depends on the cross-shore location of the midpoint of breaking-wave dissipation. The empirical model is trained using numerical simulations (SWASH) of 138 hindcast historical storm waves, two different offshore infragravity wave boundary conditions, and 24 representative eroded beach bathymetries from a Southern California beach. The model is tuned for the swell waves and concave up (sometimes barred) depth profiles characteristic of the study region. Consistent with their generation by surf zone-wide processes, setup and infragravity runup depend more strongly on surf zone $\beta_{\text{eff}}$ than on foreshore $\beta_f$. In contrast, sea-swell runup depends more strongly on shoreline processes, and $\beta_f$ is more important than $\beta_{\text{eff}}$. Empirical model accuracy is improved by including both $\beta_{\text{eff}}$ and $\beta_f$.

## 2.2 Introduction

Wave runup, the maximum elevation of the uprush of water at the shoreline, is determined by surf zone and shoreline processes. Breaking waves transfer momentum into the water column, elevating the mean water level (wave setup, Longuet-Higgins, Stewart, 1964). Some wave energy reaches the shoreline and oscillates (swash) around the setup. Swash oscillations on ocean beaches can occur at the periods of incident sea-swell (SS) waves and also at longer "infragravity" (IG) periods (Battjes, 1974; Suhayda, 1974; Huntley, 1976).

For a given set of incident wave conditions, bathymetry controls the evolution of waves across the surf and swash zones, and the resulting shoreline setup and swash. The effects of bathymetry on setup (Stephens et al., 2011), infragravity swash (Cox et al., 2013) and total runup (Cohn et al., 2014; Silva Gomes da et al., 2020) have been investigated using multiple barred profiles and a range of forcing conditions in numerical models. Bar crest depth influences setup, with shallower bars generating higher setup levels (Stephens et al., 2011). In cases where waves break seaward of the bar, the IG swash was reduced when compared to runs of the same forcing and with no bars (Cox et al., 2013). Raubenheimer et al. (2001) showed the effect of shallow bars on setup varies with tide. Runup debris lines observed on 10+ beaches, for each of two storm events ($H_0 \sim 8.5$ and 10.7m), suggest $R_{max} \sim \beta_{sz}^{2/3}$ (Mather et al., 2011) where $\beta_{sz}^{2/3}$ is the average slope from the shoreline to the 15m depth contour (approximately the surf zone slope for these storm waves). Using observations of runup and the corresponding bathymetry to improve runup parameterizations, Silva Gomes da et al. (2019) created three different empirical equations for dissipative, intermediate and reflective sandy beaches (each with their own characteristic nearshore bathymetry). Because natural subaqueous bathymetry and wave conditions each span a wide range, their combined effect on runup has not been generalized. Empirical formulas are only reliably valid within their calibration range, and

in many calibration cases important observational details (e.g. surf zone bathymetry, incident wave frequency spectra) are unknown. Silva Gomes da et al. (2020) show that unknown subaqueous bathymetry is likely responsible for much of the scatter between bulk parametric models (e.g. Stockdon et al., 2006) about observations from a wide range of settings, and that information about the beach state could improve the skill of the predictor.

Although the importance of surf zone bathymetry is widely acknowledged, most empirical runup models include only the swash zone (e.g. foreshore) beach slope, $\beta_f$. Hunt (1959) related runup $R$ to offshore wave height $H_0$, deep water wavelength $L_0 = \frac{g}{2\pi}T_p^2$ at the peak wave period, and a linear slope $\beta$

$$R \sim \beta \left(H_0 L_0\right)^{0.5}. \tag{2.1}$$

Irregular wave field runup is often expressed as $R_{2\%}$, the vertical level exceeded by 2% of the runup. With runup energy spectra $E_r(f)$ and Gaussian statistics, $R_{2\%,G}$ is the mean setup ($\eta$) plus two standard deviations of the vertical runup time series $S$:

$$R_{2\%,G} = \eta + \frac{S}{2} \quad \text{with} \quad S = \left(S_{IG}^2 + S_{SS}^2\right)^{0.5}, \tag{2.2}$$

where $S = 4\left(\int E_r df\right)^{0.5}$, separated into infragravity (IG) [$0.004 \leq f < 0.04$] and sea-swell (SS) [$0.04 \leq f < 0.25$] frequency bands (Holman, Sallenger, 1985; Holman, 1986; Vousdoukas et al., 2012; Atkinson et al., 2017). The 0.04Hz limit is selected to include long swell in the SS band. A widely used empirical equation (S06, Stockdon et al., 2006) has individual parameterizations for setup, IG swash, and SS swash, respectively:

$$R_{2\%,G} = 1.1\left(H_0 L_0\right)^{0.5}\left(0.35\beta_f + \frac{1}{2}\left[0.004 + 0.56\beta_f^2\right]^{0.5}\right). \tag{2.3}$$

The foreshore beach slope, $\beta_f$, is defined as the average slope between the mean plus or

minus two standard deviations of the vertical runup. Each term in Eq. 2.3 depends on $H_0 L_0$, and $\eta$ and $S_{SS}$ also depend on $\beta_f$. Many variants of Eq. 2.3 have been developed, often based on different definitions of the independent variables and tuned to different bathymetries and wave conditions. For example, $L_0$ is commonly based on the mean wave frequency or mean period, rather than the peak (O'Grady et al., 2019; Dodet et al., 2019; Silva Gomes da et al., 2020, and references therein). While the more readily available $\beta_f$ is prevalent, previous studies have used alternative slopes, such as a surf zone slope in setup (Raubenheimer et al., 2001, and others) and maximum uprush (Mather et al., 2011). IG runup is independent of $\beta_f$ in some studies (e.g. Stockdon et al., 2006; Hughes et al., 2014; Fiedler et al., 2020) and slope dependent in others (e.g. Ruggiero, 2004; Thomson et al., 2006). In contrast, the strong dependence of SS on $\beta_f$ is well estabilished (Miche, 1951; Hunt, 1959; Battjes, 1974; Huntley et al., 1977; Hughes et al., 2018, and many others). The bulk offshore wave height $H_0 \approx 4\left(\int E(f)df\right)^{0.5}$ does not include the incident wave spectral shape, leading to sometimes large errors with bimodal or broad offshore spectra (Oorschot van, d'Angremond, 1968; Almeida et al., 2017). Below, models using $H_0$ and $L_0$ (or similar) as independent variables (sometimes squared or in other functions) will be referred to as "Bulk" parametric models.

Fiedler et al. (2020) replaced $H_0$ and $L_0$ (Eq. 2.3) as separate variables with a single frequency-weighted energy spectra, the integrated power law approximation (IPA).

$$R_{2\%,G} = \eta + 2\left(E_{IG} + E_{SS}\right)^{0.5} \tag{2.4}$$

$$\text{with} \quad \left[\int \eta, E_{IG}, E_{SS}\right]_{shoreline} = \left[\alpha\beta_f \int_{SS} E^m(f) f^n df\right]_{deep},$$

where $\beta_f$ is the foreshore slope, and the parameters $\alpha, l, m$, and $n$ are chosen to maximize model skill, $R^2 = 1 - \frac{\sum_{i=1}^{n}(p-o)^2}{\sum_{i=1}^{n}(o-\bar{o})^2}$ where $p$ is the parameterization-predicted value and $o$ the SWASH-modeled value ('observed'). The units of $\alpha$ are set to give m and $m^2$ for the

setup and swash terms respectively. Frequency-weighted energy spectral models (Eq. 2.4) will be referred to as "IPA" (integrated power approximation). The best-fit IPA using the numerical runup model SWASH (reviewed below), historical waves and a single winter subaqueous bathymetry at Imperial Beach, CA (Fiedler et al., 2020), is

$$R_{2\%,G} = 0.21 \int_{SS} E^{0.55} f^{-1.05} df + 2 \left[ 0.04 \int_{SS} E^{1} f^{-1} df + 0.99 \beta_f^2 \int_{SS} E^{0.45} f^{-1.85} df \right]^{0.5}. \tag{2.5}$$

Optimal IPA $(m, n)$ values (Eq. 2.5) indicate a linear or weaker ($m$ between 0.45 and 1) dependence of $R_{2\%,G}$ on $E$, and an inverse or stronger ($n$ between $-1$ and $-2$) dependence on $f$, qualitatively consistent with $H_0 L_0 \sim E^{0.5} f^{-2}$ (Eq. 2.3). The S06 (Eq. 2.3) and IPA estimates (Eq. 2.5) of SS swash have the same $\beta_f^2$ dependence, and neither IG swash term depends on $\beta_f$. However, the S06 estimate (Eq. 2.3) of setup depends linearly on $\beta_f$, whereas the IPA setup (Eq. 2.5) does not. An IPA model using $\sim \int_{SS} E^{0.5} f^{-2} df$ for IG and SS swash had skill only slightly lower than optimal (Eq. 2.5). The S06 skill was (of course) improved by calibration to these simulations, but IPA-type models (Eq. 2.5) had higher skill than a bulk-type model (Eq. 2.3), suggesting the utility of IPA in accounting for spectral shape. The IPA (Eq. 2.5) was developed as a storm wave runup model for the swell-dominated wave climates typical of Southern California. It is currently used in the overtopping forecasts for Imperial Beach with a modeled $\beta_f$ (https://climateadapt.ucsd.edu/imperialbeach/forecast/).

Here, the effect on $R_{2\%}$ of varying surf zone bathymetry, in addition to foreshore slope, is assessed. The range of modeled waves and bathymetry is restricted to plausible storm conditions for the study region. Eight observed subaqueous winter bathymetries, each with three foreshore beach slopes, are coupled with 138 hours of model storm waves to create 6624 runup simulations using the SWASH numerical model. Both bulk $H_0 L_0$ (Eq. 2.3) and IPA integral (Eq. 2.5) parameterizations are improved by including an effective, mid-surf zone slope $\beta_{\text{eff}}$. The variation in runup between different (observed) winter profiles

with equal $\beta_f$ are differentiated by $\beta_{\text{eff}}$. Section 3.3 describes the bathymetries, waves and SWASH model used for runup simulations. In Section 3.4, $\beta_{\text{eff}}$ is included in runup empirical models. Section 3.5 is a discussion of the applicability and limitations of this study.

## 2.3 Methods

### 2.3.1 Bathymetries

Quarterly bathymetric and monthly subaerial LiDAR surveys at Imperial Beach began in November 2008 (Ludka et al., 2019). The study transect offshore of Cortez Avenue (MOP D0045, Ludka et al., 2019) has been surveyed 119 times. Eight representative winter profiles (between November and February) are selected to use in the numerical modeling study (Figure 2.1). The profiles include an offshore sandbar (2009-2010 El Niño) and range from shallow (blue) to eroded (red). These constructed profiles rejoin offshore at $(x, z) = (-433\text{m}, -8.4\text{m})$ and extend with constant slope 0.01 to $h = -15\text{m}$ (NAVD88), where SWASH is initialized for all profiles. The subaqueous bathymetries rejoin onshore at $x = 0\text{m}$, and foreshore bathymetry $\beta_f$ is varied for each offshore bathymetry. Three concave foreshore profiles are used: (1) a LiDAR-derived profile from the January 2019 storm described in Fiedler et al. (2020) ($\beta_f \approx 0.1$), (2) the average eroded profile used for calibration in Fiedler et al. (2020) ($\beta_f \approx 0.08$) and (3) a surveyed profile from February 15th, 2018 ($\beta_f \approx 0.05$), similar to the average observed beach slope at Cortez Avenue (Figure 2.1). The foreshore beach is extended linearly above $x = 5\text{m}$ to prevent overtopping in the numerical model. All simulations are applied at mean higher high water (MHHW).

### 2.3.2 Incident Waves

Using a subset of the wave conditions with potential for overtopping from Fiedler et al. (2020), the wave forcing for the SWASH simulations (Figure 2.2) consists of 138

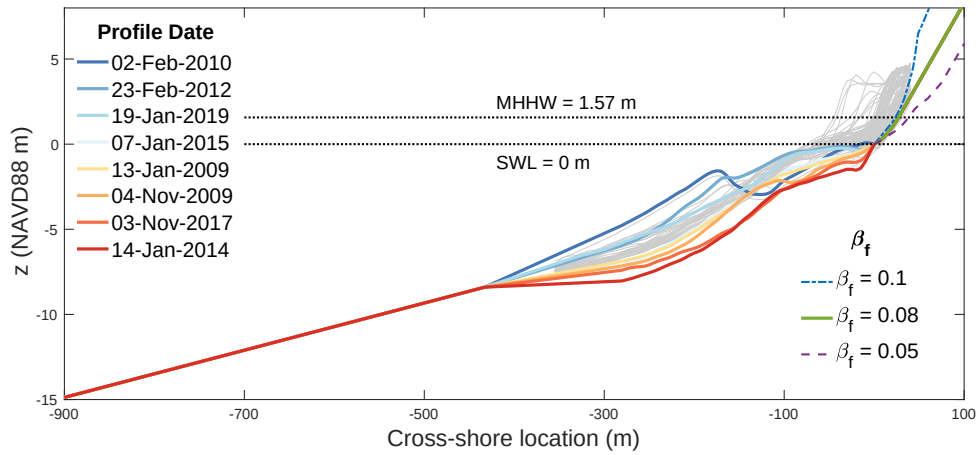


**Figure 2.1.** Depth (NAVD88) versus cross-shore distance at Cortez Avenue, Imperial Beach, CA (MOP line D0045). Subaqueous profiles used in the current study are colored from blue (shallow) to red (eroded), with respective survey dates shown in legend. Three foreshore beach slopes are shown in blue ($\beta_f = 0.1$), green ($\beta_f = 0.08$), and purple ($\beta_f = 0.05$). Subaqueous and subaerial profiles are joined at $(x, z) = (0, 0)$. The historical profiles are shown in gray. The horizontal lines indicate MHHW = 1.57m and SWL = 0m.

spectral estimates extracted from a 20 year hindcast in 10m depth offshore of Cortez Avenue, Imperial Beach (MOPS, O'Reilly et al., 2016). The offshore wave conditions are reverse shoaled to deep water $H_0$ between $1.5 - 4.5$m, $f_p$ between $0.05 - 0.08$Hz, and $(H_0 L_0)^{0.5}$ between $30 - 48$m. Model spectral estimates were applied in 15m depth to avoid initializing the runup SWASH model within the surf zone.

### 2.3.3 SWASH model

SWASH is a phase-resolving numerical model that solves the nonlinear shallow water equations for a depth-averaged, non-hydrostatic free surface flow (Zijlema et al., 2011). In highly controlled laboratory flumes, carefully implemented modern numerical models generally agree well with observed waves and runup (Torres-Freyermuth et al., 2010; Ruju et al., 2014; Bakker de et al., 2014, 2015; Suzuki et al., 2017). In field applications, numerical model assumptions are violated and boundary conditions poorly

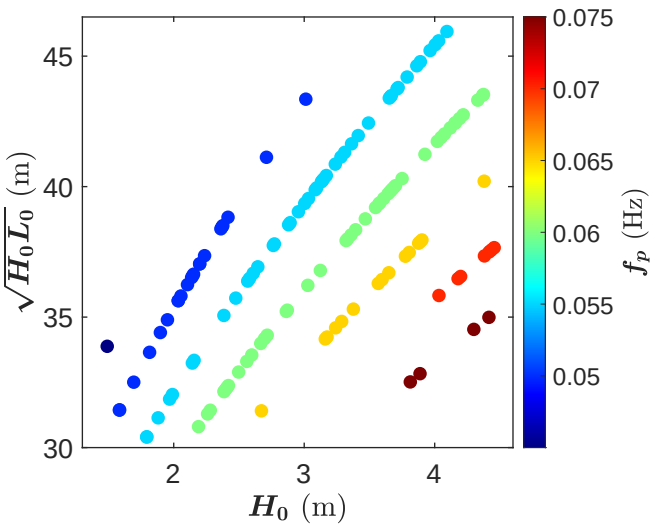


**Figure 2.2.** $(H_0 L_0)^{0.5}$ versus offshore significant wave height $H_0$, colored by peak frequency $f_p$ for 138 MOP wave spectral hindcasts used to force the SWASH model. $H_0$ and deep water wavelength $L_0$ are obtained by reverse-shoaling the wave hindcasts from 10m depth to deep water.

known. Nevertheless, forecast warning systems for beach narrowing, wave overtopping and street flooding must estimate $R_{2\%}$ for changing wave forecasts. Fiedler et al. (2020) developed the IPA, an empirical, computationally simple runup parameterization using SWASH in conjunction with historical waves and bathymetry. That approach is extended here from 1 to 8 offshore bathymetries, and to include a characteristic surf zone slope as well as foreshore slope.

SWASH is run in nonstationary 2D mode, with a curvilinear grid with a 2-m alongshore mesh for two identical parallel transects with 2 vertical layers. Bathymetric profiles are interpolated onto a 2-m cross-shore grid from offshore at $x = -909$m until $x = -507$m, and smoothed to a 0.25m grid on the foreshore. Bottom friction is parameterized using the default Manning formula with coefficient $0.019\text{m}^{-1/3}\text{s}$ and background viscosity $0.1e^{-4}\text{m}^2/\text{s}$. Breaking parameters are $\alpha = 0.6$, $\beta = 0.3$, and $\mu = 0.25$ (Smit et al., 2013). Additional details follow Fiedler et al. (2020).

The modeled tide level is fixed at MHHW (1.57m NAVD88, La Jolla NOAA tide

Station 9410230), as overtopping events at Imperial Beach typically occur when large waves and high tide combine. Model runs are 60 minutes, allowing for 10 minutes of model spin up. The 50 minute records are a compromise between statistical stability and computation time (Fiedler et al., 2018). Cross-shore and vertical runup location time series are calculated with a 10 cm runup threshold depth. Setup is estimated as the mean vertical runup. Swash statistics are estimated from spectra of the detrended vertical runup with 10 minute Hanning windows and 50% overlap. Foreshore beach slopes for parameterizations are the average slope between two runup standard deviations above and below the mean vertical runup line (Stockdon et al., 2006).

The offshore boundary conditions of shoreward propagating SS and IG waves are prescribed in precision 1D laboratory flume studies and observed approximately in a few field studies. Regional waves models (including MOPS, O'Reilly et al., 2016) do not provide reliable IG forecasts. The offshore IG energy in situations where it is unknown have been specified as a theoretical 1D boundwave (Hasselmann, 1962) and with $E_{IG} = 0$. Runup using these offshore boundary conditions tends to converge with the subaqueous bathymetry considered by Fiedler et al. (2019), but can differ substantially in the present cases. Both IG boundary conditions are used here for all test waves and bathymetries, and their difference is treated as noise in the fit between simulations and parameterizations (Section 3.5).

## 2.4 Results

The eight subaqueous and three subaerial bathymetries give a total of 24 profiles, which along with the two IG boundary conditions and 138 forcing conditions, result in 6624 SWASH model runs. For the same $H_0$, $R_{2\%,G}$ can vary by over 2 meters depending on the subaqueous bathymetry (Figure 2.3 g). SS swash differs by more than a factor of 2 with the lowest and highest $\beta_f$ (Figure 2.3 f) consistent with parameterizations (Eq. 2.3

and 2.5). In contrast, SWASH-simulated IG swash and setup $\eta$ do not separate by $\beta_f$ (Figure 2.3 b,d). The three components separate to varying degrees with offshore profile (Figure 2.3 a,c,e). Profiles with an offshore sandbar have smaller $R_{2\%,G}$ than those with a trough (compare blue with red in Figure 2.3 g). $R_{2\%,G}$ (the sum of components) depends on both $\beta_f$ and $\beta_{\text{eff}}$ (Figure 2.3 g,h). The profile-dependent spread indicates that $R_{2\%,G}$ on eroded profiles is generally higher than shallow (or barred) profiles for the tested wave conditions. Below we characterize the effect of different subaqueous bathymetry with an effective mid-surf zone slope $\beta_{\text{eff}}$.

First, the parameter values in existing formulations characterizing bathymetry with only the foreshore slope $\beta_f$ (Eq. 2.3 and 2.5) are optimized for this simulated data set. Based on the Hunt parameterization of $(H_0 L_0)^{0.5}$, and following S06 (Eq. 2.3), linear regressions give a Bulk runup form (RMSE $= 0.44$m, $R^2 = 0.40$)

$$R_{2\%,G} = (H_0 L_0)^{0.5} \left( 0.02 + \frac{1}{2} \left[ 0.005 + 0.4 \beta_f^2 \right]^{0.5} \right). \tag{2.6}$$

Below, Eq. 2.6 is referred to as "1-slope Bulk". Note the IG and SS swash constants (0.005 and 0.4, respectively) are within 50% of the S06 values (Eq. 2.3) of 0.004 and 0.56 respectively. A difference between the present results and S06 (Eq. 2.3) is that setup does not depend on $\beta_f$, in contrast with standard S06 (Figure 2.3 b). Here, when $\beta_f$ dependence is included in setup, skill decreases from 0.32 to $-0.72$ (see Table 2.1 for skills of individual components). The IG and SS swash terms (Eq. 2.6) are equal with steep foreshore beach slope ($\beta_f = 0.11$). Ignoring the SS swash term, the ratio of IG swash to setup terms is 1.8. Note that Eq. 2.6 nonlinearly couples IG and SS, and their total contribution to $R_{2\%,G}$ does not equal their linear sum.

A 1-slope IPA tuned to the current simulations maximizes model skill by optimizing values of $(\alpha, l, m, n)$ in $\left[\alpha \beta_f^l \int_{SS} E^m f^n df\right]_{deep}$, where $E$ is the incident sea-swell MOP spectra for $\eta$, $S_{IG}$ and $S_{SS}$. With allowed values $0 \leq m \leq 3$, $-4 \leq n \leq 3$, and $l = [0, 1, 2]$,

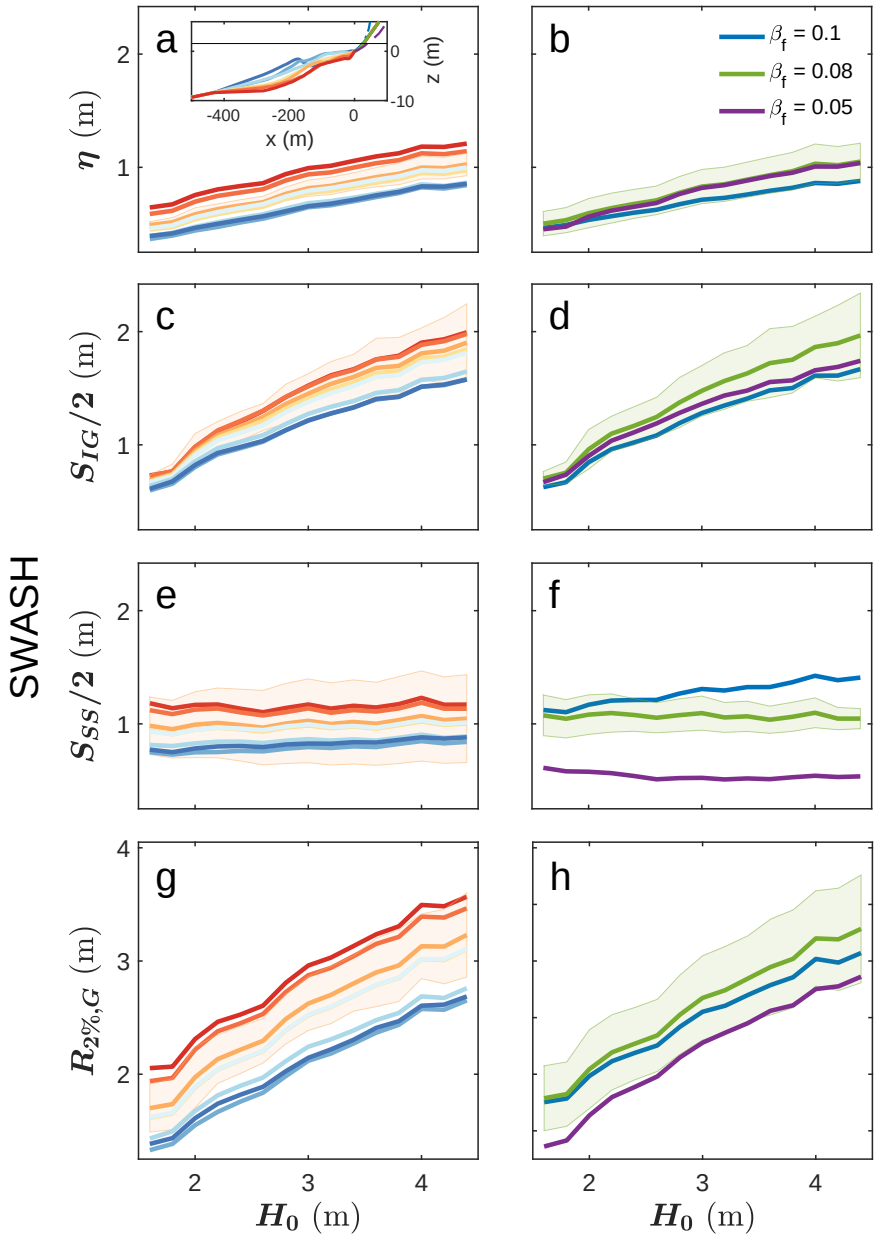


**Figure 2.3.** 20 cm binned means of SWASH-modeled runup components, (a,b) $\eta$, (c,d) $S_{IG}/2$ and (e,f) $S_{SS}/2$ and (g,h) total $R_{2\%}$ versus offshore wave height $H_0$. Line colors indicate subaqueous profile (left, see inset in a) and (right) subaerial beach slope $\beta_f$. The binned standard deviations of an average profile (orange/left) and $\beta_f = 0.08$ (right) are shown in the shaded area around their respective mean. All components depend on subaqueous profile (a,c,e), $S_{SS}$ depends most strongly on $\beta_f$ (f). SS swash (e,f) does not generally increase with increasing $H_0$, consistent with saturation.

the optimum form is

$$R_{2\%,G} = 0.12 \int_{SS} E^{0.45} f^{-1.3} df + 2 \left[ 0.52 \int_{SS} E^{0.9} f^{-0.2} df + 0.06 \beta_f^2 \int_{SS} E^{0.3} f^{-3.1} df \right]^{0.5}, \tag{2.7}$$

with $R^2 = 0.62$ and RMSE = 0.35m. Below, Eq. 2.7 is referred to as "1-slope IPA". Using the Hunt dependence $(H_0 L_0)^{0.5} \sim E^{0.5} f^{-2}$ in integral form gives $R^2 = 0.53$ and RMSE = 0.39m (not shown), confirming Fiedler et al. (2020) that an integral form of $(H_0 L_0)^{0.5}$ performs almost as well as with optimum powers. Skills for each component (setup, IG swash, SS swash) in untuned S06 (Eq. 2.3), 1-slope Bulk (Eq. 2.6), and 1-slope-IPA (Eq. 2.7) are in Table 2.1 and Figure 2.4. Note the ratio of IG to SS swash terms (Eq. 2.7) depends on $\beta_f^2$ similar to Eq. 2.6, but also depends on spectral shape. The $f^{-0.2}$ dependence for IG swash is much weaker than the $f^{-3.1}$ dependence of SS swash. The $E^{0.3}$ dependence of SS swash is relatively weak compared with setup and IG swash, and not inconsistent with SS saturation (Figure 2.3 e,f), as discussed below.

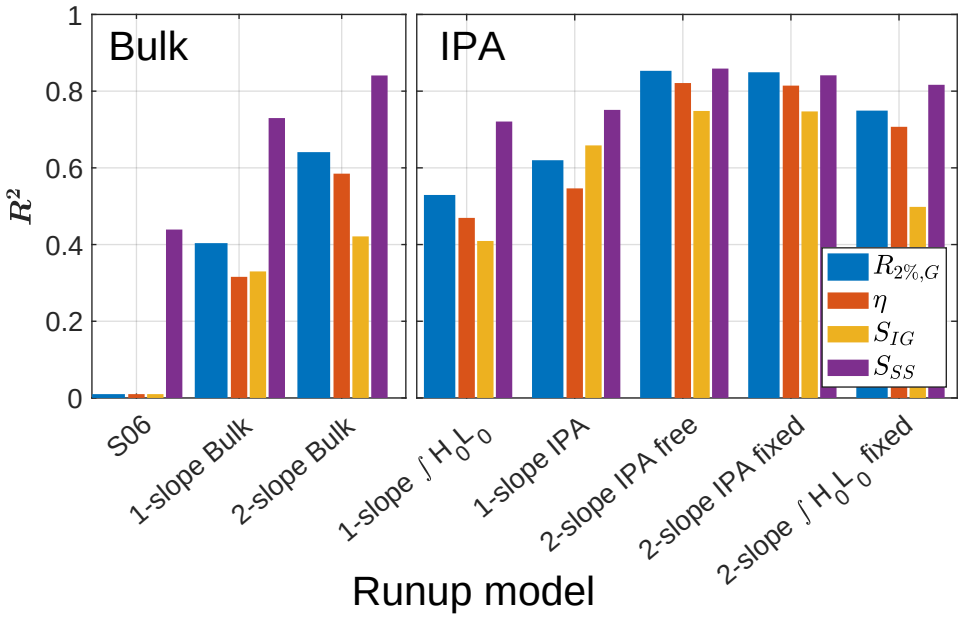


**Figure 2.4.** Model skill ($R^2$) for $R_{2\%,G}$, $\eta$ , $S_{IG}$, and $S_{SS}$ for 9 runup models using Bulk forms (left) and IPA forms (right). Each color corresponds to an $R_{2\%,G}$ component (see legend). Skill values below 0 are shown at 0. Skills are in Table 2.1.

**Table 2.1.** RMSE, skill ($R^2$), slope ($\alpha$) of the linear regression, and exponents $l, g, m, n$ are shown for selected runup parameterizations (left column). RMSE and skill shown for setup, IG, and SS swash and total $R_{2\%,G}$. The entries correspond to Eq. 2.3, 2.6, 2.12, unnumbered equation, 2.7, 2.9, 2.10 and 2.11.

| parameterization | component | RMSE | $R^2$ | $\alpha$ | $l$ | $g$ | $m$ | $n$ |
|---|---|---|---|---|---|---|---|---|
| S06 | $\eta$ | 0.45 | -3.87 | 0.35 | 1 | - | - | - |
| | $S_{IG}$ | 0.80 | -0.09 | 0.06 | 0 | - | - | - |
| | $S_{SS}$ | 0.54 | 0.44 | 0.75 | 1 | - | - | - |
| | $R_{2\%,G}$ | 0.75 | -0.77 | 1.1 | - | - | - | - |
| 1-slope Bulk | $\eta$ | 0.17 | 0.32 | 0.02 | 0 | - | - | - |
| | $S_{IG}$ | 0.63 | 0.33 | 0.07 | 0 | - | - | - |
| | $S_{SS}$ | 0.37 | 0.73 | 0.63 | 1 | - | - | - |
| | $R_{2\%,G}$ | 0.44 | 0.40 | - | - | - | - | - |
| 2-slope Bulk | $\eta$ | 0.13 | 0.58 | 0.09 | 0 | 0.4 | | |
| | $S_{IG}$ | 0.59 | 0.42 | 0.19 | 0 | 0.25 | - | - |
| | $S_{SS}$ | 0.29 | 0.84 | 2.33 | 1 | 0.35 | - | - |
| | $R_{2\%,G}$ | 0.34 | 0.64 | - | - | - | - | - |
| 1-slope $\int H_0 L_0$ | $\eta$ | 0.15 | 0.47 | 0.37 | 0 | - | 0.25 | -1 |
| | $S_{IG}$ | 0.59 | 0.41 | 0.01 | 0 | - | 0.5 | -2 |
| | $S_{SS}$ | 0.38 | 0.72 | 0.80 | 2 | - | 0.5 | -2 |
| | $R_{2\%,G}$ | 0.39 | 0.53 | - | - | - | - | - |
| 1-slope IPA | $\eta$ | 0.14 | 0.55 | 0.12 | 0 | - | 0.45 | -1.3 |
| | $S_{IG}$ | 0.45 | 0.66 | 0.52 | 0 | - | 0.9 | -0.2 |
| | $S_{SS}$ | 0.36 | 0.75 | 0.06 | 2 | - | 0.3 | -3.1 |
| | $R_{2\%,G}$ | 0.35 | 0.62 | - | - | - | - | - |
| 2-slope IPA | $\eta$ | 0.09 | 0.82 | 0.40 | 0 | 0.45 | 0.5 | -1.45 |
| | $S_{IG}$ | 0.39 | 0.75 | 3.72 | 0 | 0.6 | 0.95 | -0.25 |
| | $S_{SS}$ | 0.27 | 0.86 | 0.76 | 2 | 0.75 | 0.4 | -3.1 |
| | $R_{2\%,G}$ | 0.22 | 0.85 | - | - | - | - | - |
| 2-slope IPA (fixed slope) | $\eta$ | 0.09 | 0.81 | 0.47 | 0 | 0.5 | 0.5 | -1.45 |
| | $S_{IG}$ | 0.39 | 0.75 | 2.59 | 0 | 0.5 | 0.9 | -0.3 |
| | $S_{SS}$ | 0.29 | 0.84 | 2.55 | 2 | 1 | 0.45 | -2.95 |
| | $R_{2\%,G}$ | 0.22 | 0.85 | - | - | - | - | - |
| 2-slope $\int H_0 L_0$ (fixed slope) | $\eta$ | 0.11 | 0.71 | 2.38 | 0 | 0.5 | 0.25 | -1 |
| | $S_{IG}$ | 0.55 | 0.50 | 0.07 | 0 | 0.5 | 0.5 | -2 |
| | $S_{SS}$ | 0.31 | 0.82 | 31.88 | 2 | 1 | 0.5 | -2 |
| | $R_{2\%,G}$ | 0.28 | 0.75 | - | - | - | - | - |

### 2.4.1 2-slope parameterizations

To characterize the effect of subaqueous profile differences on $R_{2\%,G}$, an effective, mid-surf zone slope $\beta_{\text{eff}}$ is estimated for each profile (Figure 2.1) during each incident wave condition (Figure 2.2). For each SWASH run, the distance between the cross-shore location $x_{mid}$ where the shoreward SS linear energy flux is 50% of the incoming SS boundary flux ($\sim$ 17m water depth at MHHW, Figure 2.5 a) is identified. For a given wave case, shallower profiles have larger $x_{mid}$ than more eroded profiles. The sandbar profile has the largest $x_{mid}$ for all $H_0$. For all profiles, $x_{mid}$ increases with increasing offshore significant wave height $H_0$ (Figure 2.5 b). During the largest waves, the full surf zone width is deeper than 10m and therefore independent of profile, whereas $x_{mid}$ still differentiates between profiles.

The breaking wave height at $x_{mid}$ ($H_{mid}$) and the offshore wave height $H_0$, are highly correlated ($R^2 = 0.96$) (Figure 2.5 c), where $H_{mid} = CH_0$, with $C = 0.94$. The mid-surf zone width ($x_{mid}$) is incorporated in the runup parameterization as an effective surf zone slope:

$$\beta_{\text{eff}} = H_{mid}/x_{mid} = CH_0/x_{mid}. \tag{2.8}$$

Estimation of $\beta_{\text{eff}}$ from remote-sensing (rather than SWASH) is discussed in Section 3.5.

For a 2-slope IPA, $\left[\alpha\beta_f^l\beta_{\text{eff}}^g \int_{SS} E^m f^n df\right]_{deep}$, with all four powers $(l, g, m, n)$ allowed to vary, the optimized form has $R^2 = 0.85$ and RMSE = 0.22m,

$$\begin{aligned} R_{2\%,G} =& 0.4\beta_{\text{eff}}^{0.45} \int_{SS} E^{0.5} f^{-1.45} df \\ &+2\left[3.72\beta_{\text{eff}}^{0.6} \int_{SS} E^{0.95} f^{-0.25} df + 0.76\beta_f^2\beta_{\text{eff}}^{0.75} \int_{SS} E^{0.4} f^{-3.1} df\right]^{0.5}. \end{aligned} \tag{2.9}$$

The optimal values of $(l, g, m, n)$ in Eq. 2.9, referred to as "2-slope IPA free", yield skill $> 0.75$ for setup, IG and SS swash (Figure 2.4). IG swash has the lowest skill, perhaps owing to offshore IG boundary condition uncertainty. Free parameter values are not tightly constrained by the training data set. A 2-slope form with equal skill in each component

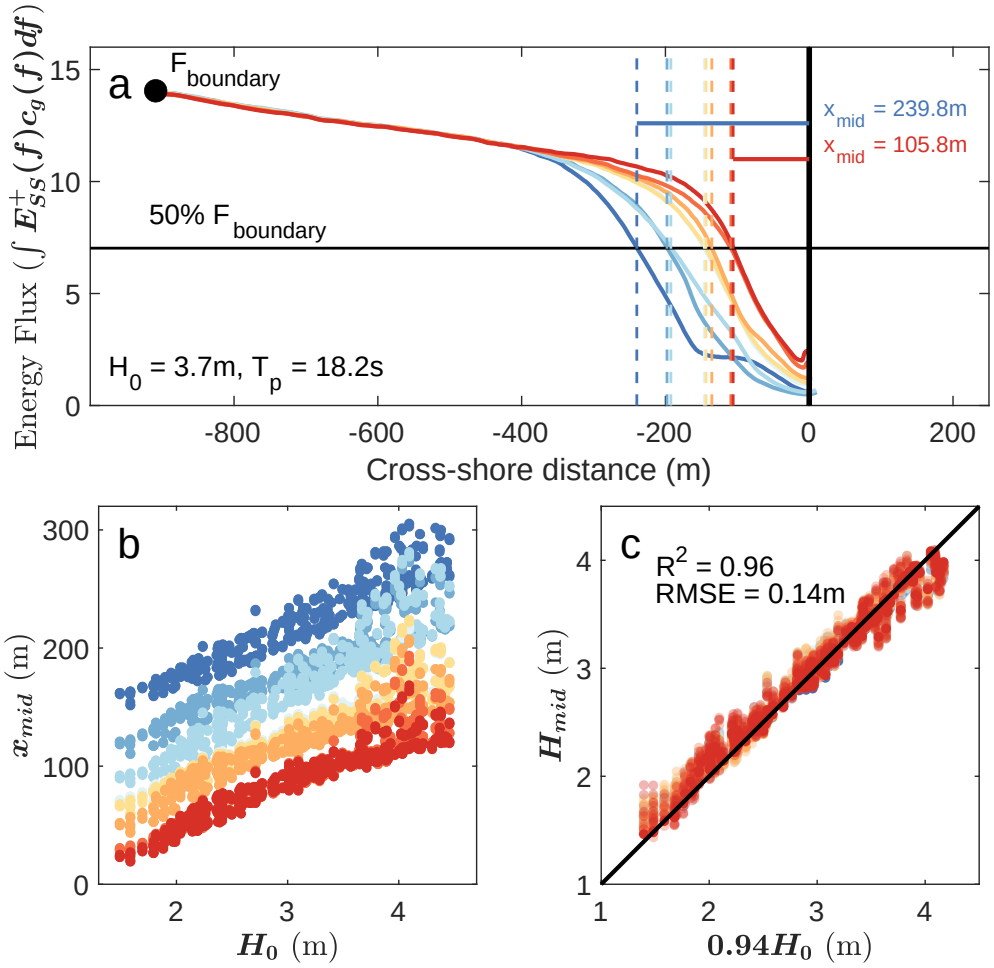


**Figure 2.5.** Example of $x_{mid}$ estimates using different bathymetry profiles (color corresponds to Figure 2.1) and $H_0 = 3.7$m, $T_p = 18$s, IG boundary condition: $E_{IG} = 0$, and $\beta_f = 0.1$. (a) Incoming sea-swell linear energy flux ($\int_{SS} E^+_{SS}(f)c_g(f)df$) versus cross-shore distance. The mid-surf zone width $x_{mid}$, where the flux equals 50% of the boundary flux $F$ (black dot), depends on surf zone bathymetry (blue = shallow with well-developed sandbar, red = eroded profile). For shallower (blue) profiles, wave breaking occurs further offshore. The foreshore area used to compute $\beta_f$ is excluded by the choice of the $x$ origin. (b) $x_{mid}$ versus $H_0$ for all cases. More eroded profiles (red) always have narrower $x_{mid}$ for the same $H_0$, and higher $H_0$ produce a larger $x_{mid}$ for all profiles. (c) Mid-surf zone breaking wave height $H_{mid}$ versus offshore wave height $0.94H_0$. Black line is 1:1.

uses fixed rounded values $(0, 0.5, 1, 2)$ for slope powers

$$\begin{aligned} R_{2\%,G} =& 0.47\beta_{\text{eff}}^{0.5} \int_{SS} E^{0.5} f^{-1.45} df \\ &+2\left[2.59\beta_{\text{eff}}^{0.5} \int_{SS} E^{0.9} f^{-0.3} df + 2.55\beta_f^2 \beta_{\text{eff}} \int_{SS} E^{0.45} f^{-2.95} df\right]^{0.5}. \end{aligned} \tag{2.10}$$

Error contours of the 2-slope IPA (with fixed power) ("2-slope IPA fixed", Eq. 2.10) shows that a range of $(m, n)$ combinations have similar high skill (dark green in Figure 2.6). For SS swash, high skill can also be achieved when $m = 0$, signaling no dependence on deep water energy $E$, consistent with saturation (Figure 2.6 c). In contrast, setup and IG swash more clearly increase with increasing $E$ (e.g. $m > 0$, Figure 2.6 a,b). Note that with low $\beta_f$ and negligible SS, the remaining setup and IG terms in Eq. 2.9 depend on $\sim E^{0.5} \sim H$, and not on $\beta_f$. Three empirical formulas (Senechal et al., 2011, Table 4, Eq. 1-3) that relate total swash $S$ to $H_0$ on dissipative beaches, with no frequency or beta dependence, have negative skill for the present runup simulations (not shown).

A model with $(m, n)$ prescribed by $H_0 L_0$ and fixed powers of $\beta$ (e.g. the "2-slope HoLo fixed" model), has 3 free parameters, the proportionality constant $\alpha$ for each component,

$$R_{2\%,G} = 2.38\beta_{\text{eff}}^{0.5} \int_{SS} E^{0.25} f^{-1} df + 2\left[\int_{SS} E^{0.5} f^{-2} df \left(0.07\beta_{\text{eff}}^{0.5} + 31.0\beta_f^2 \beta_{\text{eff}}\right)\right]^{0.5}. \tag{2.11}$$

Skill remains high in SS swash and setup, but IG swash skill falls to 0.5 (Eq. 2.11, Figure 2.4). The $H_0 L_0 \sim E^{0.5} f^{-2}$ dependence differs enough from optimal $E^{0.9} f^{-0.3}$ to degrade skill. The $R^2$ of $R_{2\%,G}$ is 0.75 (Eq. 2.11), which is lower than the 0.85 from the optimal forms (Eq. 2.9 or 2.10). Furthermore, IG and SS swash have the same $E^{0.5} f^{-2}$ dependence and SS swash does not show saturation effects. Finally, a bulk 2-slope form, where $\beta_{\text{eff}}^g$

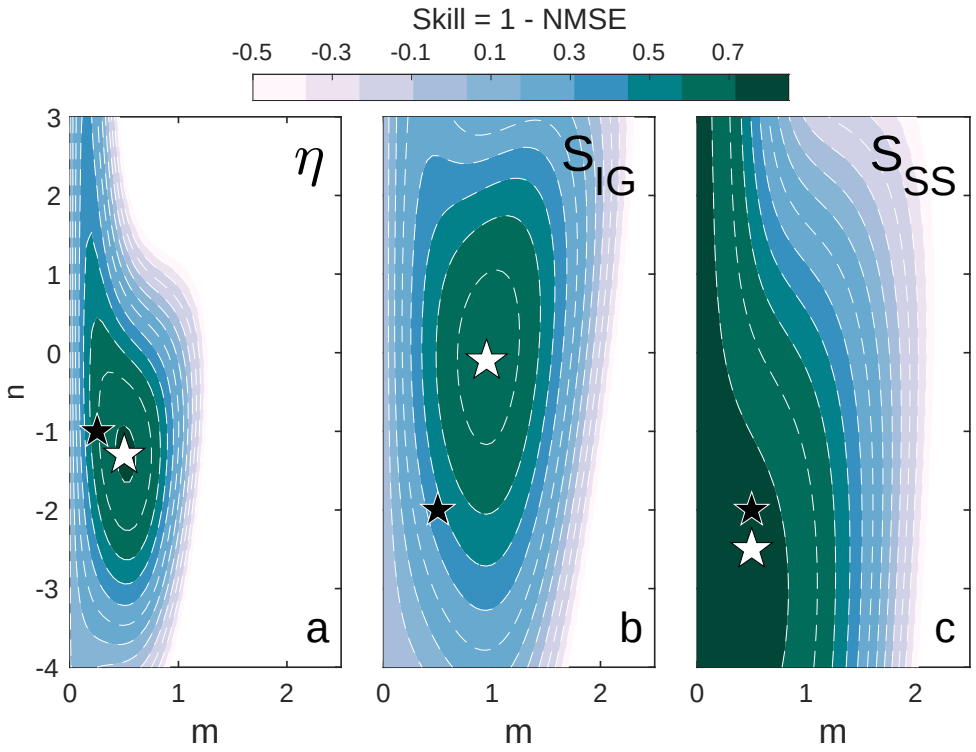


**Figure 2.6.** Skill $R^2$ contours of 2-slope power law fit (Eq. 2.10) for (a) $\eta$ ($\beta_f^0\beta_{\text{eff}}^{0.5}$), (b) $S_{IG}$ ($\beta_f^0\beta_{\text{eff}}^{0.5}$), and (c) $S_{SS}$ ($\beta_f^2\beta_{\text{eff}}^1$) versus energy ($m$) and frequency ($n$) powers $\left[\beta_f^l\beta_{\text{eff}}^g\int_{SS}E^m f^n df\right]_{deep}$. White stars highlight the optimum powers $(m,n)$ for each runup component. An integrated form of $H_0L_0$ and fixed exponents on the slopes (Eq. 2.11, black stars) has notably reduced skill in IG.

with $g$ variable between 0 and 2 has significantly decreased $R^2 = 0.45$ (Figure 2.4),

$$R_{2\%,G} = (H_0 L_0)^{0.5} \left( 0.09\beta_{\text{eff}}^{0.4} + \frac{1}{2}\left[0.036\beta_{\text{eff}}^{0.5} + 5.43\beta_f^2\beta_{\text{eff}}^{0.7}\right]^{0.5} \right). \tag{2.12}$$

The robustness of the parameter $H_0 L_0$ in both IPA (Eq. 2.11) and Bulk (Eq. 2.12) forms is noteworthy, but Eq. 2.10 ("2-slope IPA fixed") is preferred because it is more accurate yet still computationally simple.

## 2.5 Discussion

### 2.5.1 Errors

Error in parameterization is reduced by increasing the amount of included bathymetric and incident wave information. The simplest bulk 1-slope $\beta_f$ model has significant skill ($R^2 = 0.4$, Figure2.7 b) despite a pronounced bathymetric bias in the setup and SS swash components (Figure 2.7 a, 2.A.2 a,c). $R^2$ is improved to 0.64 by including spectral shape (1-slope IPA, Figure 2.7 b), and similarly to 0.62 by including subaqueous bathymetry (2-slope Bulk, Figure 2.7 c). All runup components in 1-slope IPA show a strong bathymetric bias, which is exacerbated by the largest offshore forcing (Figure 2.A.2 g-i). Including both spectral shape and $\beta_{\text{eff}}$ yields the 2-slope IPA fixed model, with $R^2 = 0.85$ and RMSE = 0.22m (Figure 2.7 d). Inclusion of $\beta_{\text{eff}}$ reduces the error associated with subaqueous bathymetry in both Bulk and IPA models.

The largest remaining error is the IG term (Figure 2.8), with error from the offshore IG boundary condition compounding other errors. For the Bulk models, even low offshore wave forcing can result in significant error in the IG swash component (Figure 2.A.2 b,e). Inclusion of spectral shape information (IPA models) improves this fit in smaller forcing ($H_0 < 3.5$m) but is degraded by the noise introduced by the boundary condition in larger wave forcings, most notably on the more eroded profiles (red dots, Figure 2.8 and 2.A.2 h,k). That is, IG boundary condition errors are oftentimes large in conditions favorable to

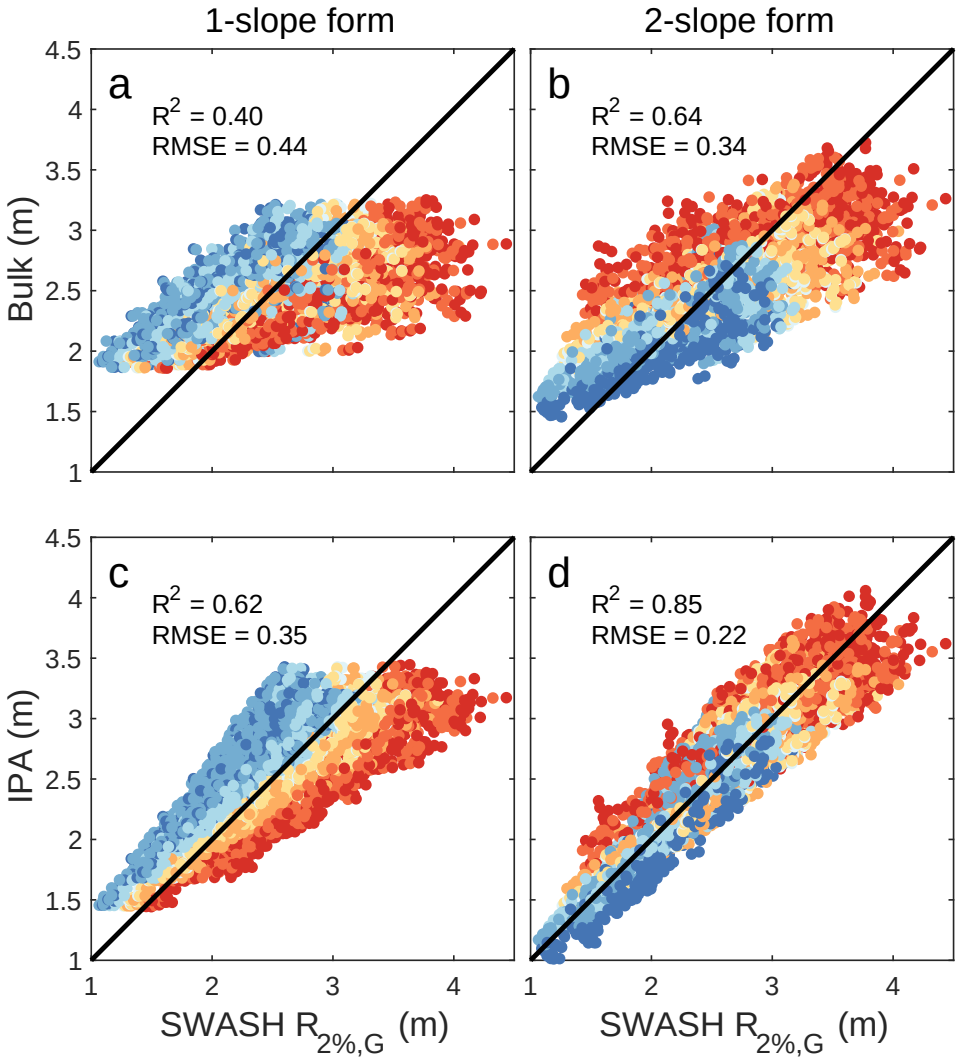


**Figure 2.7.** Empirical models versus SWASH-modeled $R_{2\%,G}$ for all 6624 model runs: (a) 1-slope Bulk (Eq. 2.6), (b) 2-slope Bulk (Eq. 2.12), (c) 1-slope IPA (Eq. 2.7), (d) 2-slope IPA fixed (Eq. 2.10). 1-slope only includes the foreshore beach slope $\beta_f$ and 2-slope also includes the effective mid-surf zone slope $\beta_{\text{eff}}$. The black 1:1 line indicates the parameterization agrees with SWASH. Dots are colored by profile (blue = shallow, red = eroded). Errors in the 1-slope forms (a,c) that depend on surf zone slope are reduced in the 2-slope forms (b,d). Errors in the Bulk models (a,b) are reduced by weighted (IPA) integrals (c,d).

overtopping (Figure 2.A.1). An improved offshore IG boundary condition, a 2D boundwave combined with an empirically determined amount of free waves, is under development.

### 2.5.2 Spectra

Average vertical runup spectra of the SWASH runs (Figure 2.9) illustrate the above results. The SS band spectra have a strong dependence on the foreshore beach slope, supporting the inclusion of a $\beta_f$ term in the SS swash component. This $f^{-4}$ slope in the SS band is consistent with saturation, as also suggested by the weak dependence of SS on $H_0$ (Figure 2.3 e,f) and $E$ (Figure 2.6).

The IG band shows a strong offshore boundary condition dependence, with $\beta_f$ having a much smaller impact, consistent with Figure 2.8. While both setup and SS swash have minimal difference between the results for the different offshore IG boundary condition ($< 10\%$), IG swash shows significant difference - almost 1m ($\sim 25\%$) in certain conditions. A more accurate boundary condition would help reduce this scatter.

The relative sizes of $\eta$, $S_{IG}$, and $S_{SS}$, are estimated by computing the ratio of terms for the different foreshore beach slopes as well as all 6624 model runs. In general, setup is less than both IG and SS swash, with mean $S_{IG}/\eta = 3.51$ and mean $S_{SS}/\eta = 2.61$, with few ratios less than unity (Table 2.2). On average, the modeled beach is dominated by IG waves, with mean $S_{IG}/S_{SS} = 1.64$, but the ratio is highly variable ($\sigma = 0.81$). In particular, the largest SS waves on the steepest foreshores tend to have SS dominated runup. On average, shoreline IG swash with a 1D boundwave offshore IG boundary condition is 90% of the IG swash with $E_{IG} = 0$ at the boundary (Table 2.2).

### 2.5.3 Limitations and applicability

This study is limited to wave events with $2.0 < H_0 < 4.5$m, 8 observed subaqueous bathymetries and 3 foreshore slopes between 0.05 and 0.11. The largest runups are driven by low frequency ($0.05 - 0.07$Hz) swell waves, and saturation of the SS swash is often

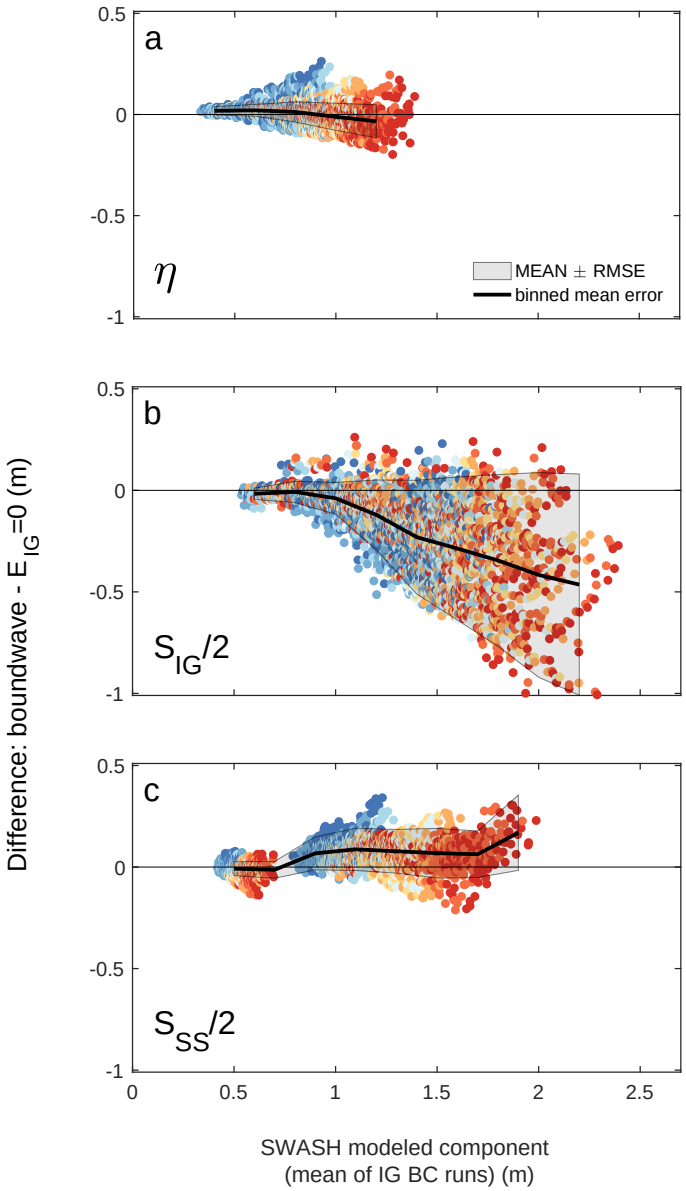


**Figure 2.8.** Scatter caused by different offshore IG boundary conditions in SWASH. For each component, the difference between the runup component values using the 1D boundwave and $E_{IG} = 0$ versus their average (a) $\eta$, (b) $S_{IG}$, (c) $S_{SS}$. Results are shown for all foreshore slopes, and are colored by subaqueous profile (Figure 2.1). Differences between $R_{2\%}$ owing to boundary conditions are relatively small for setup and SS swash, and largest for energetic IG waves on profiles lacking sandbars and other triggers of wave breaking (red in (b)).

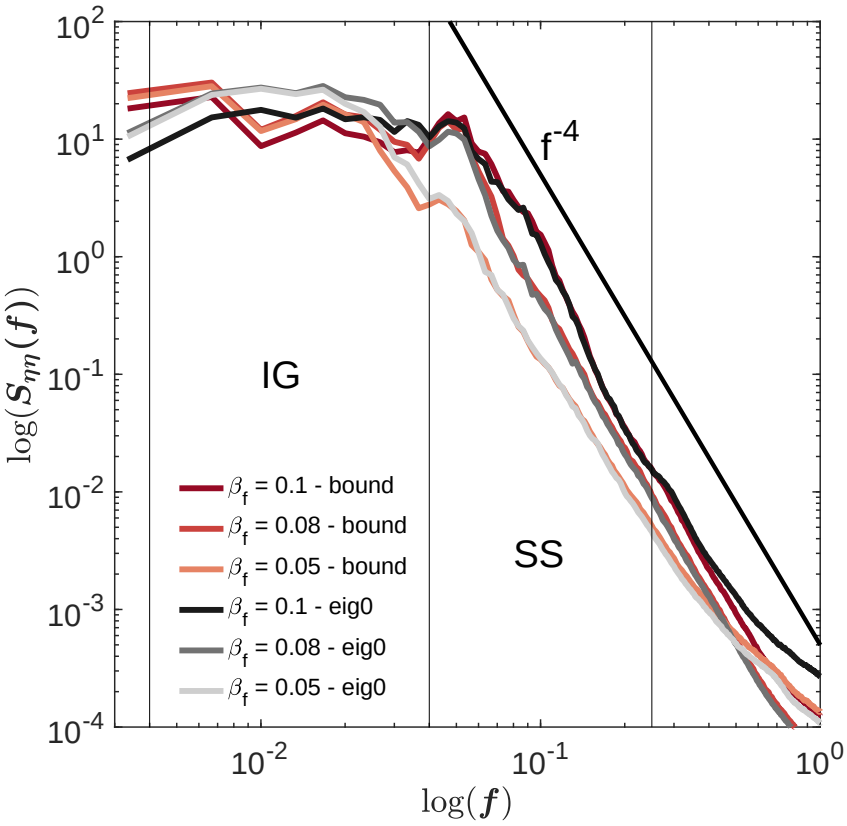


**Figure 2.9.** Shoreline vertical runup spectra, averaged for all eight subaqueous bathymetries and all 138 forcing conditions. Offshore IG boundary conditions (BC) are 1D boundwave and $E_{IG} = 0$, with 3 different $\beta_f$ (see legend). The vertical black lines define the IG and SS bands. SS spectra separate by $\beta_f$ and do not depend on offshore BC, whereas IG spectra depend on BC.

**Table 2.2.** Relative sizes of $\eta$, $S_{IG}$, and $S_{SS}$ split by foreshore beach slope and for all SWASH runs, and size of $S_{IG}$ from the 2 offshore IG boundary conditions.

| $\beta_f$ | Ratio | mean | $\sigma$ |
|---|---|---|---|
| $\beta_f = 0.1$ | $S_{IG}/\eta$ | 3.59 | 0.56 |
| | $S_{SS}/\eta$ | 3.68 | 0.48 |
| | $S_{IG}/S_{SS}$ | 1 | 0.24 |
| | $S_{IG(boundwave)}/S_{IG(E_{IG}=0)}$ | 0.89 | 0.11 |
| $\beta_f = 0.08$ | $S_{IG}/\eta$ | 3.58 | 0.52 |
| | $S_{SS}/\eta$ | 2.73 | 0.66 |
| | $S_{IG}/S_{SS}$ | 1.4 | 0.41 |
| | $S_{IG(boundwave)}/S_{IG(E_{IG}=0)}$ | 0.87 | 0.11 |
| $\beta_f = 0.05$ | $S_{IG}/\eta$ | 3.36 | 0.35 |
| | $S_{SS}/\eta$ | 1.42 | 0.46 |
| | $S_{IG}/S_{SS}$ | 2.55 | 0.66 |
| | $S_{IG(boundwave)}/S_{IG(E_{IG}=0)}$ | 0.89 | 0.10 |
| All $\beta_f$ | $S_{IG}/\eta$ | 3.51 | 0.49 |
| | $S_{SS}/\eta$ | 2.61 | 1.07 |
| | $S_{IG}/S_{SS}$ | 1.64 | 0.81 |
| | $S_{IG(boundwave)}/S_{IG(E_{IG}=0)}$ | 0.89 | 0.11 |

observed (Figure 2.6 c). A range of non-equilibrium profiles are included, for example a sandbar only observed during the 2009-2010 El Niño. $\beta_{\text{eff}}$ was found to be a useful tool to individuate these profiles. However, if the range of possible subaqueous bathymetries and waves is increased, the need for refined subsurface bathymetry estimates will also increase and $\beta_{\text{eff}}$ may not suffice to differentiate between different plausible subaqueous profiles. Other locations with less offshore morphologic change, either owing to geology (e.g. bedrock reef) or wave climate, might have no significant improvement in runup models by including the relatively constant $\beta_{\text{eff}}$.

The effective mid-surf zone slope $\beta_{\text{eff}}$, using the location where breaking reduces the incoming linear SS energy flux to 50% of the boundary flux, is estimated with SWASH. Gomes et al. (2016) showed that the locations of the time-averaged maximum of breaking intensity from SWASH and remote sensing (e.g. Argus, Holman, Stanley, 2007) are similar for the cases they considered. We used a 50% flux metric to define $x_{mid}$ in SWASH. An alternative definition uses the location of maximum dissipation. With the present

bathymetry and waves, $x_{mid}$ and $x_{max(Q_b)}$ are correlated ($R^2 = 0.44$, RMSE = 40.88m, Figure 2.10) for all subaqueous profiles (Figure 2.10 a) and offshore significant wave height (Figure 2.10 b). $x_{max(Q_b)}$ is the location of peak intensity of modeled wave breaking where $Q_b$ is the time averaged modeled wave breaking (Gomes et al. (2016, Eq. 8) $Q_b = \frac{1}{N_w}\frac{dx}{L_0}\sum B$, with $N_w = t_{simulation}/T_p$ as the ratio of simulation time to peak period, d$x$ cross-shore grid spacing, deep water wavelength $L_0$, and model-defined breaking $B$, a binary quantity). The correlation however degrades with extreme offshore wave heights. A subset of smaller offshore waves ($H_0 < 3$m) improves the agreement ($R^2 = 0.73$, RMSE = 22.9m). The correspondence between $x_{mid}$ and $x_{max(Q_b)}$ suggests that $\beta_{\text{eff}}$ or analogous simple proxies for effective bathymetry can be estimated remotely.

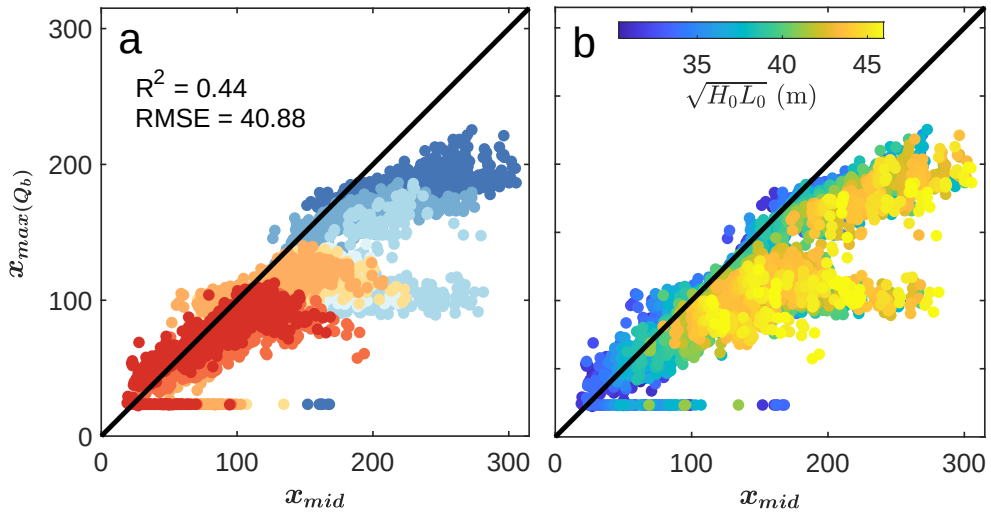


**Figure 2.10.** Cross-shore location of the effective, mid-surf zone $x_{mid}$ versus cross-shore location of the peak intensity of wave breaking $x_{max(Q_b)}$ (Eq. 8 Gomes et al., 2016), colored by (a) subaqueous bathymetry and (b) $(H_0 L_0)^{0.5}$. Black line is 1:1. With $H_0 < 3$m, skill increases to $R^2 = 0.73$ (RMSE = 22.9m).

## 2.6 Conclusion

In the absence of well-known subaerial and subsurface bathymetry, many empirical formulae for wave runup rely on a simple foreshore beach slope. Here, we improve on bulk runup estimations in large wave conditions through a frequency- and energy-weighted integrated offshore wave spectrum, and the inclusion of both a foreshore and effective surf zone slope. We have shown a 2-slope IPA model to decrease the error associated with large variations in subsurface bathymetry and large wave conditions, which may prove useful when bathymetric information is limited.

Remotely sensed morphology can inform overtopping/flood forecasts by specifying the present bathymetry, and how the beach (in a similar bathymetry) responded to past storms. Development of remote sensing of subaqueous bathymetry is ongoing (Holman et al., 1993; Aarninkhof, 2005; Dongeren van et al., 2008; Holman et al., 2013; Bak et al., 2019; Salameh et al., 2019; Geyman, Maloof, 2019; Benshila et al., 2020; Collins et al., 2020, and references therein). Extended remote observations of surf zone dissipation (including extreme events) at a site would help inform forecast models for morphologic change and runup.

## 2.7 Acknowledgments

This study was funded by the U.S. Army Corps of Engineers (W912HZ192) and the California Department of Parks and Recreation (C19E0026). B. Ludka provided the historical bathymetry data, and W.C. O'Reilly the MOPS modeling modeling. Data was collected and processed by Center for Coastal Studies field team members Lucian Parry, Rob Grenzeback, Kent Smith, Brian Woodward, Greg Boyd, and Mele Johnson. Laura Engeman and Michele Okihiro organized logistics.

Chapter 2, in full, is a reprint of the paper "Estimating runup with limited bathymetry" published in Coastal Engineering by A.M.Z. Lange, J.W. Fiedler, J.M.

Becker, M.A. Merrifield and R.T. Guza in 2022. The dissertation author was the primary investigator and author of this paper.

## 2.A Errors

$R_{2\%,G}$ contains errors from $\eta$, $S_{IG}$, and $S_{SS}$. The least-square fits are weighted towards the most frequently occurring $H_0 < 3.5$m. IPA fits for the relatively few points with $H_0 > 3.5$m are biased low by as much as 1m (Figure 2.A.1).

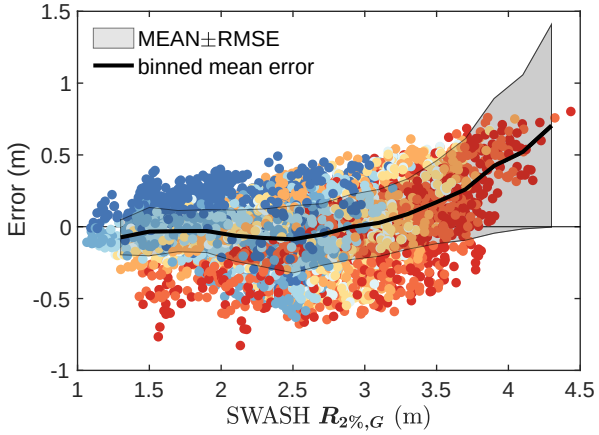


**Figure 2.A.1.** Difference between 2-slope IPA fixed (Eq. 2.10) $R_{2\%,G}$ versus SWASH $R_{2\%}$. The misfits arise from incomplete knowledge of the bathymetry and uncertainty in the IG BC.

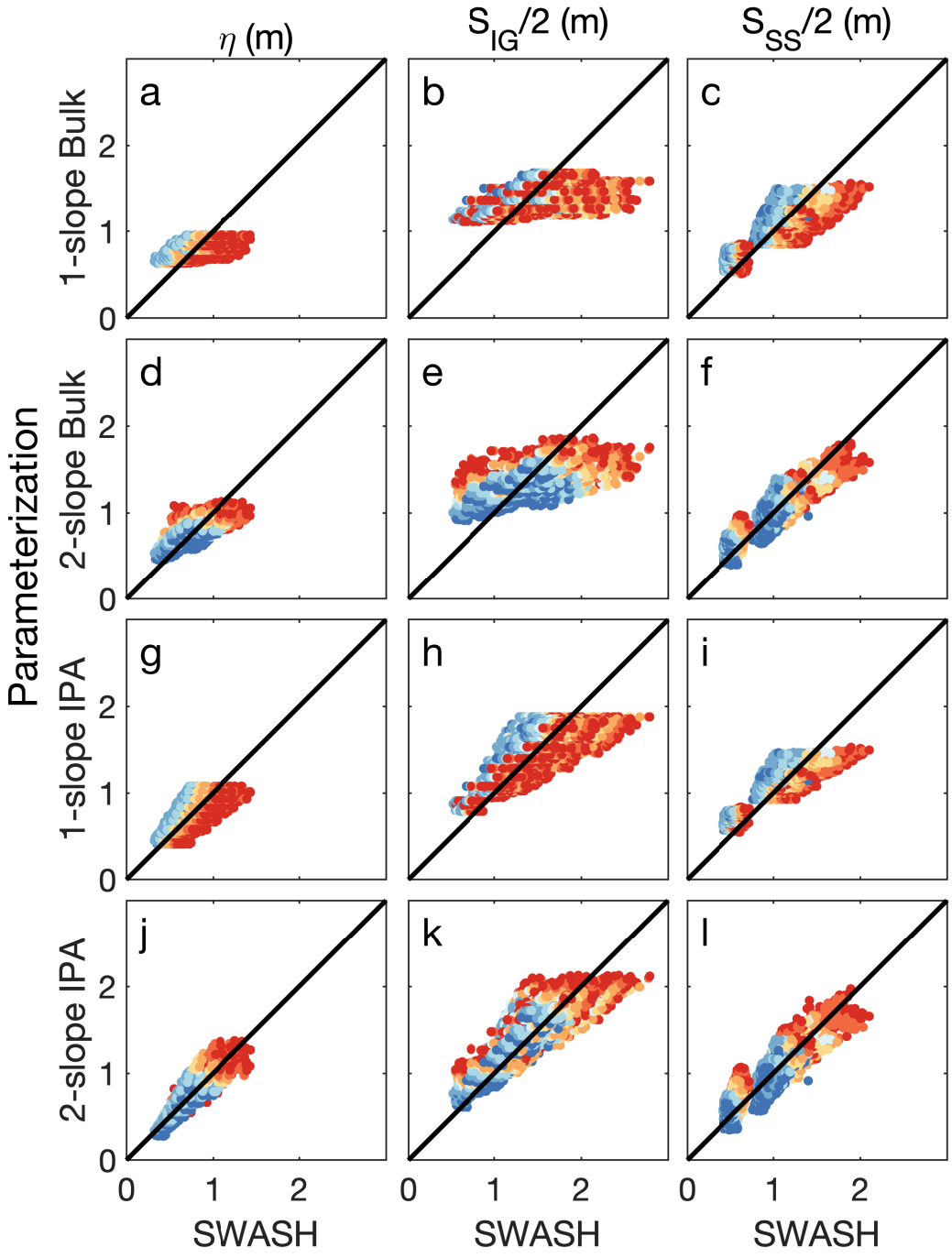


**Figure 2.A.2.** Predicted and SWASH-observed runup components $\eta$, $S_{IG}$ and $S_{SS}$ (left to right columns) for the (a-c) 1-slope Bulk (Eq. 2.6), (d-f) 2-slope Bulk (Eq. 2.12), (g-i) 1-slope IPA (Eq. 2.7), and (j-l) 2-slope IPA fixed (Eq. 2.10) models. Dots colored by subaqueous bathymetry (see Figure 2.1). Component parameterizations and statistics are in Figure 2.4 and Table 2.1.

# Chapter 3

# UAV video-based estimates of nearshore bathymetry

## 3.1 Abstract

Nearshore bathymetry estimated from video acquired by a hovering UAV is compared with ground truth. Bathymetry estimates from the widely used cBathy algorithm are improved by crest tracking (with machine learning) from near breaking through the surf zone. Individual wave crests (distinguished from the breaking wave toe that can move down the wave front face) in video timestacks are determined with a deep-learning neural network and surf zone depth estimates are computed from the wave celerity. Time-2D spatial transforms (cBathy) are used to estimate wave celerity and depth between the surf zone and 10-m depth. Composite profiles (cBathyCT), formed by joining cBathy and crest-tracking solutions near the surf zone seaward edge, based on a newly determined $\gamma(x)$ parameter, avoid the large cBathy errors associated with the onset of breaking. Incident wave heights were relatively constant on each day but varied over days between $0.55 - 2.15$m. Averaged over all 17 min hovers and cross-shore transects (112 total), surf zone depths errors were relatively small (average root-mean-square error $\langle \text{RMSE} \rangle = 0.17$m, $\langle \text{Bias} \rangle = 0.06$m) after including a heuristic nonlinear correction to the linear phase speed. Between the seaward surf zone edge and 10m depth, errors are similar to previous cBathy studies: $\langle \text{RMSE} \rangle = 0.87$m, $\langle \text{Bias} \rangle = 0.58$m with the largest errors in deepest water. Beach

profiles were generally similar for all 8 test days, concave up with a slight terrace (no sandbar) and small alongshore depth variations. Accuracy was lower on one transect with a shallow reef.

## 3.2 Introduction

Accurate bathymetry is critical to understanding nearshore processes like beach erosion and accretion, the fate of beach nourishment sand, sandbar migration, and the corresponding hydrodynamics. While topography above the waterline may be monitored efficiently with mobile scanning LiDAR or photogrammetry, subaqueous nearshore bathymetry is usually less well-known owing to the expense of insitu subaqueous surveys. Early-warning overtopping forecasts can therefore have limited accuracy owing to oversimplified (planar) or outdated bathymetry (Stephens, Cloke, 2014; Stokes et al., 2019; Jordi et al., 2019; Silva Gomes da et al., 2020; Stokes et al., 2021; Merrifield et al., 2021; USGS, 2022, and references therein).

Remote sensing via satellite or video can provide relatively wide-area, low-cost observations of nearshore bathymetry. Satellite subaqueous observations require relatively clear water, and resolution in space and time can be limited (Vanderstraete et al., 2003; Mallet, Bretar, 2009; Gao, 2009; Jing, Datt, 2010; Abileah, Trizna, 2010; Zuckerman, Anderson, 2018; Legleiter, Harrison, 2019; Li et al., 2019; Geyman, Maloof, 2019). Enabled by improved cameras and computing power, nearshore bathymetry can be estimated using video observations of surface wave dissipation and celerity (Holman, Haller, 2013). Wave dissipation methods use high-intensity peaks in time-averaged images (timex e.g. ARGUS stations (5-camera system, Holman, Stanley, 2007)) to identify persistent foam caused by depth-limited breaking on sandbar crests (Lippmann, Holman, 1989; Aarninkhof, 2005; Collins et al., 2020). Celerity-based methods exploit the dependence of wave celerity on depth (Stockdon, Holman, 2000; Catálan, Haller, 2008; Plant et al., 2009; Almar et al.,

2009; Holman et al., 2013; Holman, Haller, 2013; Wengrove et al., 2013; Radermacher et al., 2014; Bergsma et al., 2016; Rutten et al., 2017; Thuan et al., 2019; Tsukada et al., 2020).

The accuracy of estimated depths can be improved with prior imagery from long-term observations and sophisticated numerical modeling. Observed and numerical model predictions of wave dissipation patterns can be coupled and used in data-assimilation schemes that estimate depth from pixel intensity, wave celerity and other observables (Aarninkhof, 2005; Dongeren van et al., 2008). Full end-to-end machine learning methods combine image analysis with extensive past bathymetry observations and sophisticated wave modeling (Collins et al., 2020).

Bathymetry is often required in areas lacking continuous, long-term observations, and the fixed, elevated platform for a permanent camera system. To address this, hovering UAVs (Uncrewed Aerial Vehicles) have increasingly been used for nearshore observations (Brodie et al., 2019). In this study, we evaluate the accuracy of bathymetry estimates obtained from relatively short (17-minute) observations taken from a hovering UAV, without use of prior imagery, bathymetry surveys, or numerical wave models. We use celerity and the proportion of waves breaking in relation to cross-shore location to refine depth estimates in the outer surf zone, where the mix of both broken and unbroken creates errors in existing methods.

Bathymetry is estimated in four steps: 1) cBathy is applied offshore of the surf zone, 2) timestack images are used to track individual wave crests and locate the onset of breaking. Crests are tracked with a deep learning U-Net algorithm, 3) surf zone depth is estimated using the observed crest celerity and shallow water theory with a simple nonlinear correction and 4) full depth profiles (from backbeach to 8m depth) combine cBathy offshore, crest tracking in the surf zone, and a low-tide survey of the subaerial beach.

In Section 3.3, existing video-based estimates of bathymetry are reviewed and

extended. Observations are described in Section 3.4. In Section 3.5, methods valid within and seaward of the surf zone are combined, yielding composite profiles that are then compared with ground truth bathymetric surveys. Error sources and the need for additional model development to include complex bathymetry are discussed in Section 3.6.

## 3.3 Background

### 3.3.1 cBathy

cBathy (Holman et al., 2013; Holman, Bergsma, 2021) is a popular, open-source celerity-based depth inversion algorithm. It fits the most coherent frequency-wavenumber pairs (default of 4) to the cross-spectra of all pixels within a given area around a point. The depth estimates are based on the nonlinear best fit from the dominant frequency-wavenumber pairs from the surrounding points and the linear dispersion relationship (see Table 3.5.1 for cBathy parameters used here). cBathy $\langle$RMSE$\rangle$ (average root-mean-square-error) of individual estimates are $\sim 0.72$m with low waves (H $< 1.2$m) and 1.28m with all H included (Wengrove et al., 2013; Brodie et al., 2018; Bergsma et al., 2019; Holman, Bergsma, 2021; Rodríguez-Padilla et al., 2022) The offshore extent of accurate cBathy depends on camera quality, elevation, and stabilization (particularly for UAVs, Bergsma et al., 2019); insitu validation is limited to $< 7$m depth at the Field Research Facility (FRF) in Duck, NC, USA, and reasonably good agreement ($\langle \text{RMSE} \rangle = 0.56\text{m}, \langle \text{Bias} \rangle = -0.41\text{m}$) between cBathy and observations as deep as 14m were obtained at Agate Beach, Oregon, USA using an elevated (128m) headland-mounted camera (Holman et al., 2013). Results here extend to 10m depth, about 500m from the backbeach.

cBathy assumes spatially homogeneous waves and bathymetry over a specified tile size (here we use 50m cross-shore by 200m alongshore, Figure 3.3.1). Prior to wave breaking, wave front faces usually appear darker than wave rear faces. However, when waves begin breaking, the foam-dominated front wave face becomes much brighter (whiter)

than the back face, reversing the pattern from offshore. Switching between dark and light wave faces within a tile can cause large celerity and depth overestimates and is known as the Modulation Transfer Function (MTF). Holman et al. (2013) suggests using the shifting cross-shore location of the "switching region" over a tidal cycle (or longer) and a Kalman filter to reduce these errors. Kalman results accumulate over a series of prior data collections, with each new run improving the estimate until the results stabilize after roughly one or two days (Holman, Bergsma, 2021). Alternatively, Bergsma et al. (2019) used the absolute value of the pixel intensity time derivative to augment timestacks and reduce foam on the image. This modified signal is included in the input data for cBathy and reduces the surf zone $\langle \text{RMSE} \rangle$ from 3.1m to 1.3m. Here, surf zone depths are inferred from 17-min timestacks of individual waves (Figure 3.3.1 c,d), without Kalman filtering.

### 3.3.2 Timestack Analysis

Timestack images (Figure 3.3.1 c,d) show wave evolution over time on a single cross-shore transect, rather than snapshots of a 2D field (Figure 3.3.1 a,b). The x-location of individual shoaling and breaking waves can be determined in sequential pixel columns. Depth estimates based on video celerity are necessarily heuristic. The relationship between pixel intensity and sea surface elevation is a required assumption (Lippmann, Holman, 1991). Many RGB image-based timestack analyses use standard edge detection algorithms (Canny or Sobel, Szeliski, 2022) to identify the wave toe, the bright front edge of the incoming, breaking waves that sharply contrast with the darker water in front. However, as spilling breaking begins and the roller slides down the wave face, the toe moves faster than the crest, increasing the estimated speed and complicating depth inversions. The roller toe eventually reaches a relatively stable position on the wave face, and in the inner surf zone is a stable proxy for the wave crest (Stive, 1980; Basco, 1985; Svendsen et al., 2003). Traditional computer vision approaches have difficulty detecting wave crests (as opposed to toes) robustly inside the surf zone due to the complexity of foam patterns

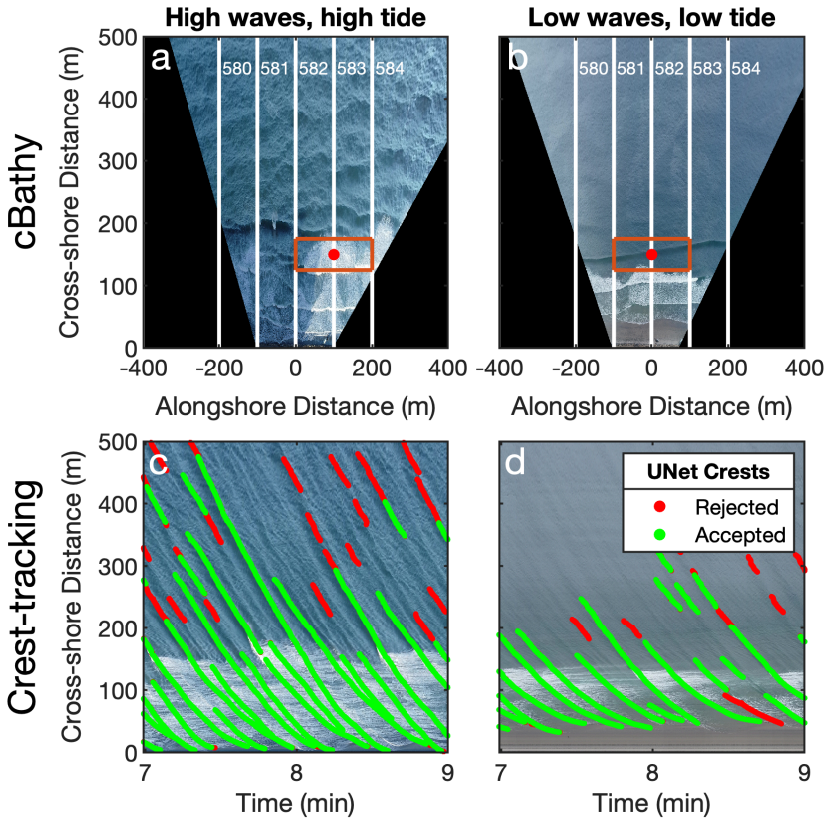


**Figure 3.3.1.** Contrasting conditions (left) Dec 15th, 2021, relatively high waves and high tide (Hs = 1.96m, tide = 1.41m) and (right) Dec 2nd, 2021, lower waves and lower tide (Hs = 0.64m, tide = 0.46m.) Beach is at the bottom of each image. (Upper) Orthorectified planview images of shoaling region and surf zone. Orange rectangle encloses 200m-alongshore by 50m-cross-shore area used for each cBathy depth estimate (red dot). Box dimensions increase offshore. Ground-truth survey cross-shore transects (white) are identified by "MOP" number. (Lower) wave crest trajectories (cross-shore location versus time) determined by a deep learning algorithm on MOPs (c) 583 and (d) 582. Red trajectories were rejected for further analysis.

(Stringari et al., 2019). Yoo et al. (2011) combined Radon-transform edge tracking and a nonlinear wave propagation model to estimate shallow water ($h < 2$m) bathymetry accurately ($\langle \text{RMSE} \rangle = 0.25\text{m}, \langle \text{Bias} \rangle = 0.1\text{m}$) with relatively low incident wave heights ($\text{H} < 0.8\text{m}$) on bathymetry not dissimilar to Torrey Pines State Beach, CA, USA (our primary study site). Stringari et al. (2019) estimates phase speed using a combination of Sobel edge detection, pixel-intensity extrema, and machine learning to extract the white signature of 'foam corresponding to the crests of breaking waves' with surf zone wave heights and depths less than 1m.

We were unable to implement Stringari et al. (2019), Yoo et al. (2011), and Bergsma et al. (2019) with the present observations. Almar et al. (2009) and Tsukada et al. (2020) obtain mean wave celerity using a cross-correlation technique with varying space and time intervals. However, for a test case, the correlation methods were relatively noisy for the present data and still exhibit the well-known errors in the breakpoint transition zone (not shown). Here we describe an alternative and reproducible crest-tracking algorithm with good surf zone performance, available in a GitHub repository. A crest-tracking algorithm with good surf zone performance with Hs as large as 2m in 4m depth is described and combined with cBathy estimates valid offshore and a low-tide subaerial survey to obtain a full nearshore profile.

### 3.3.3 Surf Zone Wave Celerity

In linear (small amplitude) shallow water theory waves advance with celerity

$$c = \sqrt{gh}. \tag{3.1}$$

However, nonlinear shoaling and breaking waves travel with amplitude-dependent phase speeds faster than $c$ (Svendsen, Buhr Hansen, 1976; Svendsen et al., 2003). For idealized

cnoidal and solitary waves with wave height H

$$c^2 = g(h + H) = gh(1 + H/h), \tag{3.2}$$

(Inman et al., 1971; Thornton, Guza, 1982; Stockdon, Holman, 2000). Assuming a saturated surf zone with $\gamma = H_{rms}/h$ yields

$$h_{estimate} = c^2/(g(1 + \gamma). \tag{3.3}$$

Surf zone waves are not constant shape as assumed in Eq. 3.2. Although phase speeds for nonlinear random waves generally increase with increasing amplitude, Eq. 3.3 is a heuristic simplification.

Variations in observed $\gamma$ between 0.3 and 1.1 have been ascribed to the effects of beach slope, breaker wave type (e.g. plunging versus spilling) and location within the surf zone (Raubenheimer et al., 1996; Catálan, Haller, 2008; Brodie et al., 2018). For both broken and unbroken waves, $c$ on average increases with increasing amplitude and depth but celerity observed on a wave-by-wave basis diverges from Eq. 3.3. Despite these complications, corrections based on Eq. 3.3 consistently improve celerity-based surf zone depth estimates (Holland, 2001; Svendsen et al., 2003; Catálan, Haller, 2008; Yoo et al., 2011; Tissier et al., 2015; Martins et al., 2018; Fiedler et al., 2021). We compare observed depths with estimates from linear (Eq. 3.1) and simplified nonlinear (Eq. 3.3) crest-tracking methods.

## 3.4 Observations

We completed 52 UAV hovers in San Diego, California with a DJI Phantom 4 RTK drone: 39 hovers over 6 days at Torrey Pines State Beach (July 2020 - Dec 2021), 6 hovers during 1 day at Cardiff State Beach, and 7 hovers over 1 day at Scripps Institution

of Oceanography (SIO). Wave conditions were relatively constant during data collection on each day, and varied over the 8 days, with $0.55 < H_0 < 2.15$m and $9 < T_p < 17.6$s (Table 3.4.1). Transects are defined by MOnitoring and Prediction (MOP) System number (O'Reilly et al., 2016). Torrey Pines depth varies little alongshore with a maximum difference of approximately 1m across $300 - 500$m (Figure 3.4.1 a insert). Bathymetries at the three sites are similar, with the exception of a pronounced bedrock reef on MOP 667 at Cardiff and a well-developed terrace at SIO (Figure 3.4.1). The beach profile near and above the waterline was measured with subaerial (LiDAR or photogrammetry) beach surveys on the same day as UAV hovers.

**Table 3.4.1.** UAV flight info and wave conditions from MOP forecasts in 10m depth. Incident wave parameters include significant wave height $Hs$, peak period $T_p$, and obliquity relative to beach normal.

| Date | Location | Hovers (MOP transect) | $Hs$ (m) | $T_p$ (s) | Obliquity (degree) | Tide Range (NAVD88m) |
|---|---|---|---|---|---|---|
| Jul 07, 2020 | Torrey Pines | 13 (579 - 584) | 0.89 | 11.3 | -12 | -0.27 - 1.13 |
| Oct 10, 2020 | Scripps | 7 (513 - 514) | 0.55 | 9 | 14 | 0.22 - 0.8 |
| Jul 09, 2021 | Cardiff | 6 (670 - 667) | 0.8 | 16.7 | -21.5 | 0.28 - 0.9 |
| Jul 12, 2021 | Torrey Pines | 6 (581 - 584) | 0.7 | 10 | 7 | -0.06 - 0.41 |
| Oct 26, 2021 | Torrey Pines | 5 (581 583) | 2.15 | 17.7 | 1 | 1.07 - 1.26 |
| Nov 02, 2021 | Torrey Pines | 5 (581 583) | 1.12 | 16.7 | 6 | 0.1 - 0.72 |
| Dec 02, 2021 | Torrey Pines | 5 (581 583) | 0.65 | 12.3 | 2 | -0.22 - 0.49 |
| Dec 15, 2021 | Torrey Pines | 5 (581 583) | 1.96 | 15.4 | -4 | 0.8 - 1.4 |

UAV hovers were typically 17 min (minimum 10 min). The UAV hovered between 27 and 91.5m above NAVD88, with no significant difference in performance with height. JPEG images were extracted from the video using the ffmpeg tool at 10Hz. RTK-surveyed, 1m x 1m checkerboards provide stability control points used for rectification with CIRN UAV Rectification software (Bruder, Brodie, 2020). Cross-shore timestacks were extracted at 20m along-shore intervals, gridded up to 500m offshore at 0.1m spacing. The $(dx, dt)$ size was kept constant across all extracted timestacks and is a trained part of the neural network.

Ground truth was insitu (labor-intensive) bathymetry surveys (jet ski, push dolly, All-Terrain Vehicle) on 100-m alongshore intervals to 10m depth usually obtained on the same day as the hovers, and always within one day. There were usually 3 cross-shore transects within the video field of view (Table 3.4.1), although the number varied with different video look angles. The 52 hovers included a total of 11 unique surveyed transects at 3 sites, with a total of 112 transects with ground truth.

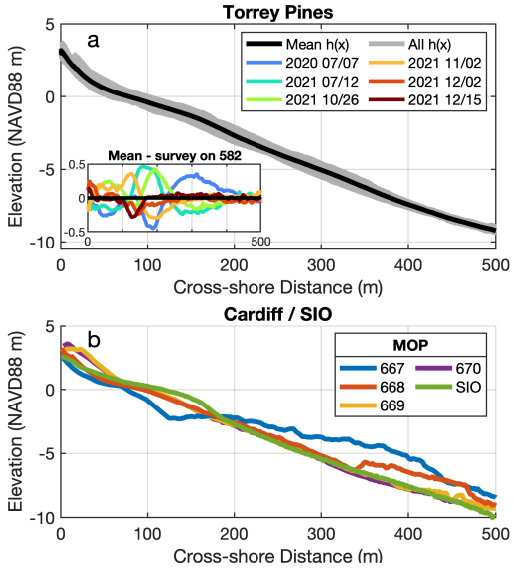


**Figure 3.4.1.** Seabed elevation versus cross-shore distance at (a) Torrey Pines. Mean of all transects and days (bold, $n = 42$) and shaded by range of all observed profiles. (insert) Deviations of MOP 582 transect from mean, colored by date. (b) Cardiff (reef at $x > 125$m on MOP 667, blue) and SIO (green MOP 514).

## 3.5 Methods

Our proposed method combines an existing celerity-based depth inversion algorithm (cBathy 2.0, Holman et al., 2013; Holman, Bergsma, 2021), which has been shown to be most effective seaward of the surf zone, with nonlinear surf zone depth estimates derived from machine learning-aided timestack wave crest tracks. The method is implemented in four steps.

### 3.5.1 cBathy Surf Zone Depth Estimation

cBathy results based on a single hover (no Kalman filtering) have much larger RMSE in the surf zone than offshore, similar to Holman et al. (2013); Brodie et al. (2018); Bergsma et al. (2019) and others. Holman, Bergsma (2021) consider cBathy estimates unreliable when the cBathy 95% confidence interval hErr $> 0.5$. This criterion can underestimate the width of the overpredicted data (Figure 3.5.1 a) or fail to identify a narrow surf zone (Figure 3.5.1 b) resulting in $\langle$RMSE$\rangle$ and $\langle$Bias$\rangle > 0.8$m. A constant threshold other than hErr $> 0.5$ did not reliably estimate where cBathy failed. An alternative criterion assumes that cBathy estimates are corrupted by a mix of breaking (white faced) and nonbreaking (dark faced) waves. The fraction of waves breaking (determined from timestacks, below) defines the region of cBathy validity as $> 95\%$ (inner surf zone) or $< 5\%$ (offshore) of waves breaking (Figure 3.5.1 e,f), and can be used instead of the standard hErr $> 0.5$ as the region where cBathy fails. In addition, the fraction of wave breaking can also be used to determine a nonlinear correction (described in Section 3.5.3) to include in the cBathy estimates. For all 3 error-filtered cBathy versions (only using hErr $< 0.5$, removing timestack derived wave-breaking region, and nonlinear correction to cBathy), estimates are interpolated across regions where cBathy fails (according to the different criteria, Figure 3.5.1).

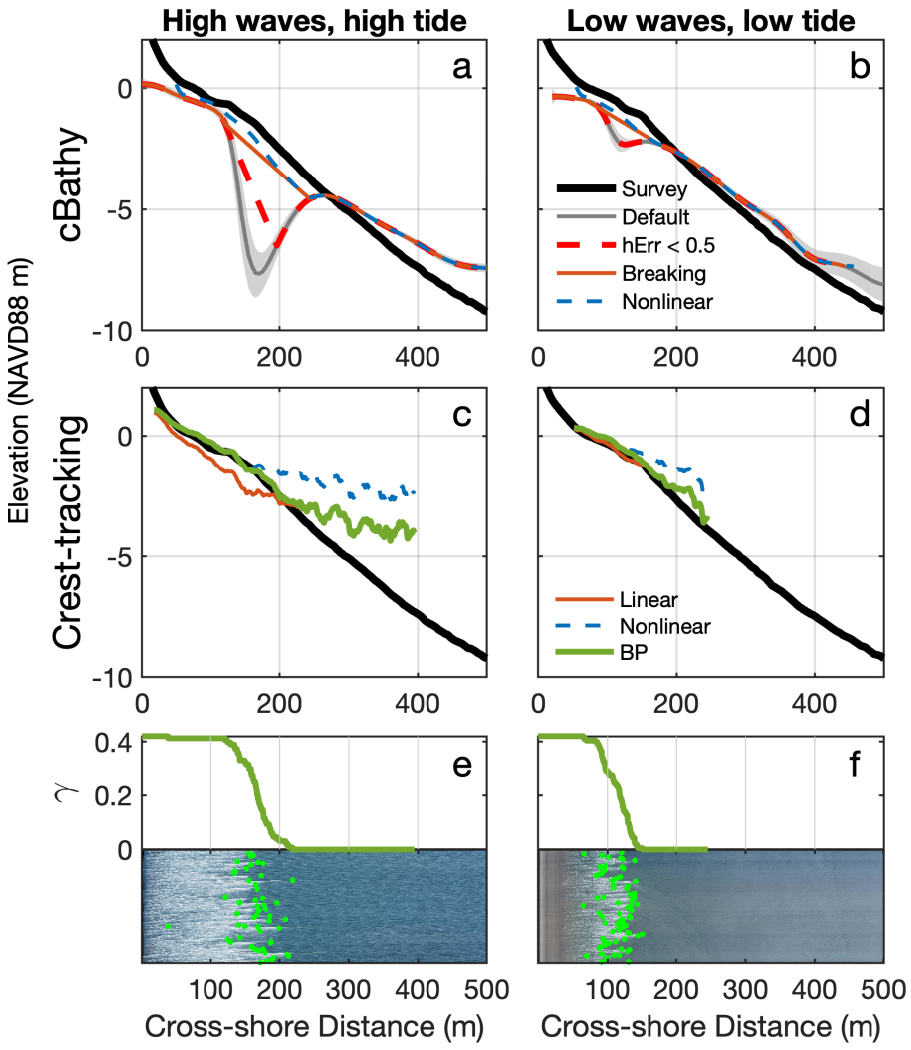


**Figure 3.5.1.** Bed elevation versus cross-shore distance for relatively (a,c) high waves and tide, Dec 15th, 2021 (Hs = 1.96m, tide = 1.41m) and (b,d) low waves and tide, Dec 2nd 2021 (Hs = 0.64m, tide = 0.46m) at Torrey Pines State Beach, USA. Mean ground-truth survey (black). Remote sensing estimates: (a,b) cBathy: default (gray with hErr shaded), hErr > 0.5m removed and interpolated over (red dashed), breaking region removed and interpolated (red solid) and (best cBathy-only method) with a nonlinear correction (blue dashed). (c,d) crest-tracking, linear (solid red), nonlinear (blue dashed), breakpoint transition (green). (e,f) effective $\gamma = H/h$ versus cross-shore distance above compressed view of the corresponding timestack with detected breakpoints shown (green dots). Effective $\gamma(x)$ is the mean of $\gamma$ step functions for all waves in a given hover.

### 3.5.2 Deep Learning for Timestack-image Wave Crest Detection

Traditional computer vision techniques, e.g. Canny or Sobel edge detection, often have difficulty accurately identifying the location of wave crests when foam is persistent (Stringari et al., 2019). Because manually identifying wave crests (e.g. through ground-truth annotations) can be time-consuming, we propose using a deep learning approach as an automated annotation tool (e.g. Collins et al., 2020). Our method is not intended to provide new information, but rather to aid in the tedious process of identifying wave crests, which we define as the location between the solid block of white water that is characteristic of a wave roller and the more interspersed longer tracks of foam on the back side of a broken wave (Figure 3.5.2 insert).

The training/validation dataset consists of 20 timestack-images with sparse (not for all waves) ground-truth provided by binary hand annotations of wave crests. To include a range of wave, lighting, and bathymetry conditions, one transect from each hover in Fall 2021 at Torrey Pines is included. Training used 16 randomly selected timestack-images and validation used 4. Note that because the deep learning approach is used here simply as an annotation tool, the specific choices of parameters of the neural network are of little importance.

Figure 3.5.2 shows the workflow for the crest-detection. An input timestack is provided and a binary output image of the detected crests is returned. An example of the output wave crests superimposed on the timestack image can be seen in the insert. Further details on the wave crest detection algorithm can be found in Appendix 3.A.

### 3.5.3 Surf Zone Depth from Crest-tracking

The surf zone method estimates the celerity of individual wave crests observed in timestacks using a deep learning neural network. Depth is recovered by inverting celerity using linear and nonlinear shallow water dispersion.

**Table 3.5.1.** cBathy 2.0 Parameters (Holman, Bergsma, 2021)

| Parameter | Description | Value |
|---|---|---|
| $\Delta t$ | Time series sampling interval | 0.5s |
| $(\Delta x_p, \Delta y_p)$ | Pixel spacing | (5,5)m |
| $(\Delta x_m, \Delta y_m)$ | Analysis point spacing | (5,25)m |
| $(h_{min},\ h_{max})$ | Min/Max acceptable depth | (0.25, 20)m |
| $(L_x, L_y)$ | Analysis smoothing scale | (25,100)m |
| $\kappa$ | Smoothing scale | 3 |
| $f$ | Analysis frequency bins, range and df | $[0.055 - 0.25 : 0005]$ Hz |
| $N_{keep}$ | Number of frequency bins to retain | 4 |

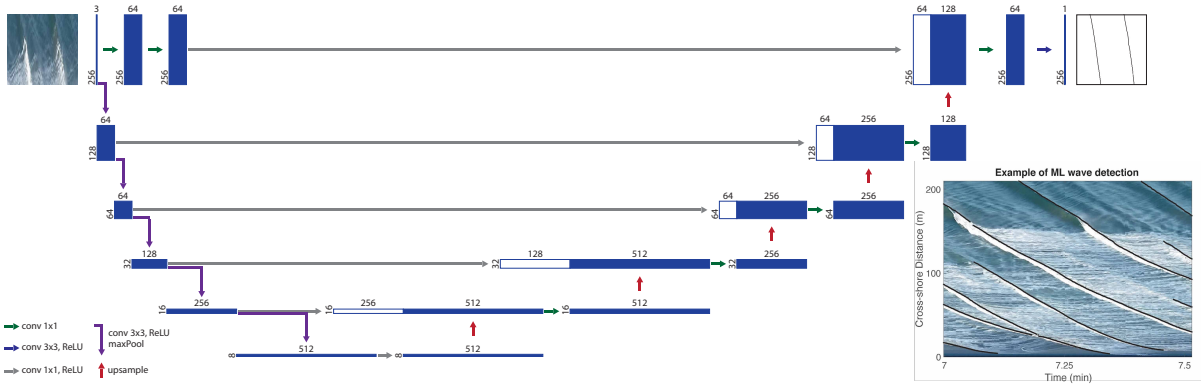


**Figure 3.5.2.** U-Net Architecture: Number of features on top and resolution (number of pixels) to the left of the blocks. (insert) Example of ML wave crest detection.

Crest tracks are extracted from the U-Net binary output images (Figure 3.5.2). The 2-D binary image is reduced to 1-pixel (0.1 m, 0.1 sec) wide curves, and the $(x, t)$ coordinates of the individual curves are detected by 1) finding the first offshore instance of the curve (where no other black points are found previously in time and further offshore in a given area), 2) following the crest, with the next coordinate detected by the shortest Euclidean distance between black points that follow in time and are onshore of the current points, and 3) removing short curves ($< 7.5$ sec). Figure 3.3.1 c,d shows the difference between the initial U-Net output and the wave crests accepted for computing celerity. The phase speed of each crest, computed by the best-fit slope (RANSAC) between two points in the 15m vicinity of each $(x, t)$ coordinate along the curve, is interpolated onto a regular grid of 0.1m intervals. The same gridding discretization (0.1 m, 0.1 sec) is used everywhere. At large offshore distances, a single video pixel can span multiple grid points, resulting in degraded accuracy. To address this issue, a pixel resolution cutoff is applied. Any pixel that covers more than 2 grid points is removed.

The 'breakpoint transition' (BP) method uses linear and nonlinear methods in their respective best areas by imposing a wave-by-wave step function $\gamma_s$ as a function of cross-shore distance, with $\gamma_s = 0$ prior to breaking and $\gamma_s = 0.42$ post-breaking. The location of the breakpoint for each accepted wave track is determined heuristically (example given in Appendix 3.B). The step function $\gamma_s = (0, 0.42)$ is imposed only at x-locations with at least 10% of the maximum number of phase speed estimates at any $x$-location during that hover (with the minimum number of estimates included typically between 5 and 11). The average of the individual $\gamma_s = (0, 0.42)$ step functions yields an effective $\gamma(x)$ (Figure 3.5.1 e,f green line) that is used to define the "bad" (interpolated over) region for cBathy (Section 3.5.1). The transition from nonbreaking (here linear) to breaking, nonlinear domains through shoaling in the physical world is captured by the effective $\gamma(x)$ changing gradually from 0 to 0.42.

For each wave track, we invert for depth following linear shallow water theory

$h = c^2/g$ ('Linear', Figure 3.5.1), or with the nonlinear estimation (Eq. 3.3, with $\gamma = 0.42$ for 'Nonlinear', and $\gamma_s$ for 'BP' in Figure 3.5.1). The average depth is then computed from the individual tracks with a 5-m Gaussian smoothing applied. Following cBathy methodology, depths are then converted to an elevation (in NAVD88 datum) with a tidal offset, using the average water level over each UAV hover at the nearby La Jolla tide gauge (NOAA station 9410230).

### 3.5.4 Generating composite profiles

Profiles spanning from the shoreline to 10-m depth ("composites") are constructed by combining improved surf zone bathymetry estimates with cBathy offshore estimates (Figure 3.5.3 d,h). The beginning of wave breaking (timestack derived, Appendix 3.B) is used as the switching location between BP and cBathy estimates. Timestacks are used both to estimate surf zone depths and to define the shoreward limit of cBathy applicability, where cBathy and crest-tracking are joined. Example depth estimates have (Figure 3.5.3 a-d) varying tidal level and approximately constant wave height and (Figure 3.5.3 e-h) varying wave height and approximately the same tide level. The large surf zone depth errors ($\langle \text{RMSE} \rangle = 1.42$m, Figure 3.5.3 a,e, Table 3.5.2) in raw, unfiltered cBathy are reduced by interpolating across the span identified as incorrect with timestacks (Figure 3.5.3 b,f). Errors in the surf zone are further significantly reduced using the phase speeds of individual crests and applying a depth inversion individually before smoothing (Gaussian-weighted 5-m moving average) and averaging (Figure 3.5.3 c,g).

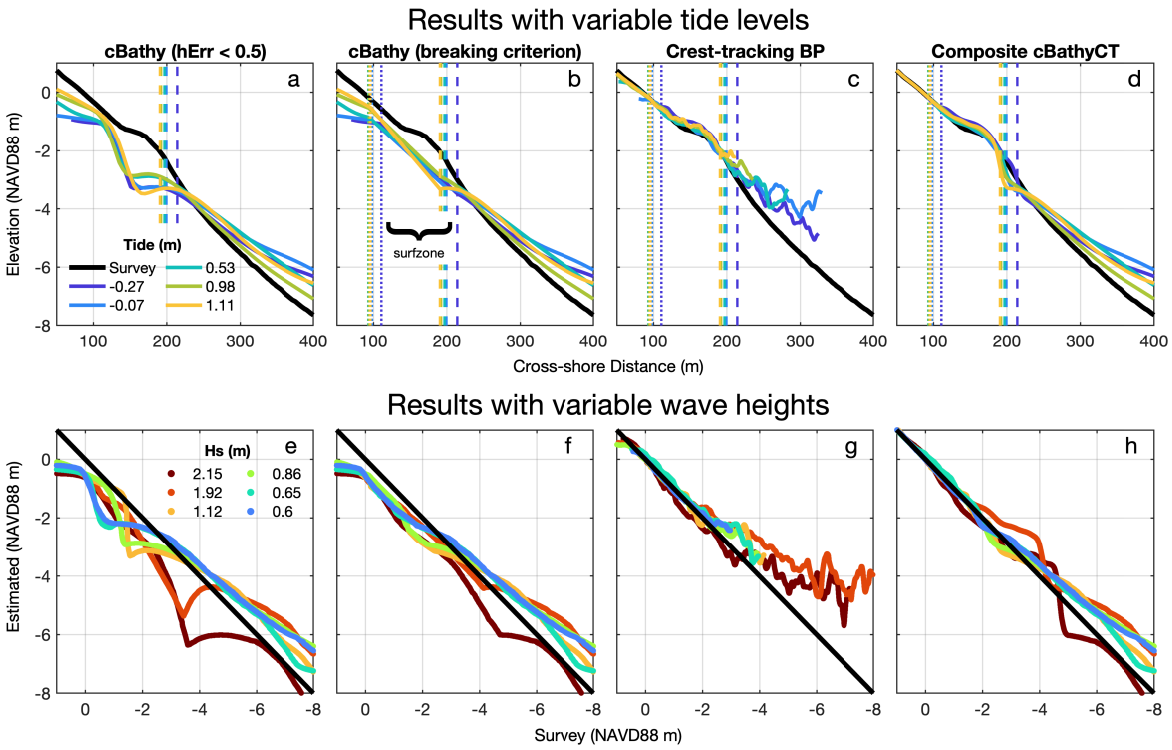


**Figure 3.5.3.** Bathymetry estimates at Torrey Pines MOP 582. Upper panels show July 7th, 2020 elevation versus cross-shore distance for varying tide levels (1.3m max difference, legend). The dotted vertical line (upper panels) marks the shoreward edge of surf zone and offshore extent of subaerial survey where the crest tracking method (c,g) is fused with insitu data for composite cBathyCT (d,h). Vertical dashed lines mark beginning of wave breaking where cBathy (b,f) and crest-tracking bathymetry (c,g) are stitched together to form the composite (d,h). Bottom panels show estimated versus observed elevation for varying wave heights (legend) near mid-tide on various dates (Table 3.4.1). Solid black is ground truth. Bathymetry estimates are shown from cBathy interpolated over hErr $< 0.5$ (a,e), cBathy interpolated over the breaking region (b,f), breakpoint transition crest-tracking (c,g) and cBathyCT (d,h). Owing to the non-planar beach profile, the stitching location varied little with tide (top panel, dotted line). Fit statistics for various composites are in Table 3.5.2.

**Table 3.5.2.** RMSE and Bias statistics for composite models (depth < 10m) at Torrey Pines. surf zone goes from the beginning of wave breaking to the SWL line. Offshore goes from the beginning of wave breaking to 500m offshore.

| Composites | cBathy (hErr < 0.5m) | cBathy (breaking parameter) | cBathy (nonlinear) | cBathyCT |
|---|---|---|---|---|
| ⟨**RMSE**⟩ (m) | | | | |
| Surf zone | 0.81 | 0.55 | 0.44 | 0.17 |
| Offshore | 0.90 | 0.90 | 0.92 | 0.87 |
| Full profile | 0.9 | 0.79 | 0.76 | 0.68 |
| ⟨**Bias**⟩ (m) | | | | |
| Surf zone | -0.56 | -0.41 | -0.29 | 0.06 |
| Offshore | 0.58 | 0.58 | 0.61 | 0.58 |
| Full profile | 0.12 | 0.19 | 0.25 | 0.38 |

A subaerial beach profile obtained from a low tide RTK-GNSS survey is combined with the subaqueous bathymetry to obtain a full profile (Figure 3.5.3 d,h). When both the survey and bathymetric estimations are available in the same cross-shore location, the low-tide survey is preferentially selected. By overriding the inner surf zone/swash zone bathymetry results with a ground-truth survey, we avoid potential issues with wave setup or large depth over-estimations near the shoreline (Sénéchal et al., 2004; Power et al., 2010; Fiedler et al., 2021). If no overlapping region between survey and bathymetry estimates exists, the distance between the two are linearly interpolated. The composite profile has smaller errors ($\langle$RMSE$\rangle$ and $\langle$Bias$\rangle$) in $<$ 3m depth than either cBathy version. Composite profile normalized errors ($\langle$RMSE$\rangle/h$) vary between $0.1 - 0.2$, with largest values near the shoreline (Figure 3.5.4). RMSE values offshore of the surf zone are similar because all methods use cBathy. The mean RMSE varied between $0.05 - 1.75$m depending on conditions (including UAV height, lighting, Hs and other factors). Although using $\gamma(x)$ to determine the bounds of the surf zone for interpolation within cBathy (rather than hErr) improves the estimates, only breakpoint crest-tracking accurately captures the terrace in a single hover.

## 3.6 Discussion

### 3.6.1 Error sources

Holman et al. (2013) proposed mitigating the surf zone gap in cBathy by Kalman filtering cBathy estimations together, based on hErr, over a tidal cycle. However, tidal variation from $-0.27 - 1.13$ NAVD88m did not shift the surf zone gap location sufficiently to span the full profile (Figure 3.5.3 e). Rather than simply a shoreward shift of a constant width surf zone as on a plane beach, the observed surf zone both widened and shifted onshore. The location where cBathy estimates fail changes with tidal elevation (Figure 3.6.1) but not enough to generate a full accurate bathymetry from cBathy alone. Composite

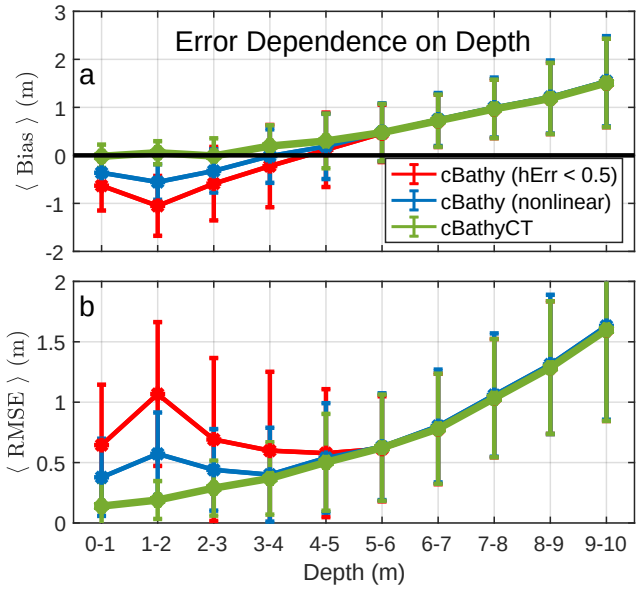


**Figure 3.5.4.** Torrey Pines composite bathymetry mean statistics from 59 full profiles, binned by depth (solid curves). (Upper) mean Bias, (lower) mean RMSE. Curve color indicates surf zone method: (red) cBathy estimate with hErr $< 0.5$m, (blue) cBathy with breaking criterion for surf zone interpolation and nonlinear gamma correction, (green) cBathy with breakpoint transition crest-tracking in the surf zone (cBathyCT). Seaward of breaking, methods all use cBathy and curves overlap. Depth is relative to the still water line, accounting for tides but not setup. Error bars show standard deviation. For cBathyCT composite, the normalized standard $\langle \text{RMSE} \rangle / h = 0.27, 0.13, 0.11,$ and $0.15$ for bin centered on $0.5, 1.5, 4.5,$ and $8.5$m respectively.

profiles are relatively insensitive to tide level (Figure 3.5.3 d).

The largest (un-normalized) $\langle \text{RMSE} \rangle$ and $\langle \text{Bias} \rangle$ are in the deepest water $h = 8 - 10$m (Figure 3.5.4, Table 3.5.2) where historical ground-truth (not shown) depths change relatively little ($\langle \text{RMSE} \rangle \sim 0.5$m). Offshore errors could be reduced using historical insitu profiles to constrain the range of plausible offshore depths. The extent to which previous ground truth profiles improve remote estimates (e.g. Kalman filtering) depends on both the characteristics of the available insitu bathymetry and the beach variability. Kalman filtering is most effective for a beach that is known (from past, extensive, accurate surveys) to change little, or to change predictably in response to changing wave conditions.

UAV rectification uses ground (stability) control points that are limited to the

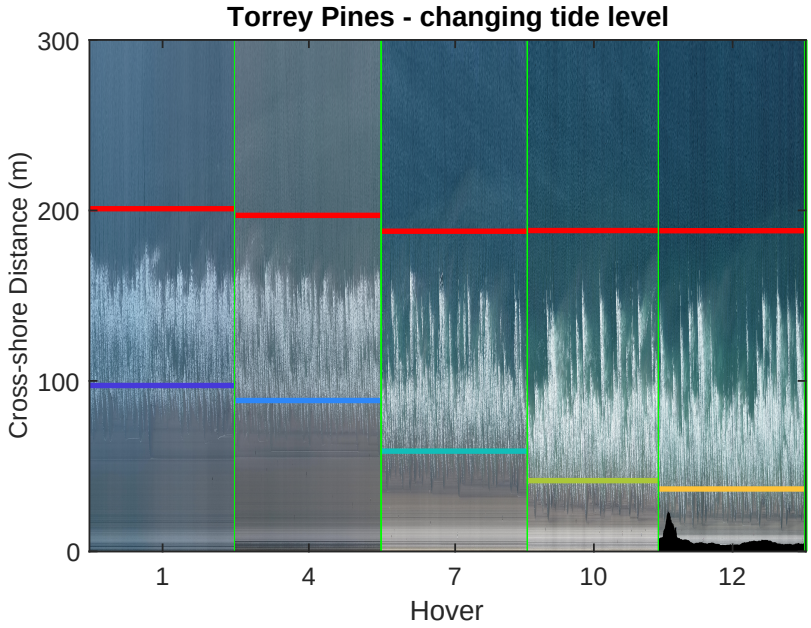


**Figure 3.6.1.** Torrey Pines MOP 582 on July 7th, 2020. Wave height Hs $\sim$ 0.89m. Timestacks (intensity versus time on a cross-shore transect) for 5, 17-min hovers during flood tide, separated by green vertical lines. The waterline (colored horizontal lines, Figure 3.5.3 a) gradually moves onshore 60m (from $x = 97$m to 37m) during flood (1.37m tide increase). The shoreward limit of accurate cBathy (solid red lines) includes breaking in the 50m-wide sample window. The offshore boundary moves onshore only 12m (from $x = 200$m to 188 m) owing to a small terrace (Figure 3.4.1) that triggers breaking.

bottom of the field of view, approximately in a straight line, and rarely near the image offshore edge. The resulting roll and pitch errors are corrected with a cross-shore shift (mean shift = 5.4m) when combining remotely-sensed subaqueous and observed subaerial surveys. Including horizon tracking to the least-squares fitting of the camera extrinsics might reduce these offsets and errors in the deepest water (Bergsma et al., 2019; Tsukada et al., 2020).

Normal incidence is not assumed in cBathy, but is assumed with surf zone crest-tracking using timestacks. Waves in the present dataset are primarily normally incident with the largest 10m-depth wave obliquity at Torrey Pines at 12° (Table 3.4.1). Assuming Snell's Law, and using 5m as a maximum surf zone depth, errors from neglecting wave obliquity are usually less than 2%. Larger wave obliquities may lead to more obvious

overestimation of phase speeds and depth, however, the current dataset limits testing the crest-tracking (CT) part of cBathyCT for obliquely incident waves. Similarly, seas with very broad spectra and therefore many different celerities present in a single timestack may lead to bad estimates with the present surf zone correction. cBathy Phase 1 frequency-wavenumber pairs can be used to determine the appropriateness of a narrow spectrum assumption, by identifying the frequency spread of the 4 most coherent frequencies. Further testing of the method in a larger variety of wave conditions is required to determine the limits of both the normal incidence and narrow spectrum assumptions.

The shallow water approximation for $c$ used in crest-tracking is valid in the present depths ($< 5$m) with long-period swell ($T_p > 9$sec) but finite depth theory could readily be used. The peak period as determined from the timestack and a nearby buoy in 17m depth (NOAA NDBC Station 46266) usually differs by less than 1 sec. Outliers in single hovers are removed by using the median of 3 flights rather than a single flight (Figure 3.6.2), but overall statistics do not consistently improve. Full profile single-hover profile bias is low owing to cancelling errors ($\langle$RMSE$\rangle$ is high) (Table 3.5.2).

### 3.6.2 Applicability to other sites

Pre-training a U-Net network on a large surf zone dataset provides the network with a good general feature representation. Additional training would be needed for sites with much different incident waves or breaking wave characteristics. A strength of the present methodology is that deep learning is only used as an annotation tool, automating the extraction of crest speeds from timestack-image wave detection, while allowing for depth estimates from different wave dispersion models (here Eq. 3.1 - 3.3).

The crest-tracking BP method performs similarly (to Torrey Pines) on the terraced profile at SIO (Figure 3.4.1), with mean $\langle$RMSE$\rangle = 0.08$m and $\langle$Bias$\rangle = -0.02$m in the surf zone. Performance was also good at Cardiff on MOP 668, 669, but was degraded by a bedrock reef at the southern edge of the field of view (MOP 667, Figure 3.6.3 a).

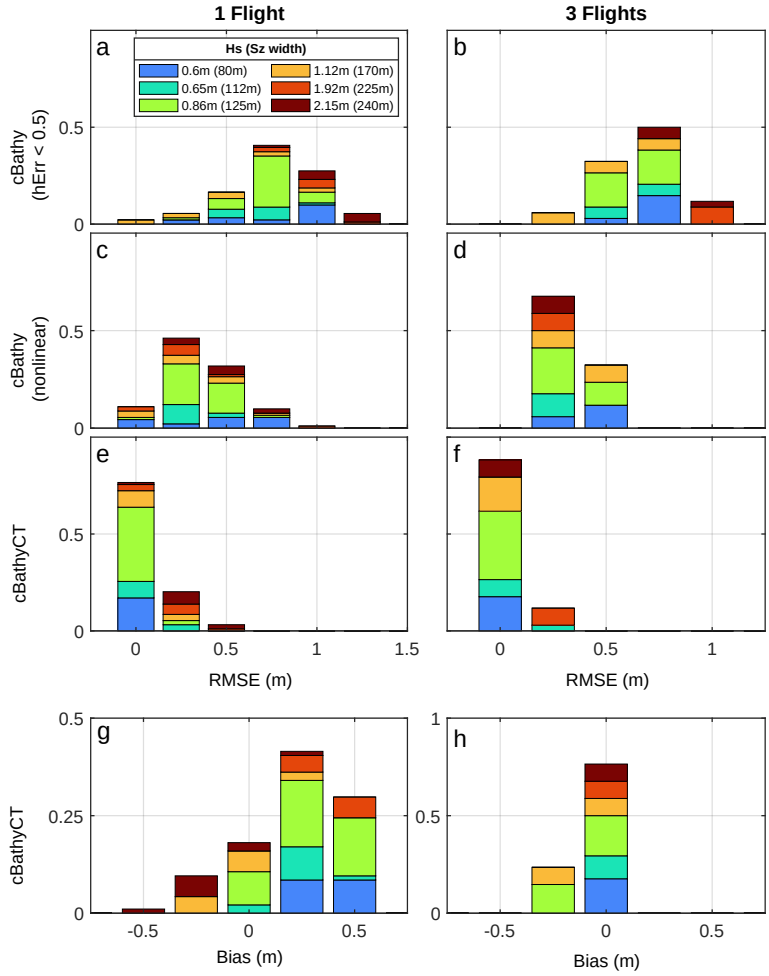


**Figure 3.6.2.** Histograms of depth inversion errors at Torrey Pines (for the surf zone region) for different methods (stacked vertically) on 59 transects (left) 1 hover and (right) median of 3 hovers. (a,b) cBathy with interpolation where hErr $< 0.5$m, (c,d) cBathy with breaking criterion for surf zone interpolation and nonlinear gamma correction, and (e,f) composite using breakpoint crest-tracking cBathyCT, (g,h) mean bias of cBathyCT. Colored by offshore Hs (legend). Outliers with the largest bias and RMSE are removed with 3 hovers. Fit statistics in Table 3.5.2. Probabilities (vertical axis) sum to 1.0.

The wave detection algorithm annotates the images accurately (Figure 3.6.3 b), but the estimation and inversion from $c$ to depth is inadequate. Nonlinear frequency doubling (e.g. Elgar et al., 1997) on the flat terrace (between $x = 120$ and 200m, Figure 3.6.3 a) may create additional crests that would confound simple crest-conserving inversions.

The effect of alongshore variations in bathymetry on phase speed and crest direction is neglected here, but could be included in more sophisticated 2D inversions both within and seaward of the surf zone.

The $\gamma = 0.42$ used here is based on historical observations at Torrey Pines (Thornton, Guza, 1982). LiDAR wavescans concurrent with UAV hovers yield a local $\gamma(x)$ (Figure 3.6.4), computed from direct sea surface elevation measurements ($H_{m_0}$) and insitu surveys (Fiedler et al., 2021). The average $\gamma$ over the surf zone varies between $0.55-0.74$, decreasing offshore. Deviations in gamma estimations at these sites do not significantly affect the bathymetric estimations; mean $\langle \text{RMSE} \rangle = 0.25$m is minimum over all available transects for $0.4 < \gamma < 0.5$, increasing only slightly to 0.3m for $0.6 < \gamma < 0.8$. Yoo et al. (2011) reported $\gamma = 0.6$ in their crest-tracking study. Note in 'low' wave conditions (Hs $< 0.75$m), linear crest-tracking ($\gamma = 0$) and BP perform comparably well with $\langle \text{RMSE} \rangle \sim 0.18$m in the breaking region. Not surprisingly, corrections for wave nonlinearity are most important when Hs is largest. The present approach ($\gamma = 0.42$) likely fails in shallow water on steep slopes where plunging waves with $\gamma > 0.8$ are expected. Concurrent video and LiDAR (e.g. Figure 3.6.4) of $\gamma$ and $c$ would enable application of the present method to sites with much different breaking wave characteristics and $\gamma$.

Results for individual 17 min hovers are encouraging. The dependence of cBathy and crest-tracking error statistics (e.g.$\langle \text{RMSE} \rangle$) on record length is unknown, and likely varies with wave conditions and bathymetry. Errors in composite profiles do not depend significantly on tide level for the present limited range of conditions but may depend on tide level on barred bathymetry. Additional model testing and calibration is needed.

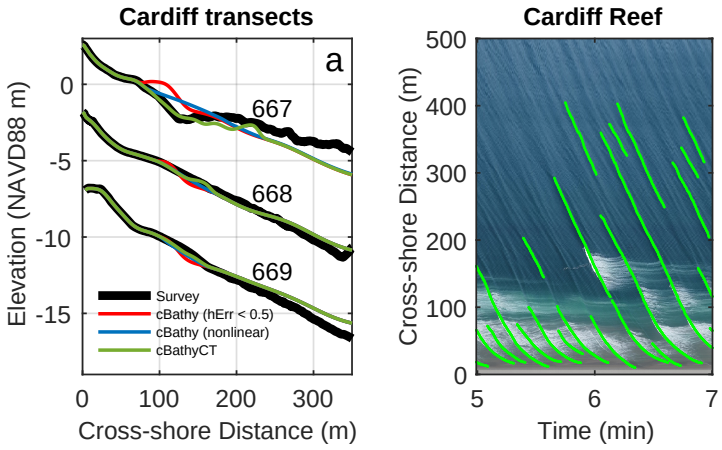


**Figure 3.6.3.** (left) Depth versus cross-shore distance from 1 hover on MOP 667 - 669 (stacked with a 5m vertical offset). Ground truth (black), cBathy with hErr $< 0.5$m (red), cBathy with a nonlinear correction (blue) and cBathyCT (green). Bedrock reef on MOP 667 from $x = 125$m to 1km offshore. (right) Results of the deep-learning crest-tracking algorithm on MOP 667. The wave crest detection neural network was not trained on reef-like profiles, but may detect wave crests accurately enough for use in alternative (e.g. 2D nonlinear) depth inversions.

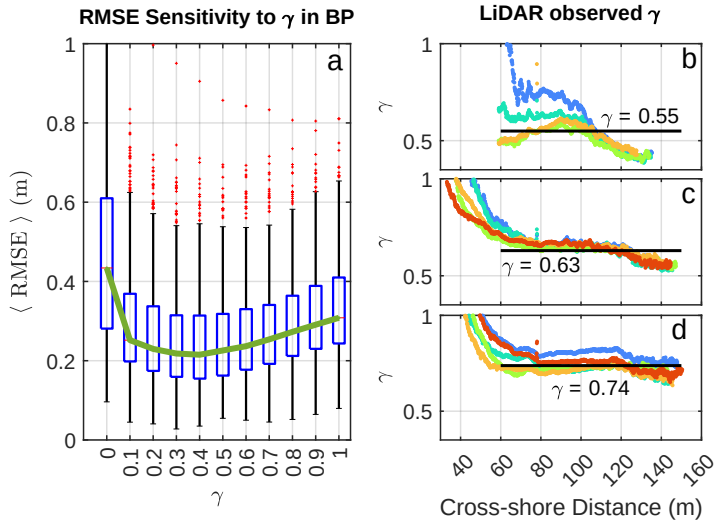


**Figure 3.6.4.** (left) for 468 transects, median RMSE versus $\gamma$ (green curve), (boxes) 50% quantile, (black bars) 90% quantile for crest-tracking BP method in the surf zone (outliers red dots). Minimum $\langle$ RMSE $\rangle$ at $\gamma = 0.4$ increases $< 20\%$ for $0.1 < \gamma < 0.7$. (right) surf zone LiDAR measured $\gamma = H_{m_0}/h$ versus cross-shore distance for (b) Nov 2nd, 2021, Hs = 1.12m, (c) Oct 26th, 2021, Hs = 1.92m, (d) Dec 15th, 2021, Hs = 2.15m, colored by hover. Black horizontal line is mean $\gamma$ over surf zone.

## 3.7 Acknowledgments

This study was funded by the U.S. Army Corps of Engineers (W912HZ1920020) and the California Department of Parks and Recreation (C19E0026). Data were collected and processed by the Coastal Processes Group field team members Lucian Parry, Rob Grenzeback, Kent Smith, Brian Woodward, Greg Boyd, and Mele Johnson. Michele Okihiro organized logistics.

Chapter 3, in full, has been submitted for publication as it may appear in Coastal Engineering 2023. A.M.Z. Lange, J.W. Fiedler, M.A. Merrifield, and R.T. Guza. The dissertation author was the primary investigator and author of this paper.

## 3.A Wave-crest Detection Deep Learning Algorithm

The U-Net architecture (Ronneberger et al., 2015) is well established for segmentation tasks such as crest detection. U-Nets are based on an Encoder-Decoder architecture, with skip connections from the Encoder to the Decoder at the different levels to be able to recover resolution. The Encoder provides a compact feature representation (many features, but little resolution) of the input image by applying convolutions followed by a maxpool downsampling at multiple levels (more features, less resolution). The Decoder takes the compact feature representation and provides a classification for each pixel in the image at full resolution by upsampling followed by concatenation and convolutions at multiple levels (fewer features, more resolution). We used a modified version of the U-Net with a ResNet18 encoder pre-trained on the ImageNet dataset (Usuyama, 2018) (Figure 3.5.2).

Wave crest detection uses a limited neighborhood area in timestack-images. Training and prediction can use small high-resolution image tiles, increasing the training dataset size and reducing the deep learning network complexity. To augment the training dataset, image tiles are sampled at arbitrary locations in the image. Timestack-images are 5000

pixels cross-shore direction and a time-dependent width of 600 pixels per minute. For the training, we sample 1000 256 x 256 image tiles from a timestack-image. For the prediction, we divide the timestack-image into overlapping 256 x 256 image tiles. The border of the predicted image tiles (therefore the overlap) has relatively large errors and is not used. Thresholds such as minimum length and width of detected track can be specified.

A binary cross-entropy (BCE) loss function is used for binary classification (limited to a region around the sparse ground-truth), with a Root-Mean-Square (RMS) optimizer and an adaptive learning rate scheduler. The model is trained for 50 epochs, with a batch size of 8 and an initial adaptive learning rate of 0.0001. Training and validation losses remained constant after 40 epochs. Model predictions are made after 50 epochs. The deep learning approach was implemented in Python and PyTorch. A desktop computer with a GeForce GTX 1660 GPU required 50 hours to train the model for 50 epochs, with predictions taking 2.5 min per timestack.

## 3.B Breakpoint locator

The breakpoint location is determined with an algorithm based on pixel intensity gradients along a wave track. Thresholds for broken and unbroken waves are determined by fitting two Gaussian distributions to the image pixel intensity histograms (Figure 3.B.1 a) and determining the mean of the distributions. Individual waves track may include only broken or only unbroken waves, with relatively small gradients, and high or low pixel intensity levels (red and black circles respectively, Figure 3.B.1 a). Tracks that include the breakpoint begin unbroken (below the low threshold), with a sharp gradient (purple dot, Figure 3.B.1 c) when breaking begins, and a high but stable pixel intensity above the high threshold (green circle, Figure 3.B.1 b). The breakpoint location is set to the location of maximum gradient. Residual foam can obscure sharp breakpoint gradients, and each wave track goes through an iterative process to determine if it contains the breakpoint. Failing a

conclusive result with the first pass with the strictest thresholds, less stringent thresholds are applied until the segment is characterized (examples provided in the attached code). The breaking location estimated by the algorithm and visual inspection agree.

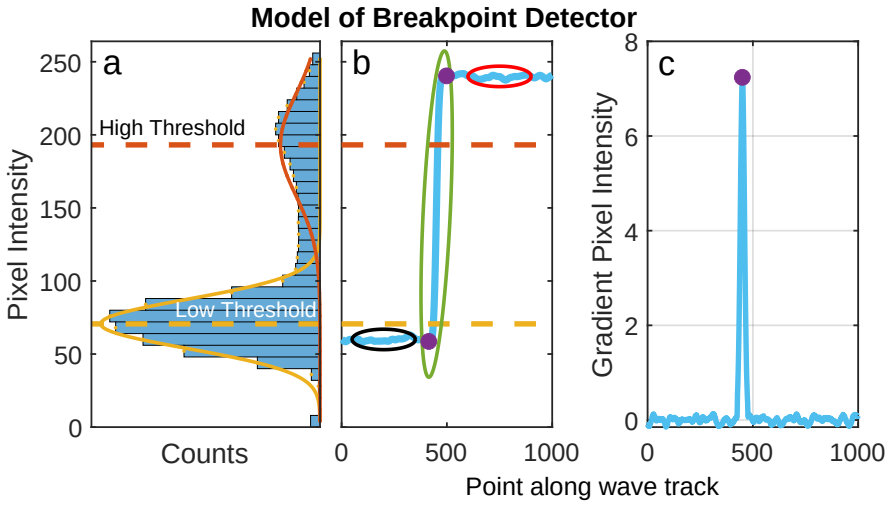


**Figure 3.B.1.** Schematic of breakpoint location using gradients of pixel intensity. (left) histogram of pixel intensity of the full image ($10^7$ counts are shown) typically have two maxima and each is fit to a Gaussian distribution, centered around high and low thresholds (red and yellow respectively). (middle) idealized pixel intensity versus location on wave track segment completely within (all broken) or completely seaward (unbroken) of surf zone (red and black circles, respectively). Sharp gradients (green) indicate breakpoint. (right) idealized pixel intensity gradient versus along-track location.

# Chapter 4

# Free infragravity waves on the inner shelf: Observations and Parameterizations at two Southern California beaches

## 4.1 Abstract

Co-located pressure and velocity observations in 10-15m depth are used to estimate the relative contribution of bound and free infragravity (IG) wave energy to the IG wave field. Shoreward and seaward going IG waves are analyzed separately. At the Southern California sites, shoreward propagating IG waves are dominated by free waves, with the bound wave energy fraction $< 30\%$ for moderate energy incident sea-swell and $< 10\%$ for low energy incident sea-swell. Only the 5% of records with energetic long swell show primarily bound waves. Consistent with theory (Hasselmann, 1962) bound wave energy scales as the square (frequency integrated) sea-swell energy, with a higher correlation with swell than sea energy. The observed linear dependency of free shoreward IG energy on local SS wave energy and tide is included in a parameterization. Free (random phase) and bound (phase-coupled) IG waves are included in numerically simulated time series for shoreward IG waves that can be used to initialize ($\sim$ 10m depth) numerical models for wave runup. Seaward and shoreward propagating free IG wave energy vary in 10-15m

depth, and are both parameterized with good skill ($R^2 \sim 0.90$).

## 4.2 Introduction

Infragravity (IG) waves are low-frequency surface-gravity ocean waves with periods typically between 25-200s. IG waves were first observed (Munk, 1949; Tucker, 1950) seaward of the surfzone, traveling shoreward with the group velocity of short-period wind-generated waves and $\sim 10\%$ of their amplitude. IG waves can contribute significantly to runup (Ruggiero, 2004; Stockdon et al., 2006; Becker et al., 2016; Fiedler et al., 2019, 2021; Lange et al., 2022), sediment transport (Aagaard, Greenwood, 1994, 2008; Baldock et al., 2010; De Bakker et al., 2016), harbor seiches (Okihiro et al., 1993; Ardhuin et al., 2010) and earth hum (Rhie, Romanowicz, 2006; Webb, 2007).

### 4.2.1 Bound Waves

"Bound waves" are shoreward propagating IG waves generated on the inner shelf (seaward of the surfzone) by the second-order nonlinear interaction of higher frequency surface gravity waves, and are 180° phase-locked with the wave envelope (Longuet-Higgins, Stewart, 1962). Shoaling, shoreward propagating sea-swell (SS) frequencies interact and transfer energy to their sum (higher-order harmonics) and difference (infragravity) frequencies through nonlinear triad interactions (Hasselmann et al., 1963; Dongeren van et al., 2007). As SS waves shoal, the bound wave approaches resonance, lags behind the wave group, and is eventually a 'free' wave (on the dispersion curve) that propagates to shore (List, 1986; Battjes, 2004; Bakker de et al., 2015). Throughout the short wave (e.g. sea-swell) surf zone, free IG waves can acquire and lose energy from SS waves and can themselves shoal and break (Battjes, 2004; Thomson et al., 2006; Henderson et al., 2006; Dongeren van et al., 2007; Ruju et al., 2012; Bakker de et al., 2014). At the shoreline, free IG waves can reflect and propagate seaward (Elgar et al., 1994; Thomson et al., 2006).

Bound infragravity spectral energy $E_{IG}^{bound} = \int_{IG} \mathbf{E}^{bound}(f)df$ is estimated from

second-order nonlinear wave theory (Hasselmann, 1962; Herbers et al., 1995a),

$$\mathbf{E}_{IG}^{bound}(\Delta f, \Delta\theta) = 2\int_{\Delta f} D^2 S(f,\theta_1) S(f+\Delta f,\theta_2) df, \tag{4.1}$$

$$D = \frac{-gk_1k_2\cos(\Delta\theta)}{2\omega_1\omega_2} + \frac{1}{2g}(\omega_1^2+\omega_2^2+\omega_1\omega_2) + C\frac{g(\omega_1+\omega_2)}{(gk_3\tanh(k_3h)-(\omega_1+\omega_2)^2)*\omega_1\omega_2},$$

$$C = (\omega_1+\omega_2)*\left(\frac{\omega_1\omega_2}{g}\right)^2 - k_1k_2\cos(\Delta\theta) - \frac{1}{2}\left(\frac{\omega_1k_2^2}{\cosh^2(k_2h)} + \frac{\omega_2k_1^2}{\cosh^2(k_1h)}\right),$$

with wavenumber $k$, angular frequency $\omega$ $(= 2\pi f)$ and where the sea-swell frequency-direction spectra $S(f,\theta)$ can be estimated from a PUV, a pitch-roll buoy (Kuik, 1988), or a regional wave model. The interaction coefficient $D$ is computed for the difference frequency $(\Delta f)$ of every frequency pair $(f_1, f_2)$ and if assuming directionally spread waves (2D), every difference direction $(\Delta\theta = \theta_2 - \theta_1 + 180°)$. $D$ varies strongly as a function of $\Delta\theta$, depth and SS frequency $f$. In shallow water, $D$ is maximum $(D_{max})$ for co-linear $(\Delta\theta = 0)$ waves, and 1D theory $(\Delta\theta = 0)$ provides an upper limit on the amount of bound wave energy. $D$ decreases quickly with increasing $\Delta\theta$; $\Delta\theta = 30°$ results in $D \sim 25\% D_{max}$ (Herbers, Guza, 1994)). The theoretical sensitivity of 2D bound wave energy to $S(f,\theta)$ and the fundamentally low resolution of a single PUV directional estimator limits the accuracy of the present 2D bound wave estimates. Due to the frequency dependence of the coupling coefficients, swell (8-25s) tends to produce larger bound waves than sea (4-8s) (Okihiro et al., 1992).

Bound IG waves can also be estimated with bispectral analysis (Hasselmann et al., 1963; Kim et al., 1980; Elgar, Guza, 1985). The third-order spectrum (bispectrum) detects nonlinear phase coupling between wave triads with angular frequencies $\omega_1$, $\omega_2$, $\omega_{1+2}$. The bispectrum is the expected value of the triple product of complex Fourier coefficients, $B(k,l) = \tilde{E}[X_kX_lX_{k+l}]$. With no nonlinear coupling of the three frequencies,

the bispectrum vanishes. The normalized magnitude of the bispectra (**b**, bicoherence),

$$\mathbf{b}(f_1, f_2) = \frac{B(f_1, f_2)}{\sqrt{\mathbf{E}(f_1)\mathbf{E}(f_2)\mathbf{E}(f_1 + f_2)}} \tag{4.2}$$

provides a measure of the strength of the coupling between the three waves. The phase of the bispectrum (biphase), assuming high bicoherence values, corresponds to the phase lag between the bound IG wave and the SS wave group (Elgar, Guza, 1985). Bispectral analysis can also be used to compute the forced wave spectral density by integrating the bispectrum over all frequency pairs for a given difference frequency (Herbers, Guza, 1994),

$$\mathbf{b}_i(\Delta f) = 2\int_{\Delta f}^{\inf} df B(f, \Delta f) / \sqrt{2\int_{\Delta f}^{\inf} df \mathbf{E}(f + \Delta f)\mathbf{E}(f)\mathbf{E}(\Delta_f)}, \tag{4.3}$$

$$\mathbf{E}_{IG}^{forced}(\Delta f) = \alpha(\Delta f)|b_i(\Delta f)|^2 \mathbf{E}(\Delta f), \tag{4.4}$$

and the bias term $\alpha$ can be computed from the bound wave theory.

### 4.2.2 Free Waves

Free waves contribute significantly to IG waves (Gallagher, 1971; Huntley et al., 1981; Oltman-Shay, Guza, 1987; Okihiro et al., 1992; Zijlema, 2012; Fiedler et al., 2018; Smit et al., 2018). 'Edge' waves are free waves trapped on a sloping beach by shoreline reflection and back-refraction by the increasing water depth (Eckart, 1951). Edge waves are sensitive to geography, with the amount of trapping depending on the continental shelf and beach topography (Herbers et al., 1995b). Seaward propagating IG waves that propagate freely from the shoreline across the shelf to deep water are known as 'leaky' waves (Webb et al., 1991; Ardhuin et al., 2014; Rijnsdorp et al., 2021). Ardhuin et al. (2014) and Rawat et al. (2014) parameterize seaward-going free wave energy for use as an incident boundary condition for global model WAVEWATCH III, but the free IG wave climate on the inner shelf is poorly understood.

Previous work in Duck, NC, Southern California, and Hawai'i, USA and the North Sea have investigated the fraction of IG energy contained in the bound component, giving an indication of the amount of free shoreward wave energy. Numerous studies at Duck, NC ($\sim 8-13$m depth) (Elgar et al., 1992; Herbers, Guza, 1994; Ruessink, 1998; Reniers, 2002) found that the bound wave fraction was typically between $10-20\%$, with higher values above 30% (and up to 100%) only during the most energetic SS conditions. In the North Sea ($\sim$ 30m depth), IG wave conditions are always free wave dominant and only during the peak of storms is the fraction bound $\geq 50\%$ (Reniers et al., 2021). At beaches in Southern California and Hawai'i ($\sim 8-13$m and 183m depth) (Okihiro et al., 1992) up to 50% of the IG energy is at times attributed to bound wave energy. The fraction bound is also heavily dependent on the water depth, e.g. (Elgar et al., 1992) observed twice the bound fraction in 8m depth compared to 13m depth in Duck, NC. Torrey Pines has long been a study site for refractively trapped waves (Huntley et al., 1981; Guza, Thornton, 1985; Oltman-Shay, Guza, 1987; Oltman-Shay, Howd, 1993; Thomson et al., 2006), with significant trapped IG energy detected shoreward of 15m water depth. This refracted energy then propagates onshore as free waves. While these trapped waves are not bound to the SS wave groups, because they were originally generated locally, there will be a dependence on local SS wave conditions.

While SS waves are relatively well observed with buoys (Behrens et al., 2019) or satellites (Ribal, Young, 2019; Qin, Li, 2021), IG waves are not, due to measurement sensitivites. IG waves are typically observed with bottom-mounted pressure and/or current sensors. However, the practical limitations of direct observations of infragravity waves motivates efforts to parameterize IG energy for use in nearshore and global models. Bound wave theory has been implemented as an offshore IG boundary condition in laboratory studies where the wavemaker is carefully controlled to create only a shoreward propagating bound IG wave and (ideally) to absorb seaward propagating IG waves (Noorloos van, 2003; Van Thiel De Vries et al., 2008; Ruessink et al., 2013; Altomare et al., 2020, and resulting

papers). Bound waves have also been used as the offshore boundary condition in field settings (Roelvink et al., 2009; Zijlema, 2012; Bakker de et al., 2014, 2015; Dusseljee et al., 2014; Rijnsdorp et al., 2014, 2015; Fiedler et al., 2019; Zhang et al., 2020; Li et al., 2020; Henderson et al., 2022). The effect of free shoreward propagating IG waves in the model offshore boundary has not received much attention. To our knowledge, no parameterization or boundary condition exists that includes both bound and free IG waves.

In this chapter, I analyze the relative contribution of bound and free IG energy to the total IG energy in $10-15$m water depth for beaches in San Diego County, USA, confirm theoretical estimates of the incident bound wave energy, investigate parameterizations for both bound and free IG energy and estimate an IG sea surface elevation timeseries that can be used as an incident boundary condition for nearshore models. Section 4.3.1 describes the dataset and quality control. Section 4.3.2 confirms that directional bound wave theory (Hasselmann, 1962) accurately predicts the observed bound wave energy. In Section 4.3.2 and 4.3.3, the relative contributions of shoreward propagating bound and free IG waves and their respective dependencies on the SS wave field is presented and compared with previous observations from other sites. The total incident bound and free IG energy and the spectral shape of the free energy are discussed in Section 4.4.

## 4.3 Observations

### 4.3.1 Data

Bottom-mounted pressure sensors and current meters (PUV) were deployed in 10 and 15m depths at Torrey Pines State Beach and Cardiff State Beach, CA intermittently between Fall 2019 and Spring 2022 (Figure 4.3.1 and Table 4.3.1). Data were collected continuously between Fall 2021 and Spring 2022 as part of the Runup and Bathymetry 2D (RuBy2D) experiment at Torrey Pines, a 3km long, alongshore-uniform composite (summer sand, winter cobbles) beach. Cardiff is a 1.8km alongshore-variable beach, with a rocky reef

beginning approximately 125m offshore at the southern end (Ludka et al., 2019). The 2Hz PUV data were segmented into 3h records. The three largest tidal constituents are removed from the bottom pressure and velocity records, and the records are surface-corrected using linear finite-depth theory over the frequency band $0.004 - 0.25$Hz. Computed spectra are segmented in 7200s demeaned ensembles, with an applied 50% overlapping Hanning window, with 0.0003Hz frequency resolution and 13 degrees of freedom. The IG band is defined between $0.004 - 0.04$Hz, the swell band between $0.04 - 0.12$Hz and the sea band between $0.12 - 0.25$Hz. As quality control, 3-hour pressure and velocity spectra passed a Z-test (Eq. 1 in Elgar et al., 2005),

$$Z^2 = \frac{P^2}{\left(\frac{\omega}{gk}\right)^2 \frac{\cosh^2 kh_P}{\cosh^2 kh_U}(U^2 + V^2)}, \tag{4.5}$$

with cutoffs of $0.8 < Z_{IG} < 1.2$ and $0.95 < Z_{SS} < 1.05$. This confirms the use of linear theory in the sea surface correction. Additionally, only records with reflection coefficients (Eq. 4 in Sheremet et al., 2002) of $R^2_{SS} < 0.25$ and $R^2_{IG} < 2.5$ are used further. The resulting 2844 quality controlled 3h record instrument information and SS bulk wave statistics are given in Table 4.3.1, including MOP location (580s are Torrey Pines and 669 is Cardiff in O'Reilly et al. (2016) and Ludka et al. (2019)), date range, depth and the number of resulting records from a given PUV, and significant wave height $Hs_{SS}$, peak period $T_p$, peak direction $D_p$ and spread $D_{spread}$. Spectral wave model (MOPS, O'Reilly et al., 2016) hindcast data from the observation periods show similar distributions of bulk parameters as a 23-year hindcast (Figure 4.3.2, $\langle\sqrt{H_0 L_0}\rangle = 14.5 \pm 4.6$m, $\langle\sqrt{H_0 L_0}\rangle_{obs} = 15.5 \pm 4.6$m, $\langle H_0\rangle = 0.83 \pm 0.38$m, $\langle H_0\rangle_{obs} = 0.85 \pm 0.39$m, $\langle f_{spread}\rangle = 0.033 \pm 0.007$Hz, $\langle f_{spread}\rangle_{obs} = 0.032 \pm 0.007$Hz, $\langle f_{peak}\rangle = 0.083 \pm 0.03$Hz, $\langle f_{peak}\rangle_{obs} = 0.077 \pm 0.026$Hz). The current observations are therefore indicative of the San Diego wave climate. Sea-surface elevation and velocity are combined to estimate shoreward and seaward propagating wave components (Sheremet et al., 2002). Unless explicitly stated, the shoreward sea-surface

elevation timeseries is used below.

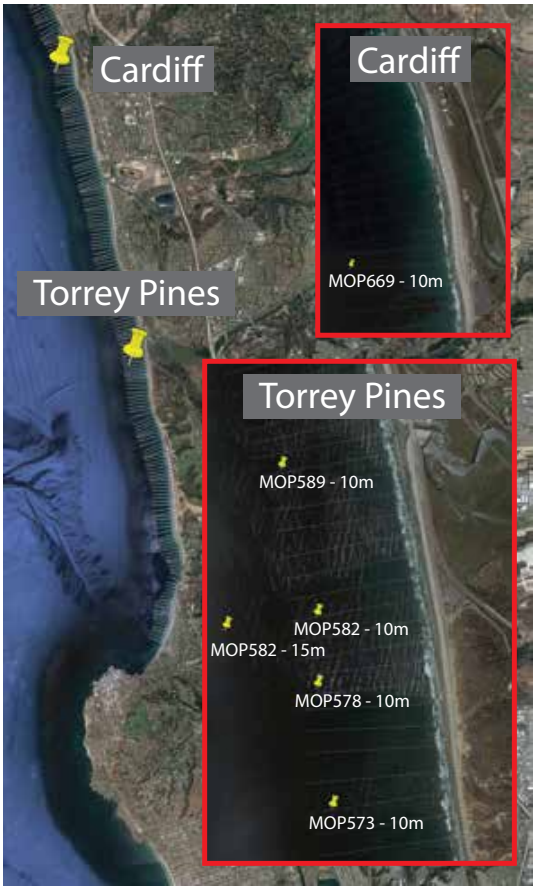


**Figure 4.3.1.** Map of PUV (co-located pressure and biaxial acoustic current meter) locations in San Diego County.

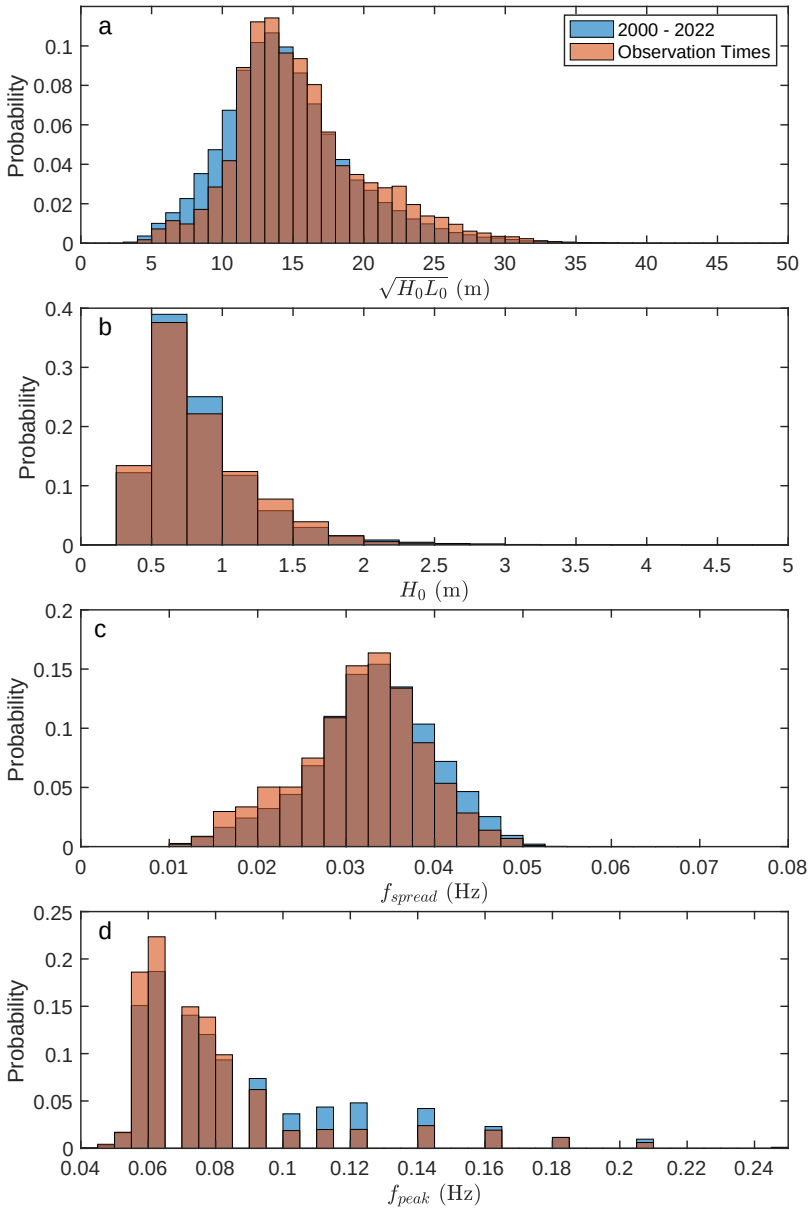


**Figure 4.3.2.** Histograms of (a) $\sqrt{H_0 L_0}$, (b) $H_0$, (c) $f_{spread}$, and (d) $f_{peak}$ at Torrey Pines in 10m at MOP582. Histograms are similar for 2000 - 2022 hindcast (blue, 201,600 1h values) and present observations (orange, 12,602 1h records). All hindcasts computed from MOPS data.

**Table 4.3.1.** PUV Bulk Statistics

| MOP | Date | Depth (m) | Distance from backbeach (m) | # of records | $Hs_{SS}$ (m) | $T_p$ (s) | $D_p$ (degrees) | $D_{spread}$ (degrees) |
|---|---|---|---|---|---|---|---|---|
| 582 | 11/19 - 04/20 | 10 | 580 | 316 | 0.3 - 2.4 | 5 - 21 | 0 - 23 | 7 - 21 |
| 582 | 10/20 - 03/21 | 10 | 580 | 315 | 0.3 - 4.1 | 5 - 21 | 0 - 25 | 9 - 22 |
| 582 | 07/21 - 09/21 | 10 | 580 | 223 | 0.4 - 1 | 5 - 19 | 0 - 29 | 14 - 24 |
| 669 | 07/21 - 09/21 | 10 | 600 | 285 | 0.4 - 1.1 | 5 - 20 | 1 - 32 | 6 - 25 |
| 573 | 10/21 - 03/22 | 10 | 600 | 281 | 0.4 - 2.5 | 5 - 19 | 0 - 28 | 8 - 22 |
| 578 | 10/21 - 11/21 | 10 | 630 | 55 | 0.4 - 1.7 | 9 - 20 | 1 - 10 | 10 - 22 |
| 582 | 10/21 - 02/22 | 10 | 630 | 323 | 0.3 - 2.3 | 5 - 20 | 0 - 19 | 9 - 21 |
| 582 | 10/21 - 02/22 | 15 | 1020 | 401 | 0.5 - 2.7 | 5 - 20 | 0 - 25 | 8 - 25 |
| 589 | 10/21 - 02/22 | 10 | 660 | 289 | 0.3 - 2.3 | 6 - 20 | 0 - 32 | 9 - 22 |

### 4.3.2 Bound Waves

Examples of the 1D and 2D ($\pm 90°$ from shorenormal directionally-integrated) bound wave energy predicted by Hasselmann (1962) and bispectral estimates for different SS conditions are shown in Figure 4.3.3. Consistent with the effects of co-linearity on the interaction coefficient $D$ in Eq. 4.1, the 1D estimates are on average 3x larger than the (directionally-integrated) 2D estimates.

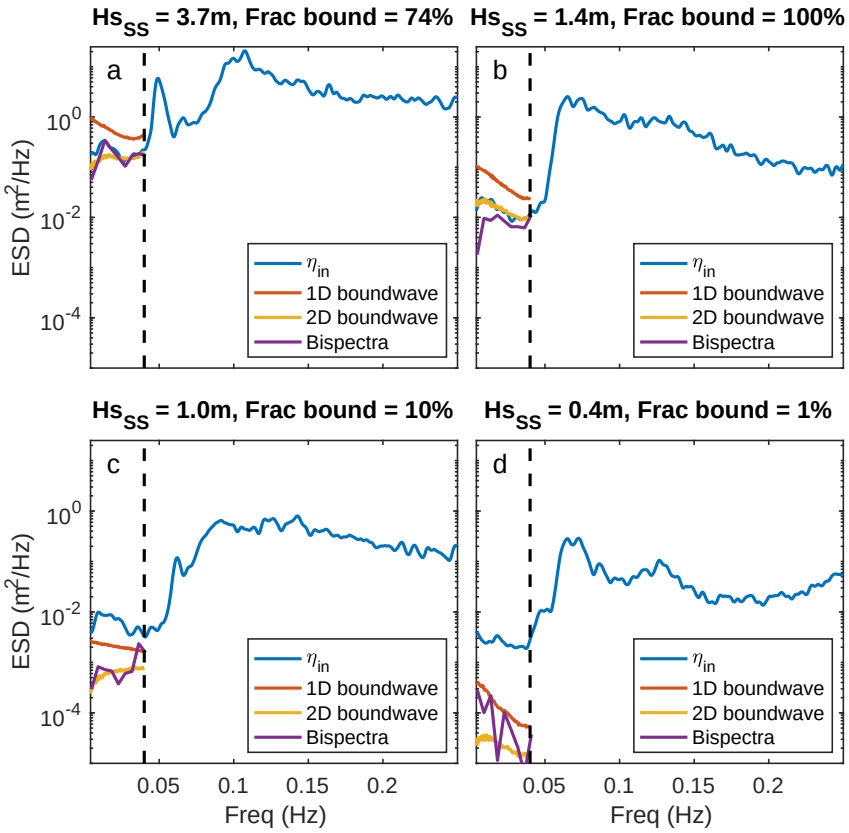


**Figure 4.3.3.** Observed (blue) sea surface elevation frequency spectra $\mathbf{E}(f)$ in 10m for varying sea-swell wave heights $Hs$ (a) $Hs = 3.7$m, $D_{spread,SS} = 18°$ (b) $Hs = 1.4$m, $D_{spread,SS} = 13°$, (c) $Hs = 1.0$m, $D_{spread,SS} = 17°$, and (d) $Hs = 0.4$m, spread $D_{spread,SS} = 24°$. In the IG band ($f < 0.04$Hz, dashed vertical line), theoretical results are shown for 1D bound wave and 2 D bound wave, and for a bispectral approach (Herbers, Guza, 1994). Fraction bound (based on 2D bound waves) ranges from about 100% (a, largest $Hs$) to 1% (d, smallest $Hs$).

Bispectral analysis confirms Hasselmann (1962)'s 2D nonlinear theory provides reasonable estimates of the bound wave energy (Figure 4.3.4). However, the bispectral $E_{IG}^{forced}$ estimate can be inaccurate when nonlinear coupling is weak, bound wave energy is low and free waves dominate. At individual frequencies, the bispectral and the bound wave estimates can differ by as much as a factor of 50 (Figure 4.3.3 and Herbers, Guza (1994)). Integrated over IG frequencies, the 2D bound wave and the forced wave energy (for fraction bound $> 15\%$) agree well (slope = 0.93) with a correlation of $R^2 = 0.94$ (Figure 4.3.4). The cases of fraction bound $> 15\%$ are typically larger SS events (median $\sqrt{H_0 L_0} = 13.1$m compared to the median of the dataset = 10.7m).

Further analysis uses 2D bound wave theory because (unlike the bispectral estimates) it does not rely on insitu IG observations and can be estimated from buoy or spectral wave model data. The frequency dependence of the bound wave coupling coefficient is seen with $E_{IG}^{bound}$ being more highly correlated with $E_{swell}$ ($R^2 = 0.84$) than $E_{sea}$ ($R^2 = 0.59$).

The bound wave fraction of the current dataset is typically $\sim 8\%$ for the most prevalent moderate wave conditions ($Hs_{SS} \sim 0.7$m), with only 5% of the cases (120/2488) having a fraction bound greater than 50% (Figure 4.3.5 d). Across all previous observations, the fraction bound increases with increasing $E_{IG}$ and $E_{SS}$ and decreasing depth (or tides), where the sensor is most likely closer to the surfzone, and therefore more bound wave generation has occurred. In our results, the total bound wave energy scales similarly (Figure 4.3.5 a). This can be traced back to the shallow water limit of Eq 4.1, with $E_{IG}^{bound} \sim E_{SS}^2 h^{-5}$ (Herbers et al., 1995a).

### 4.3.3 Free Waves

The shoreward free IG energy spectra is estimated by subtracting the bound wave estimate ($\mathbf{E}_{IG}^{bound}(f)$) from the total incident wave energy spectra. These shoreward-directed free waves are a combination of refractively trapped (and typically locally generated) waves and leaky waves from remote sources. The free (and due to the dominance of free wave IG

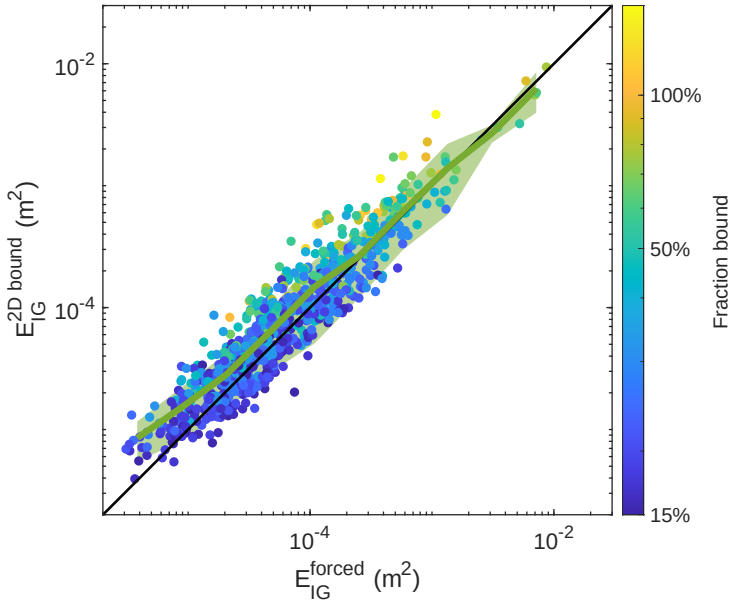


**Figure 4.3.4.** Bound IG energy from nonlinear 2D theory (Hasselmann, 1962) versus an estimate $E_{IG}^{forced}$ based on bispectral analysis (Herbers, Guza, 1994). Colors are fraction bound based on 2D bound wave theory. When fraction bound $< 15\%$ bispectral results are widely scattered, and not shown or included in $R^2$. The 1-1 line, and mean and standard deviation for binned data (green curve and shading) are shown.

energy, the total) wave energy is approximately linearly proportional to $E_{SS}$ (Figure 4.3.5 b, c, and consistent with Herbers et al., 1995b; Okihiro, Guza, 1995). This linear dependence on $E_{SS}$, as opposed to a quadratic dependence for the bound wave, has been attributed to dissipation (Herbers et al., 1995b). Free waves have a weaker depth dependence ($h^{-1}$) than bound waves ($h^{-5}$), consistent with Herbers et al. (1995b).

Okihiro et al. (1992) found that in Southern California for typical SS energy, 25% of the IG energy was bound in 8-13m depth, 70% was trapped shoreward of a sensor in 183m depth, and only 5% was leaky. Leaky, free IG waves can propagate across ocean basins and in deep water appear uncoupled from and uncorrelated with local SS wave conditions (Webb et al., 1991; Ardhuin et al., 2014). However, on the inner shelf, remotely generated

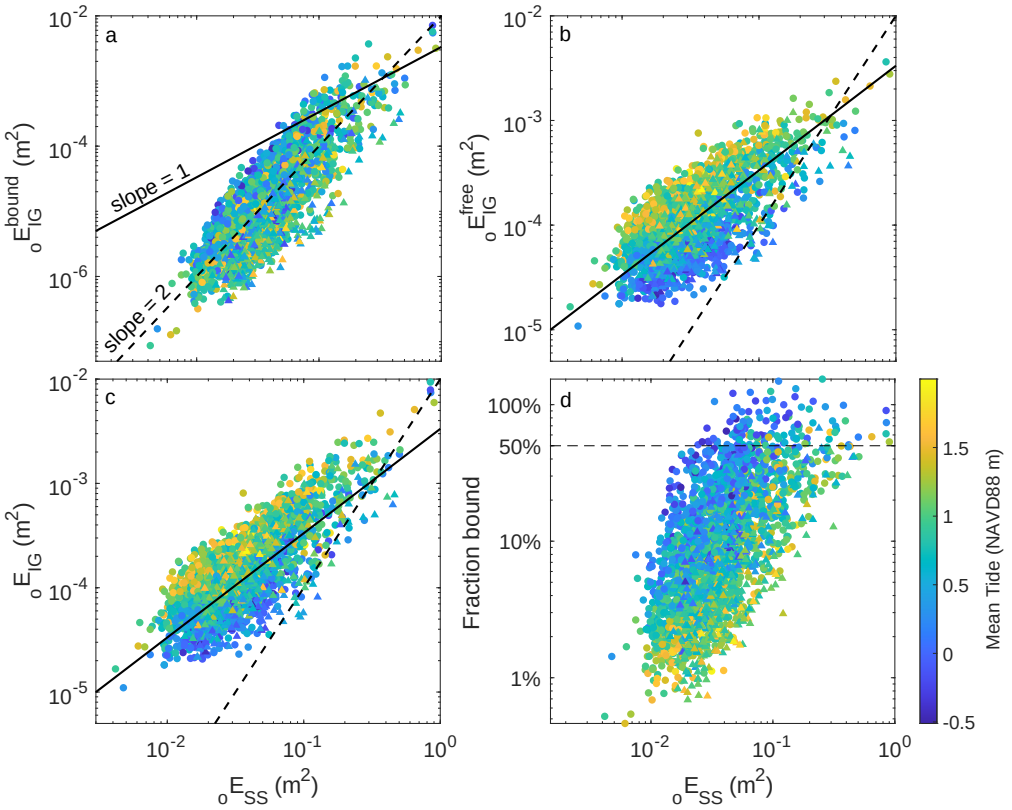


**Figure 4.3.5.** Observed shoreward propagating IG energy (a)$E_{IG}^{bound}$, (b) $E_{IG}^{free}$, (c) $E_{IG}^{total}$, and (d) fraction bound versus $E_{SS}$. $\triangle$ is 15m PUV data. $E_{IG}^{bound}$ scales as $E_{SS}^2$ whereas both total and free IG energy scale as $E_{SS}$ (solid and dashed lines, respectively). Most observed fraction bound are $< 50\%$ and many are $< 10\%$.

IG waves only dominate local IG waves when $E_{SS}$ is very low (Herbers et al., 1995b; Sheremet et al., 2002). Remotely generated IG waves (i.e., unrelated to local SS wave energy) are not considered in the following analysis and contribute to parameterization noise.

## 4.4 Parameterizing the IG wave field

### 4.4.1 Bound Waves

Although 2D bound wave energy can be determined from the incident sea-swell spectrum and theory, it can be useful for computational efficiency to parameterize the total bound wave energy from bulk sea-swell wave statistics. A linear regression between ${}_{pred}E_{IG}^{bound}$ and $E_{SS}^2 h^{-5}$ (with exponents predicted in Herbers et al. (1995a) and similar to Ruessink (1998)), performs reasonably well, with correlation coefficients $R^2$ between $0.58 - 0.91$, for 10m Torrey Pines, 15m Torrey Pines and 10m Cardiff PUVs. A frequency-weighted sea-swell energy integral $\left(\int_{SS} \mathbf{E}(f) f^{-1} df\right)$ (similar to the approach of Fiedler et al. (2020)), results in higher correlations across all PUV sensors (Eq. 4.6 with $R^2 = 0.84 - 0.97$, Figure 4.4.1 a),

$$ {}_{p}E_{IG}^{bound} = 15.2 \left( \int_{SS} \mathbf{E}(f) f^{-1} df \right)^2 h^{-5}. \tag{4.6} $$

The parametric form includes the important dependencies of depth, frequencies, and SS wave energy.

### 4.4.2 Shoreward Free Waves

Figure 4.3.5 b shows a relationship between ${}_{obs}E_{IG}^{free}$ and $E_{SS}$, which performs reasonably well (linear regression gives a correlation of $R^2 = 0.79$). However, similar to the bound wave parameterization, a frequency-weighted SS energy integral improves the linear regression fit to $R^2 = 0.84$. The known tidal dependence of the free IG energy is accounted for with the normalized tide ($\tilde{\sigma} = \frac{\text{tide}_{obs} - \text{tide}_{low}}{\text{tide}_{high} - \text{tide}_{low}}$, where 2.5m is the total tidal range observed across all deployments), with $\tilde{\sigma} = 0$ at the lowest observed tide ($-0.5$ NAVD88m), and $\tilde{\sigma} = 1$ at the highest tide (2 NAVD88m). Including a linear $\tilde{\sigma}$ dependence in the regression improves the correlation between observed and predicted total $E_{IG}^{free}$

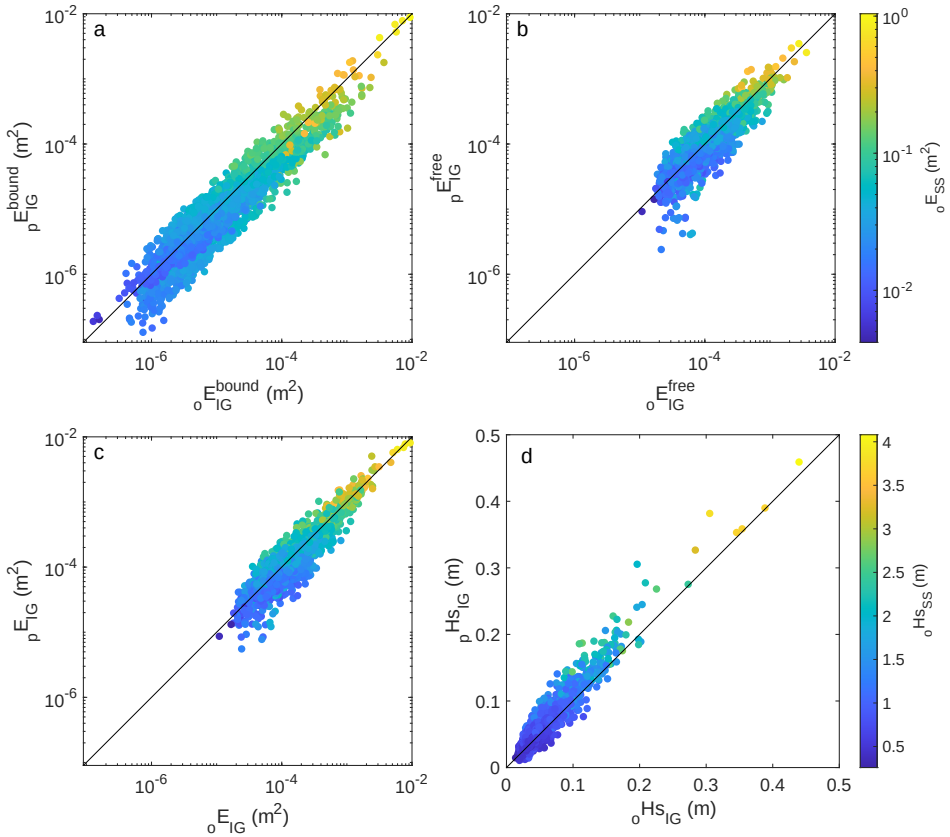


**Figure 4.4.1.** Parameterizations of incident IG wave field. (a) 2D bound wave parameterization (Eq. 4.6, $R^2 = 0.95$), (b) Free wave parameterization (Eq. 4.7, $R^2 = 0.9$), (c) 2D bound wave theory + free wave parameterization ($R^2 = 0.97$), colored by total incident SS energy (see color bar in (b)) and (d) significant wave height of estimated IG timeseries ($R^2 = 0.95$), colored by SS significant wave height.

energy to $R^2 = 0.9$ (Eq. 4.7, Figure 4.4.1 b) at all but the lowest tides and $E_{SS}$,

$$_pE_{IG}^{free} = 0.00067\tilde{\sigma} \int_{SS} \mathbf{E}(f) f^{-1} df. \tag{4.7}$$

Correlations in different depths and beaches are in Table 4.4.1.

The total shoreward IG energy, with contributions from both bound and free waves

**Table 4.4.1.** $R^2$ between total (frequency-band integrated) free shoreward IG energy observed and three parameterizations using the observed sea-swell wave energy spectrum $\mathbf{E}_{SS}(f)$. PUV sensors were deployed in 10m and 15m at Torrey Pines and 10m at Cardiff (see Table 4.3.1 for details). In all cases, $\tilde{\sigma}\int_{SS}\mathbf{E}(f)f^{-1}df$ has the highest $R^2$.

| | $\int_{SS}\mathbf{E}(f)df$ | $\int_{SS}\mathbf{E}(f)f^{-1}df$ | $\tilde{\sigma}\int_{SS}\mathbf{E}(f)f^{-1}df$ |
|---|---|---|---|
| 10m Torrey Pines | 0.82 | 0.88 | 0.92 |
| 15m Torrey Pines | 0.63 | 0.74 | 0.84 |
| 10m Cardiff | 0.5 | 0.69 | 0.87 |
| Total | 0.79 | 0.84 | 0.9 |

can be estimated with local SS parameters. The parmeterization performs well ($R^2 = 0.96$) for all but the smallest $E_{SS}$ and tides using either the bound wave parameterization (Eq. 4.6) or the integrated 2D Hasselmann bound wave energy (Figure 4.4.1 c). On the smallest $E_{SS}$ conditions, the parameterization underpredicts $E_{IG}$. This may be due to very little local IG wave generation and fractionally higher contributions to the IG wave field from free waves from remote sources (Webb et al., 1991; Ardhuin et al., 2014), but without other observations, this is not possible to determine.

Functional forms of the frequency distribution of the free IG energy were compared with the observed free IG spectra (normalized by the frequency-weighted SS energy). Functional forms investigated include linear and cubic fits to the median spectral shape, the spectral shape of Ardhuin et al. (2014) and an altered form (referred to as *nouvelleArdhuin*, Eq. 4.8),

$$A(f) = \begin{cases} \beta\frac{1}{\Delta f} * [f/0.012\text{Hz}] & \text{when } f < 0.012\text{Hz} \\ \beta\frac{1}{\Delta f} * [0.012\text{Hz}/f] & \text{when } f > 0.012\text{Hz} \end{cases}, \tag{4.8}$$

with $\beta = 0.0146$.

NouvelleArdhuin has the smallest ($\sim 0.35$) median root-mean-square logarithmic error (RMSLE) between ${}_{obs}E_{IG}^{free} * A(f)$ and ${}_{obs}\mathbf{E}_{IG}^{free}(f)$. Over all 2488 records, RMSLE are linear $\sim 0.45$, cubic $\sim 0.4$ and Ardhuin $\sim 0.42$. The free wave frequency distribution varies over a wide range and leads to relatively large RMSLE errors in all the tested forms.

NouvelleArdhuin (Eq. 4.8) is relatively simple, has the smallest errors, and is used below.

Timeseries realizations of the shoreward free IG are estimated from an inverse FFT of ${}_{pred}\mathbf{E}_{IG}^{free}(f)$,

$$\begin{aligned} {}_{p}\mathbf{E}_{IG}^{free}(f) =& {}_{p}E_{IG}^{free} * A(f), \\ & \text{with } {}_{p}E_{IG}^{free} = 0.00067\tilde{\sigma} \int_{SS} \mathbf{E}(f) f^{-1} df, \end{aligned} \tag{4.9}$$

with random phases and $A(f)$ (Eq. 4.8).

Linearly combining the computed bound wave timeseries with the estimated shoreward propagating free wave timeseries (with random phase), yields an estimated total shoreward IG timeseries that can be used as a boundary condition for numerical models. The parameterizations approximately reproduce a range of infragravity heights (Figure 4.4.1 c, RMSE $\sim$ 0.01m, Skill = 0.82, $R^2 = 0.95$, Bias = 0.006m).

## 4.5 Discussion

Ardhuin et al. (2014) parameterized seaward free IG energy as a function of local sea-swell conditions, and used that parameterization as a shoreline boundary condition in a global ocean wave model. The underlying assumption is that seaward IG energy is free, directionally broad, and mainly radiated from the surfzone. The ${}_{p}\mathbf{E}_{IG}^{sea}(f)$ parameterization is

$${}_{p}\mathbf{E}_{IG}^{sea}(f) = \left[1.2\alpha^2 \frac{kg^2}{c_g 2} \left(\frac{H_s T_{m,0}^2}{4}\right)^2\right] * \frac{1}{\Delta f} \left[\min\left(1, \frac{0.015\text{Hz}}{f}\right)\right]^{1.5}, \tag{4.10}$$

with the first part determining the frequency-band integrated ${}_{p}E_{IG}^{sea}$ energy, and the second, the frequency distribution of the seaward IG spectrum. Zheng et al. (2021) compared output from the Ardhuin et al. (2014) model and observations of $H_{IG}$ and found $R^2 = 0.6$. Using this approach for seaward IG energy yields similar parameters for $\alpha$ (= 8.3 x $10^{-4} s^{-1}$) with $R^2 = 0.71$ between estimated and observed $E_{IG}^{free}$ (Figure 4.5.1 a). A parameterization,

similar to Eq. 4.7, for the seaward energy,

$$ {}_pE_{IG}^{seaward} = 0.001\tilde{\sigma} \int_{SS} \mathbf{E}(f) f^{-1} df. \tag{4.11} $$

shows similar tidal dependence of seaward and shoreward energy, and similar high skill $R^2 = 0.91$ (Figure 4.5.1 b). The ratio of seaward/shoreward = 0.001/0.00067 = 1.5, is constant and independent of tide. Although the dependence on $\tilde{\sigma}$ and the constant are not well constrained, the implication that $R^2_{IG}$ is not a function of tide level is supported by the observations (Figure 4.5.2, $R^2 = 0.22$).

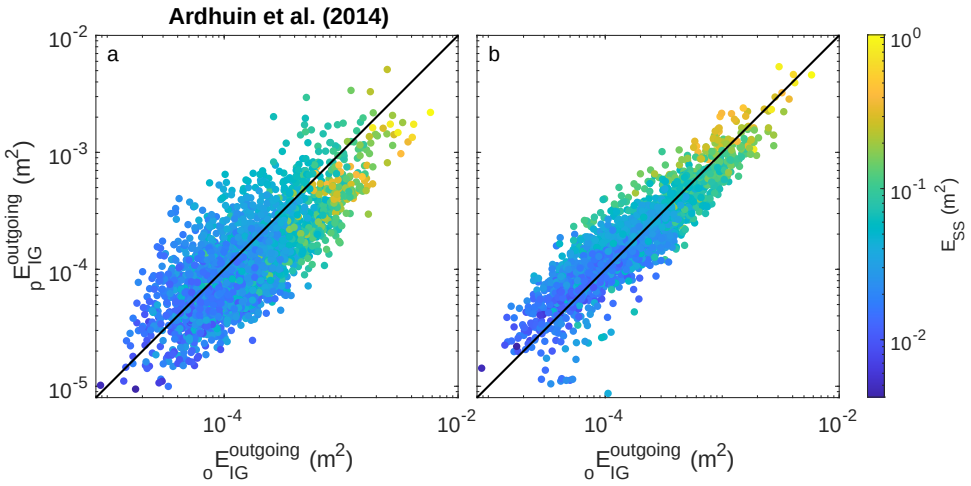


**Figure 4.5.1.** Parameterization of seaward IG energy from local SS conditions. (left) Ardhuin et al. (2014) ($R^2 = 0.71$) and (right) new parameterization ($R^2 = 0.91$), including tidal dependence (Eq. 4.11).

A tidal modulation of the total and free IG energy is observed (Figure 4.3.5 b, c), consistent with previous observations of total IG energy in Southern California (Okihiro, Guza, 1995). This modulation, lower $E_{IG}$ at low tide, has been attributed to IG energy loss within the surfzone being stronger on flat and shallow low-tide beaches than on steeper high-tide beaches (given a concave beach profile, Figure 4.5.2) (Thomson et al., 2006).

Note that refractive trapping of seaward IG energy creates shoreward IG waves. That is, seaward and shoreward IG waves both increase at high tide, when the surfzone more efficiently radiates IG energy.

Observed values of $R^2_{IG}$ vary between 0.5 - 2.5, whereas $R^2_{IG} = 1.5$ follows from the present crude parameterizations. While $R^2_{IG}$ at the shoreline is constrained to $< 1$, $R^2_{IG} > 1$ in 10-15m depth allows for onshore IG surf zone generation and dissipation, shoreline reflection and trapping (Gallagher, 1971; Elgar, Guza, 1985; Oltman-Shay, Guza, 1987; Okihiro et al., 1992; Elgar et al., 1992, 1994; Herbers, Guza, 1994; Herbers et al., 1995a,b; Okihiro, Guza, 1995; Sheremet et al., 2002; Battjes, 2004; Thomson et al., 2006; Henderson et al., 2006; Rijnsdorp et al., 2015). Ongoing numerical simulations with the SWASH model are intended to understand IG wave physics, including at beaches with much lower and higher slopes (and different wave climates) than parameterized here.

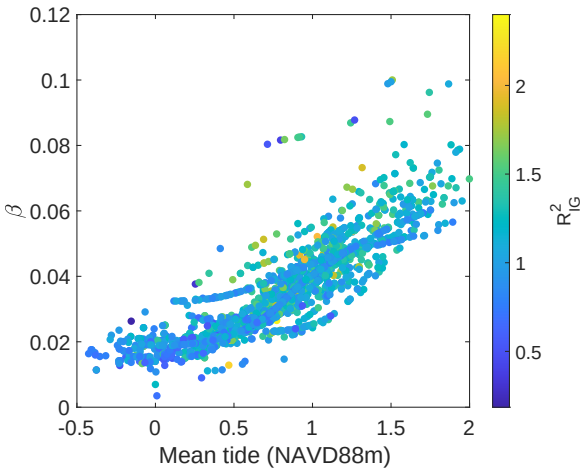


**Figure 4.5.2.** Beach slope versus mean tide (relative to NAVD88m) of 3h record) at Torrey Pines. Beach slope is the linear fit ±0.5m around the tide level. The concave shape of subaerial beach results in a steeper beach face at high tide than low tide. However, $R^2_{IG}$ is not significantly correlated with on beach slope or tide level.

## 4.6 Conclusion

This relative contribution of bound and free infragravity waves to the IG wave field on the inner shelf (depth 10-15m) in San Diego County, USA was examined using PUV observations and nonlinear wave theory. In general, free waves dominate the IG wave field with only 5% of the records showing a bound wave fraction $> 50\%$. This is consistent with previous observations in Southern California and Duck, USA and the North Sea. The bound wave energy scaled with the local SS energy squared (with higher correlation to swell energy than sea) and has a slight depth dependence consistent with a $h^{-5}$ scaling. The free IG energy was found to scale linearly with the local SS energy and the mean tide. These dependencies were exploited to derive parameterizations for the total (bound and free IG) shoreward propagating energy as a function of tide and local sea-swell conditions that can be determined from spectral refraction models or buoy observations. A parameterization of the seaward propagating IG waves also showed a tidal dependence that differed from previous seaward-going IG energy (Ardhuin et al., 2014). Using an observation-based frequency distribution for free IG energy, bound and free wave can be included in synthetic IG timeseries that can be used to initialize models for surfzone processes including runup.

## 4.7 Acknowledgments

This study was funded by the U.S. Army Corps of Engineers (W912HZ1920020) and the California Department of Parks and Recreation (C19E0026). Data were collected and processed by the Coastal Processes Group field team members Lucian Parry, Rob Grenzeback, Kent Smith, Brian Woodward, Greg Boyd, Shane Finnerty, Carson Black, and Mele Johnson. Michele Okihiro organized logistics.

Chapter 4, in part, is currently being prepared for submission for publication of the material. A.M.Z. Lange, J.W. Fiedler, M.A. Merrifield, and R.T. Guza. The dissertation

author was the primary investigator and author of this material.

# Bibliography

*Aagaard Troels, Greenwood Brian.* Suspended sediment transport and the role of infragravity waves in a barred surf zone // Marine Geology. IV 1994. 118, 1-2. 23–48.

*Aagaard Troels, Greenwood Brian.* Infragravity wave contribution to surf zone sediment transport — The role of advection // Marine Geology. V 2008. 251, 1-2. 1–14.

*Aarninkhof S. G. J.* Nearshore subtidal bathymetry from time-exposure video images // Journal of Geophysical Research. 2005. 110, C6. C06011.

*Abileah Ron, Trizna Dennis B.* Shallow water bathymetry with an incoherent X-band radar using small (smaller) space-time image cubes // 2010 IEEE International Geoscience and Remote Sensing Symposium. Honolulu, HI, USA: IEEE, VII 2010. 4330–4333.

*Alevizos Evangelos.* A Combined Machine Learning and Residual Analysis Approach for Improved Retrieval of Shallow Bathymetry from Hyperspectral Imagery and Sparse Ground Truth Data // Remote Sensing. X 2020. 12, 21. 3489.

*Almar Rafael, Bonneton Philippe, Senechal Nadia, Roelvink Dano.* WAVE CELERITY FROM VIDEO IMAGING: A NEW METHOD // Coastal Engineering 2008. Hamburg, Germany: World Scientific Publishing Company, V 2009. 661–673.

*Almeida Luis Pedro, Masselink Gerd, McCall Robert, Russell Paul.* Storm overwash of a gravel barrier: Field measurements and XBeach-G modelling // Coastal Engineering. II 2017. 120. 22–35.

*Altomare Corrado, Bolle A, Brand E, Chen M, Dan S, De Sloover L, Dewulf A, Ramos J, Gruwez V, Houthuys R, Kisacik D, Lonneville B, Mertens T, Monbaliu J, Montreuil A, Ouda M, Ponsar S, Rauwoens P, Roest B, Toorman E, Strypsteen G, Suzuki T, Troch P, Trouw K, Van Ackere S, Vandebeek I, Eynde D Van den, Verwaest Toon, Wongsoredjo S, Zhange Q.* CREST Final Scientific Report: Take Home Messages & Project Results. 2020.

*Ardhuin Fabrice, Devaux Emmanuel, Pineau-Guillou Lucia.* Observation et prévision des seiches sur la côte Atlantique française // XIèmes Journées, Les Sables d'Olonne. 2010.

1–8.

*Ardhuin Fabrice, Rawat Arshad, Aucan Jerome.* A numerical model for free infragravity waves: Definition and validation at regional and global scales // Ocean Modelling. V 2014. 77. 20–32.

*Atkinson Alexander L., Power Hannah E., Moura Theo, Hammond Tim, Callaghan David P., Baldock Tom E.* Assessment of runup predictions by empirical models on non-truncated beaches on the south-east Australian coast // Coastal Engineering. I 2017. 119. 15–31.

*Aubrey David G.* Seasonal patterns of onshore/offshore sediment movement // Journal of Geophysical Research. 1979. 84, C10. 6347.

*Bak A. Spicer, Brodie Katherine L., Hesser Tyler J., Smith Jane M.* Applying dynamically updated nearshore bathymetry estimates to operational nearshore wave modeling // Coastal Engineering. III 2019. 145. 53–64.

*Bakker A. T. M. de, Herbers T. H. C., Smit P. B., Tissier M. F. S., Ruessink B. G.* Nonlinear Infragravity–Wave Interactions on a Gently Sloping Laboratory Beach // Journal of Physical Oceanography. II 2015. 45, 2. 589–605.

*Bakker A.T.M. de, Tissier M.F.S., Ruessink B.G.* Shoreline dissipation of infragravity waves // Continental Shelf Research. I 2014. 72. 73–82.

*Baldock T.E., Manoonvoravong P., Pham Kim Son.* Sediment transport and beach morphodynamics induced by free long waves, bound long waves and wave groups // Coastal Engineering. X 2010. 57, 10. 898–916.

*Basco David R.* A Qualitative Description of Wave Breaking // Journal of Waterway, Port, Coastal, and Ocean Engineering. 1985. 111, 2. 171–188.

*Battjes J. A.* Surf Similarity // Coastal Engineering. 1974.

*Battjes J A.* Surf-Zone Dynamics // Annual Review of Fluid Mechanics. 1988. 20. 257–293.

*Battjes J. A.* Shoaling of subharmonic gravity waves // Journal of Geophysical Research. 2004. 109, C2. C02009.

*Becker J. M., Merrifield M. A., Yoon H.* Infragravity waves on fringing reefs in the tropical Pacific: Dynamic setup // Journal of Geophysical Research: Oceans. V 2016. 121, 5. 3010–3028.

*Beer A.F. de, McCall R.T., Long J.W., Tissier M.F.S., Reniers A.J.H.M.* Simulating wave

runup on an intermediate–reflective beach using a wave-resolving and a wave-averaged version of XBeach // Coastal Engineering. I 2021. 163. 103788.

*Behrens James, Thomas Julie, Terrill Eric, Jensen Robert.* CDIP: Maintaining a Robust and Reliable Ocean Observing Buoy Network // 2019 IEEE/OES Twelfth Current, Waves and Turbulence Measurement (CWTM). San Diego, CA, USA: IEEE, III 2019. 1–5.

*Bender Christopher J., Dean Robert G.* Wave field modification by bathymetric anomalies and resulting shoreline changes: a review with recent results // Coastal Engineering. VIII 2003. 49, 1-2. 125–153.

*Benshila Rachid, Thoumyre Grégoire, Najar Mahmoud Al, Abessolo Grégoire, Almar Rafael, Bergsma Erwin, Hugonnard Guillaume, Labracherie Laurent, Lavie Benjamin, Ragonneau Tom, Simon Ehouarn, Vieuble Bastien, Wilson Dennis.* A Deep Learning Approach for Estimation of the Nearshore Bathymetry // Journal of Coastal Research. V 2020. 95, sp1. 1011.

*Bergsma E.W.J., Conley D.C., Davidson M.A., O'Hare T.J.* Video-based nearshore bathymetry estimation in macro-tidal environments // Marine Geology. IV 2016. 374. 31–41.

*Bergsma Erwin W.J., Almar Rafael, Almeida Luis Pedro Melo de, Sall Moussa.* On the operational use of UAVs for video-derived bathymetry // Coastal Engineering. X 2019. 152. 103527.

*Bertin Xavier, Bakker Anouk de, Dongeren Ap van, Coco Giovanni, André Gael, Ardhuin Fabrice, Bonneton Philippe, Bouchette Frédéric, Castelle Bruno, Crawford Wayne C., Davidson Mark, Deen Martha, Dodet Guillaume, Guérin Thomas, Inch Kris, Leckler Fabien, McCall Robert, Muller Héloïse, Olabarrieta Maitane, Roelvink Dano, Ruessink Gerben, Sous Damien, Stutzmann Éléonore, Tissier Marion.* Infragravity waves: From driving mechanisms to impacts // Earth-Science Reviews. II 2018. 177. 774–799.

*Brodie Katherine L., Bruder Brittany L., Slocum Richard K., Spore Nicholas J.* Simultaneous Mapping of Coastal Topography and Bathymetry From a Lightweight Multicamera UAS // IEEE Transactions on Geoscience and Remote Sensing. IX 2019. 57, 9. 6844–6864.

*Brodie Katherine L., Palmsten Margaret L., Hesser Tyler J., Dickhudt Patrick J., Raubenheimer Britt, Ladner Hannah, Elgar Steve.* Evaluation of video-based linear depth inversion performance and applications using altimeters and hydrographic surveys in a wide range of environmental conditions // Coastal Engineering. VI 2018. 136. 147–160.

*Bruder Brittany L., Brodie Katherine L.* CIRN Quantitative Coastal Imaging Toolbox //

SoftwareX. VII 2020. 12. 100582.

*Catálan Patricio A., Haller Merrick C.* Remote sensing of breaking wave phase speeds with application to non-linear depth inversions // Coastal Engineering. I 2008. 55, 1. 93–111.

*Cohn N., Ruggiero P., Ortiz J., Walstra D.J.* Investigating the role of complex sandbar morphology on nearshore hydrodynamics // Journal of Coastal Research. IV 2014. 70. 53–58.

*Collins Adam, Brodie Katherine, Bak Andrew Spicer, Hesser Tyler, Farthing Matthew, Lee Jonghyun, Long Joseph.* Bathymetric Inversion and Uncertainty Estimation from Synthetic Surf-Zone Imagery with Machine Learning // Remote Sensing. X 2020. 12, 20. 3364.

*Cox Nicholas, Dunkin Lauren M., Irish Jennifer L.* An empirical model for infragravity swash on barred beaches // Coastal Engineering. XI 2013. 81. 44–50.

*De Bakker A. T. M., Brinkkemper J. A., Van Der Steen F., Tissier M. F. S., Ruessink B. G.* Cross-shore sand transport by infragravity waves as a function of beach steepness: SAND TRANSPORT BY INFRAGRAVITY WAVES // Journal of Geophysical Research: Earth Surface. X 2016. 121, 10. 1786–1799.

*Dodet Guillaume, Melet Angélique, Ardhuin Fabrice, Bertin Xavier, Idier Déborah, Almar Rafael.* The Contribution of Wind-Generated Waves to Coastal Sea-Level Changes // Surveys in Geophysics. XI 2019. 40, 6. 1563–1601.

*Dongeren A. van, Battjes J., Janssen T., Noorloos J. van, Steenhauer K., Steenbergen G., Reniers A.* Shoaling and shoreline dissipation of low-frequency waves // Journal of Geophysical Research. II 2007. 112, C2. C02011.

*Dongeren Ap van, Plant Nathaniel, Cohen Anna, Roelvink Dano, Haller Merrick C., Catalán Patricio.* Beach Wizard: Nearshore bathymetry estimation through assimilation of model computations and remote observations // Coastal Engineering. XII 2008. 55, 12. 1016–1027.

*Doria André, Guza R.T., O'Reilly William C., Yates M.L.* Observations and modeling of San Diego beaches during El Niño // Continental Shelf Research. VIII 2016. 124. 153–164.

*Dusseljee Daniel, Klopman Gert, Van Vledder Gerbrant, Riezebos Hendrik Jan.* IMPACT OF HARBOR NAVIGATION CHANNELS ON WAVES: A NUMERICAL MODELLING GUIDELINE // Coastal Engineering Proceedings. XII 2014. 1, 34. 58.

SURFACE WAVES ON WATER OF VARIABLE DEPTH. // . 1951.

*Elgar Steve, Guza R. T.* Observations of bispectra of shoaling surface gravity waves // Journal of Fluid Mechanics. 1985.

*Elgar Steve, Guza R. T., Raubenheimer B., Herbers T. H. C., Gallagher Edith L.* Spectral evolution of shoaling and breaking waves on a barred beach // Journal of Geophysical Research: Oceans. VII 1997. 102, C7. 15797–15805.

*Elgar Steve, Herbers T. H. C., Guza R. T.* Reflection of Ocean Surface Gravity Waves from a Natural Beach // Journal of Physical Oceanography. VII 1994. 24, 7. 1503–1511.

Observations of infragravity waves. // . 1992. 5.

*Elgar Steve, Raubenheimer Britt, Guza R T.* Quality control of acoustic Doppler velocimeter data in the surfzone // Measurement Science and Technology. X 2005. 16, 10. 1889–1893.

*FEMA* . Guidance for Flood Risk Analysis and Mapping - Coastal Wave Runup and Overtopping. XI 2021.

*Fiedler Julia W., Kim Lauren, Grenzeback Robert, Young Adam, Merrifield Mark A.* Enhanced Surf Zone and Wave Runup Observations with Hovering Drone-Mounted Lidar // Journal of Atmospheric and Oceanic Technology. XI 2021. 38, 11. 1967–1978.

*Fiedler Julia W., Smit Pieter B., Brodie Katherine L., McNinch Jesse, Guza R.T.* Numerical modeling of wave runup on steep and mildly sloping natural beaches // Coastal Engineering. I 2018. 131. 106–113.

*Fiedler Julia W., Smit Pieter B., Brodie Katherine L., McNinch Jesse, Guza R.T.* The offshore boundary condition in surf zone modeling // Coastal Engineering. I 2019. 143. 12–20.

*Fiedler Julia W., Young Adam P., Ludka Bonnie C., O'Reilly William C., Henderson Cassandra, Merrifield Mark A., Guza R. T.* Predicting site-specific storm wave run-up // Natural Hazards. X 2020. 104, 1. 493–517.

*Gallagher Brent.* Generation of surf beat by non-linear wave interactions // Journal of Fluid Mechanics. IX 1971. 49, 1. 1–20.

*Gallagher Edith L., Elgar Steve, Guza R. T.* Observations of sand bar evolution on a natural beach // Journal of Geophysical Research: Oceans. II 1998. 103, C2. 3203–3215.

*Gallien T.W.* Validated coastal flood modeling at Imperial Beach, California: Comparing total water level, empirical and numerical overtopping methodologies // Coastal

Engineering. V 2016. 111. 95–104.

*Gao Jay.* Bathymetric mapping by means of remote sensing: methods, accuracy and limitations // Progress in Physical Geography: Earth and Environment. II 2009. 33, 1. 103–116.

*Geyman Emily C., Maloof Adam C.* A Simple Method for Extracting Water Depth From Multispectral Satellite Imagery in Regions of Variable Bottom Type // Earth and Space Science. III 2019. 6, 3. 527–537.

*Gomes Esther R., Mulligan Ryan P., Brodie Katherine L., McNinch Jesse E.* Bathymetric control on the spatial distribution of wave breaking in the surf zone of a natural beach // Coastal Engineering. X 2016. 116. 180–194.

*Guimarães Pedro Veras, Farina Leandro, Toldo Elirio, Diaz-Hernandez Gabriel, Akhmatskaya Elena.* Numerical simulation of extreme wave runup during storm events in Tramandaí Beach, Rio Grande do Sul, Brazil // Coastal Engineering. I 2015. 95. 171–180.

*Guza R. T., Thornton Edward B.* Swash oscillations on a natural beach // Journal of Geophysical Research. 1982. 87, C1. 483.

*Guza R. T., Thornton Edward B.* Observations of surf beat // Journal of Geophysical Research. 1985. 90, C2. 3161.

*Hasselmann K.* On the non-linear energy transfer in a gravity-wave spectrum Part 1. General theory // Journal of Fluid Mechanics. IV 1962. 12, 04. 481.

*Hasselmann K., Munk W. H., MacDonald Gordon.* Bispectra of Ocean Waves. 1963.

*Henderson Cassandra S., Fiedler Julia W., Merrifield Mark A., Guza R.T., Young Adam P.* Phase resolving runup and overtopping field validation of SWASH // Coastal Engineering. VIII 2022. 175. 104128.

*Henderson Stephen M., Guza R. T., Elgar Steve, Herbers T. H. C., Bowen A. J.* Nonlinear generation and loss of infragravity wave energy // Journal of Geophysical Research. XII 2006. 111, C12. C12007.

*Herbers T. H. C., Burton M. C.* Nonlinear shoaling of directionally spread waves on a beach // Journal of Geophysical Research: Oceans. IX 1997. 102, C9. 21101–21114.

*Herbers T. H. C., Elgar Steve, Guza R. T.* Generation and propagation of infragravity waves // Journal of Geophysical Research. 1995a. 100, C12. 24863.

*Herbers T. H. C., Elgar Steve, Guza R. T., O'Reilly W. C.* Infragravity-Frequency (0.005–0.05 Hz) Motions on the Shelf. Part II Free Waves // Journal of Physical Oceanography. 1995b. 1063–1079.

*Herbers T. H. C., Guza R. T.* Infragravity-Frequency (0.005–0.05 Hz) Motions on the Shelf. Part I Forced Waves // Journal of Physical Oceanography. 1994.

*Hodúl Matúš, Bird Stephen, Knudby Anders, Chénier René.* Satellite derived photogrammetric bathymetry // ISPRS Journal of Photogrammetry and Remote Sensing. VIII 2018. 142. 268–277.

*Hoefel F.* Wave-Induced Sediment Transport and Sandbar Migration // Science. III 2003. 299, 5614. 1885–1887.

*Holland T.K.* Application of the linear dispersion relation with respect to depth inversion and remotely sensed imagery // IEEE Transactions on Geoscience and Remote Sensing. IX 2001. 39, 9. 2060–2072.

*Holman R. A., Sallenger A. H.* Setup and swash on a natural beach // Journal of Geophysical Research. 1985. 90, C1. 945.

*Holman R.A.* Extreme value statistics for wave run-up on a natural beach // Coastal Engineering. III 1986. 9, 6. 527–544.

*Holman R.A., Stanley J.* The history and technical capabilities of Argus // Coastal Engineering. VI 2007. 54, 6-7. 477–491.

*Holman Rob, Bergsma Erwin W. J.* Updates to and Performance of the cBathy Algorithm for Estimating Nearshore Bathymetry from Remote Sensing Imagery // Remote Sensing. X 2021. 13, 19. 3996.

*Holman Rob, Haller Merrick C.* Remote Sensing of the Nearshore // Annual Review of Marine Science. I 2013. 5, 1. 95–113.

*Holman Rob, Plant Nathaniel, Holland Todd.* cBathy: A robust algorithm for estimating nearshore bathymetry: The cBathy Algorithm // Journal of Geophysical Research: Oceans. V 2013. 118, 5. 2595–2609.

*Holman Rob, Sallenger Asbury, Lippmann Tom, Haines John.* The Application of Video Image Processing to the Study of Nearshore Processes // Oceanography. 1993. 6, 3. 78–85.

*Hughes Michael G., Aagaard Troels, Baldock Tom E., Power Hannah E.* Spectral signatures for swash on reflective, intermediate and dissipative beaches // Marine Geology. IX

2014. 355. 88–97.

*Hughes Michael G., Baldock Tom E., Aagaard Troels.* Swash saturation: an assessment of available models // Ocean Dynamics. VII 2018. 68, 7. 911–922.

*Hunt Ira A.* Design of seawalls and breakwaters // Journal of the Waterways and Harbors Division. 1959. 85, 3. 123.

*Huntley D. A.* Long-period waves on a natural beach // Journal of Geophysical Research. XII 1976. 81, 36. 6441–6449.

*Huntley D. A., Guza R. T., Bowen A. J.* A universal form for shoreline run-up spectra? // Journal of Geophysical Research. VI 1977. 82, 18. 2577–2581.

*Huntley D. A., Guza R. T., Thornton E. B.* Field observations of surf beat: 1. Progressive edge waves // Journal of Geophysical Research. 1981. 86, C7. 6451.

*Inman D. L., Tait R. J., Nordstrom C. E.* Mixing in the surf zone // Journal of Geophysical Research. V 1971. 76, 15. 3493–3514.

*Irish J.L., White T.E.* Coastal engineering applications of high-resolution lidar bathymetry // Coastal Engineering. X 1998. 35, 1-2. 47–71.

*Jing Enjie, Datt Bisun.* Detection of coastal bathymetry using hyperspectral imagery // OCEANS'10 IEEE SYDNEY. Sydney, Australia: IEEE, V 2010. 1–4.

*Jordi Antoni, Georgas Nickitas, Blumberg Alan, Yin Larry, Chen Ziyu, Wang Yifan, Schulte Justin, Ramaswamy Venkatsundar, Runnels Dave, Saleh Firas.* A Next-Generation Coastal Ocean Operational System: Probabilistic Flood Forecasting at Street Scale // Bulletin of the American Meteorological Society. I 2019. 100, 1. 41–54.

*Kim Y. C., Beall J. M., Powers E. J., Miksad R. W.* Bispectrum and nonlinear wave coupling // Physics of Fluids. 1980. 23, 2. 258.

*Kuik A.J.* A Method for the Routine Analysis of Pitch-and-Roll Buoy Wave Data. 1988.

*Kulp Scott A., Strauss Benjamin H.* New elevation data triple estimates of global vulnerability to sea-level rise and coastal flooding // Nature Communications. XII 2019. 10, 1. 4844.

*Lange Athina M.Z., Fiedler Julia W., Becker Janet M., Merrifield Mark A., Guza R.T.* Estimating runup with limited bathymetry // Coastal Engineering. III 2022. 172. 104055.

*Larson Magnus, Kraus Nicholas C.* Temporal and spatial scales of beach profile change, Duck, North Carolina // Marine Geology. III 1994. 117, 1-4. 75–94.

*Legleiter Carl J., Harrison Lee R.* Remote Sensing of River Bathymetry: Evaluating a Range of Sensors, Platforms, and Algorithms on the Upper Sacramento River, California, USA // Water Resources Research. III 2019. 55, 3. 2142–2169.

*Li Jiwei, Knapp David E., Schill Steven R., Roelfsema Chris, Phinn Stuart, Silman Miles, Mascaro Joseph, Asner Gregory P.* Adaptive bathymetry estimation for shallow coastal waters using Planet Dove satellites // Remote Sensing of Environment. X 2019. 232. 111302.

*Li Shaowu, Liao Zhiling, Liu Ye, Zou Qingping.* Evolution of Infragravity Waves Over a Shoal Under Nonbreaking Conditions // Journal of Geophysical Research: Oceans. VIII 2020. 125, 8.

Phase Speed and Angle of Breaking Waves Measured with Video Techniques. // . 1. 1991. 542–556.

*Lippmann T C, Holman R A.* Quantification of sand bar morphology: A video technique based on wave dissipation // Journal of Geophysical Research. 1989. 94. 17.

*List Jeffrey H.* Wave Groupiness as a Source of Nearshore Long Waves // COASTAL ENGINEERING. 1986. 15.

*Liu Ye, Liao Zhiling, Fang Kezhao, Li Shaowu.* Uncertainty of wave runup prediction on coral reef-fringed coasts using SWASH model // Ocean Engineering. XII 2021. 242. 110094.

*Longuet-Higgins M. S., Stewart R. W.* Radiation stress and mass transport in gravity waves, with application to 'surf beats' // Journal of Fluid Mechanics. VIII 1962. 13, 4. 481–504.

*Longuet-Higgins M S, Stewart R W.* Radiation stresses in water waves; a physical discussion, with applications // Deep Sea Research. 1964. 11. 529–562.

*Ludka B. C., Guza R. T., O'Reilly W. C., Merrifield M. A., Flick R. E., Bak A. S., Hesser T., Bucciarelli R., Olfe C., Woodward B., Boyd W., Smith K., Okihiro M., Grenzeback R., Parry L., Boyd G.* Sixteen years of bathymetry and waves at San Diego beaches // Scientific Data. XII 2019. 6, 1. 161.

*Ma Sheng, Tao Zui, Yang Xiaofeng, Yu Yang, Zhou Xuan, Li Ziwei.* Bathymetry Retrieval From Hyperspectral Remote Sensing Data in Optical-Shallow Water // IEEE Transactions on Geoscience and Remote Sensing. II 2014. 52, 2. 1205–1212.

*Maas H.-G., Mader D., Richter K., Westfeld P.* IMPROVEMENTS IN LIDAR BATHYMETRY DATA ANALYSIS // The International Archives of the Photogrammetry, Remote Sensing and Spatial Information Sciences. IV 2019. XLII-2/W10. 113–117.

*Mallet Clément, Bretar Frédéric.* Full-waveform topographic lidar: State-of-the-art // ISPRS Journal of Photogrammetry and Remote Sensing. I 2009. 64, 1. 1–16.

*Martins K., Blenkinsopp C. E., Deigaard R., Power H. E.* Energy Dissipation in the Inner Surf Zone: New Insights From Li DAR -Based Roller Geometry Measurements // Journal of Geophysical Research: Oceans. V 2018. 123, 5. 3386–3407.

*Martins Kévin, Bonneton Philippe, Viron Olivier de, Turner Ian L., Harley Mitchel D., Splinter Kristen.* New Perspectives for Nonlinear Depth-Inversion of the Nearshore Using Boussinesq Theory // Geophysical Research Letters. I 2023. 50, 2.

*Mather Andrew, Stretch Derek, Garland Gerald.* Predicting Extreme Wave Run-Up on Natural Beaches for Coastal Planning and Management // Coastal Engineering Journal. VI 2011. 53, 2. 87–109.

*Merrifield M. A., Johnson Mele, Guza R T, Fiedler Julia W., Young Adam P., Henderson Cassandra, Lange Athina M.Z., O'Reilly W C, Ludka Bonnie C., Okihiro Michele, Pappas Kyle, Engeman Laura, Behrens James, Terrill Eric.* An early warning system for wave-driven coastal flooding at Imperial Beach, CA // Natural Hazards. 2021.

Le pouvoir reflechissant des ouvrages maritimes exposes a l'action de la houle. // . 1951.

*Munk W. H.* Surf beats // Transactions, American Geophysical Union. 1949. 30, 6. 849.

*Nicolae Lerma Alexandre, Pedreros Rodrigo, Robinet Arthur, Sénéchal Nadia.* Simulating wave setup and runup during storm conditions on a complex barred beach // Coastal Engineering. V 2017. 123. 29–41.

Energy transfer between short wave groups and bound long waves on a plane slope. // . 2003.

*O'Grady J. G., McInnes K. L., Hemer M. A., Hoeke R. K., Stephenson A. G., Colberg F.* Extreme Water Levels for Australian Beaches Using Empirical Equations for Shoreline Wave Setup // Journal of Geophysical Research: Oceans. VIII 2019. 124, 8. 5468–5484.

*O'Reilly W.C., Olfe Corey B., Thomas Julianna, Seymour R.J., Guza R.T.* The California coastal wave monitoring and prediction system // Coastal Engineering. X 2016. 116. 118–132.

*Okihiro Michele, Guza R. T.* Infragravity energy modulation by tides // Journal of Geophysical Research. 1995. 100, C8. 16143.

*Okihiro Michele, Guza R. T., Seymour R. J.* Bound Infragravity Waves // Journal of Geophysical Research. 1992. 97, C7. 11453–11469.

*Okihiro Michele, Guza R. T., Seymour R. J.* Excitation of seiche observed in a small harbor // Journal of Geophysical Research. 1993. 98, C10. 18201.

*Oltman-Shay Joan, Guza R. T.* Infragravity Edge Wave Observations on Two California Beaches.pdf. 1987.

*Oltman-Shay Joan, Howd Peter A.* Edge waves on nonplanar bathymetry and alongshore currents: A model and data comparison // Journal of Geophysical Research: Oceans. II 1993. 98, C2. 2495–2507.

*Oorschot J H van, d'Angremond K.* The Effect of Wave Energy Spectra on Wave Run-up // Coastal Engineering. 1968. 11th International Conference on Coastal Engineering. 13.

*Plant Nathaniel G., Edwards Kacey L., Kaihatu James M., Veeramony Jayaram, Hsu Larry, Holland K. Todd.* The effect of bathymetric filtering on nearshore process model results // Coastal Engineering. IV 2009. 56, 4. 484–493.

*Power H. E., Hughes M. G., Aagaard T., Baldock T. E.* Nearshore wave height variation in unsaturated surf // Journal of Geophysical Research. VIII 2010. 115, C8. C08030.

*Qin Lingyu, Li Ying.* Significant Wave Height Estimation Using Multi-Satellite Observations from GNSS-R // Remote Sensing. XI 2021. 13, 23. 4806.

*Radermacher Max, Wengrove Meagan, Vries Jaap van Thiel de, Holman Rob.* Applicability of video-derived bathymetry estimates to nearshore current model predictions // Journal of Coastal Research. IV 2014. 70. 290–295.

*Ranasinghe Roshanka, McLoughlin Rodney, Short Andrew, Symonds Graham.* The Southern Oscillation Index, wave climate, and beach rotation // Marine Geology. III 2004. 204, 3-4. 273–287.

*Raubenheimer B., Guza R. T., Elgar Steve.* Wave transformation across the inner surf zone // Journal of Geophysical Research: Oceans. XI 1996. 101, C11. 25589–25597.

*Raubenheimer B., Guza R. T., Elgar Steve.* Field observations of wave-driven setdown and setup // Journal of Geophysical Research: Oceans. III 2001. 106, C3. 4629–4638.

*Rawat Arshad, Ardhuin Fabrice, Ballu Valérie, Crawford Wayne, Corela Carlos, Aucan*

*Jerome*. Infragravity waves across the oceans: Following Infra-Gravity Wave Bursts // Geophysical Research Letters. XI 2014. 41, 22. 7957–7963.

*Reniers A. J. H. M.* Linear modeling of infragravity waves during Delilah // Journal of Geophysical Research. 2002. 107, C10. 3137.

*Reniers Ad J.H.M., Naporowski Remy, Tissier Marion F. S., Schipper Matthieu A. de, Akrish Gal, Rijnsdorp Dirk P.* North Sea Infragravity Wave Observations // Journal of Marine Science and Engineering. I 2021. 9, 2. 141.

*Rhie Junkee, Romanowicz Barbara*. A study of the relation between ocean storms and the Earth's hum: OCEAN STORMS AND EARTH'S HUM // Geochemistry, Geophysics, Geosystems. X 2006. 7, 10. n/a–n/a.

*Ribal Agustinus, Young Ian R.* 33 years of globally calibrated wave height and wind speed data based on altimeter observations // Scientific Data. V 2019. 6, 1. 77.

*Rijnsdorp Dirk P., Reniers Ad J. H. M., Zijlema Marcel*. Free Infragravity Waves in the North Sea // Journal of Geophysical Research: Oceans. VIII 2021. 126, 8.

*Rijnsdorp Dirk P., Ruessink Gerben, Zijlema Marcel*. Infragravity-wave dynamics in a barred coastal region, a numerical study // Journal of Geophysical Research: Oceans. VI 2015. 120, 6. 4068–4089.

*Rijnsdorp Dirk P., Smit Pieter B., Zijlema Marcel*. Non-hydrostatic modelling of infragravity waves under laboratory conditions // Coastal Engineering. III 2014. 85. 30–42.

*Rodríguez-Padilla Isaac, Castelle Bruno, Marieu Vincent, Morichon Denis*. Video-Based Nearshore Bathymetric Inversion on a Geologically Constrained Mesotidal Beach during Storm Events // Remote Sensing. VIII 2022. 14, 16. 3850.

*Roelvink Dano, McCall Robert, Mehvar Seyedabdolhossein, Nederhoff Kees, Dastgheib Ali*. Improving predictions of swash dynamics in XBeach: The role of groupiness and incident-band runup // Coastal Engineering. IV 2018. 134. 103–123.

*Roelvink Dano, Reniers Ad, Van Dongeren Ap, Van Thiel De Vries Jaap, McCall Robert, Lescinski Jamie*. Modelling storm impacts on beaches, dunes and barrier islands // Coastal Engineering. XI 2009. 56, 11-12. 1133–1152.

*Ronneberger Olaf, Fischer Philipp, Brox Thomas*. U-Net: Convolutional Networks for Biomedical Image Segmentation // arXiv:1505.04597 [cs]. V 2015. arXiv: 1505.04597.

*Ruessink B. G.* Bound and free infragravity waves in the nearshore zone under breaking

and nonbreaking conditions // Journal of Geophysical Research: Oceans. VI 1998. 103, C6. 12795–12805.

*Ruessink Gerben, Michallet Hervé, Bonneton Philippe, Mouazé Dominique, Lara Javier L, Silva Paulo A, Wellens Peter.* GLOBEX: WAVE DYNAMICS ON A GENTLY SLOPING LABORATORY BEACH // Coastal Dynamics. 2013. 12.

*Ruggiero Peter.* Wave run-up on a high-energy dissipative beach // Journal of Geophysical Research. 2004. 109, C6. C06025.

*Ruggiero Peter, Kaminsky George M., Gelfenbaum Guy, Cohn Nicholas.* Morphodynamics of prograding beaches: A synthesis of seasonal- to century-scale observations of the Columbia River littoral cell // Marine Geology. VI 2016. 376. 51–68.

*Ruju Andrea, Lara Javier L., Losada Inigo J.* Radiation stress and low-frequency energy balance within the surf zone: A numerical approach // Coastal Engineering. X 2012. 68. 44–55.

*Ruju Andrea, Lara Javier L., Losada Inigo J.* Numerical analysis of run-up oscillations under dissipative conditions // Coastal Engineering. IV 2014. 86. 45–56.

*Ruju Andrea, Lara Javier L., Losada Inigo J.* Numerical Assessment of Infragravity Swash Response to Offshore Wave Frequency Spread Variability // Journal of Geophysical Research: Oceans. IX 2019. 124, 9. 6643–6657.

*Rutten Jantien, Jong Steven M. de, Ruessink Gerben.* Accuracy of Nearshore Bathymetry Inverted From ${X}$ -Band Radar and Optical Video Data // IEEE Transactions on Geoscience and Remote Sensing. II 2017. 55, 2. 1106–1116.

*Salameh Edward, Frappart Frédéric, Almar Rafael, Baptista Paulo, Heygster Georg, Lubac Bertrand, Raucoules Daniel, Almeida Luis, Bergsma Erwin, Capo Sylvain, De Michele Marcello, Idier Deborah, Li Zhen, Marieu Vincent, Poupardin Adrien, Silva Paulo, Turki Imen, Laignel Benoit.* Monitoring Beach Topography and Nearshore Bathymetry Using Spaceborne Remote Sensing: A Review // Remote Sensing. IX 2019. 11, 19. 2212.

*Sandidge Juanita C., Holyer Ronald J.* Coastal Bathymetry from Hyperspectral Observations of Water Radiance // Remote Sensing of Environment. IX 1998. 65, 3. 341–352.

*Senechal Nadia, Coco Giovanni, Bryan Karin R., Holman Rob A.* Wave runup during extreme storm conditions // Journal of Geophysical Research. VII 2011. 116, C7. C07032.

*Seymour Richard, Guza R.T., O'Reilly William, Elgar Steve.* Rapid erosion of a small

southern California beach fill // Coastal Engineering. II 2005. 52, 2. 151–158.

*Sheremet A., Guza R T, Elgar Steve, Herbers T. H. C.* Observations of nearshore infragravity waves: Seaward and shoreward propagating components // Journal of Geophysical Research. 2002. 107, C8. 3095.

*Silva Paula Gomes da, Coco Giovanni, Garnier Roland, Klein Antonio H.F.* On the prediction of runup, setup and swash on beaches // Earth-Science Reviews. V 2020. 204. 103148.

*Silva Paula Gomes da, Medina Raúl, González Mauricio, Garnier Roland.* Wave reflection and saturation on natural beaches: The role of the morphodynamic beach state in incident swash // Coastal Engineering. XI 2019. 153. 103540.

*Smit P. B., Janssen T. T., Herbers T. H. C., Taira T., Romanowicz B. A.* Infragravity Wave Radiation Across the Shelf Break // Journal of Geophysical Research: Oceans. VII 2018. 123, 7. 4483–4490.

*Smit Pieter, Zijlema Marcel, Stelling Guus.* Depth-induced wave breaking in a non-hydrostatic, near-shore wave model // Coastal Engineering. VI 2013. 76. 1–16.

*Stephens Elisabeth, Cloke Hannah.* Improving flood forecasts for better flood preparedness in the UK (and beyond): Commentary // The Geographical Journal. XII 2014. 180, 4. 310–316.

*Stephens Scott A., Coco Giovanni, Bryan Karin R.* Numerical Simulations of Wave Setup over Barred Beach Profiles: Implications for Predictability // Journal of Waterway, Port, Coastal, and Ocean Engineering. VII 2011. 137, 4. 175–181.

*Stive M J F.* VELOCITY AND PRESSURE FIELD OF SPILLING BREAKERS // COASTAL ENGINEERING. 1980. 20.

*Stockdon Hilary F., Holman Rob A.* Estimation of wave phase speed and nearshore bathymetry from video imagery // Journal of Geophysical Research: Oceans. IX 2000. 105, C9. 22015–22033.

*Stockdon Hilary F., Holman Rob A., Howd Peter A., Sallenger Asbury H.* Empirical parameterization of setup, swash, and runup // Coastal Engineering. V 2006. 53, 7. 573–588.

*Stokes Kit, Poate Tim, Masselink Gerd.* DEVELOPMENT OF A REAL-TIME, REGIONAL COASTAL FLOOD WARNING SYSTEM FOR SOUTHWEST ENGLAND // Coastal Sediments 2019. Tampa/St. Petersburg, Florida, USA: WORLD SCIENTIFIC, V 2019. 1460–1474.

*Stokes Kit, Poate Tim, Masselink Gerd, King Erin, Saulter Andrew, Ely Nick.* Forecasting coastal overtopping at engineered and naturally defended coastlines // Coastal Engineering. III 2021. 164. 103827.

*Stringari C. E., Power H. E.* The Fraction of Broken Waves in Natural Surf Zones // Journal of Geophysical Research: Oceans. XII 2019. 124, 12. 9114–9140.

*Stringari C.E., Harris D.L., Power H.E.* A novel machine learning algorithm for tracking remotely sensed waves in the surf zone // Coastal Engineering. V 2019. 147. 149–158.

*Suhayda J. N.* Standing waves on beaches // Journal of Geophysical Research. VII 1974. 79, 21. 3065–3071.

*Suhayda Joseph N., Pettigrew Neal R.* Observations of wave height and wave celerity in the surf zone // Journal of Geophysical Research. III 1977. 82, 9. 1419–1424.

*Suzuki Tomohiro, Altomare Corrado, Veale William, Verwaest Toon, Trouw Koen, Troch Peter, Zijlema Marcel.* Efficient and robust wave overtopping estimation for impermeable coastal structures in shallow foreshores using SWASH // Coastal Engineering. IV 2017. 122. 108–123.

*Svendsen Ib A, Buhr Hansen J.* Deformation up to Breaking of Periodic Waves on a Beach // Proceedings, 15th International Conference on Coastal Engineering. 1976. 520–539.

*Svendsen Ib A, Qin Wenkai, Ebersole Bruce A.* Modelling waves and currents at the LSTF and other laboratory facilities // Coastal Engineering. XI 2003. 50, 1-2. 19–45.

*Szeliski Richard.* Computer Vision: Algorithms and Applications, 2nd Edition. I 2022. 2.

*Sénéchal N, Dupuis H, Bonneton P.* Preliminary hydrodynamic results of a field experiment on a barred beach, True Vert beach on October 2001 // Ocean Dynamics. 2004. 54. 408–414.

*Thomson Jim, Elgar Steve, Raubenheimer Britt, Herbers T. H. C., Guza R. T.* Tidal modulation of infragravity waves via nonlinear energy losses in the surfzone // Geophysical Research Letters. 2006. 33, 5. L05601.

*Thornton E. B., Humiston R. T., Birkemeier W.* Bar/trough generation on a natural beach // Journal of Geophysical Research: Oceans. V 1996. 101, C5. 12097–12110.

*Thornton Edward B., Guza R. T.* Energy saturation and phase speeds measured on a natural beach // Journal of Geophysical Research. 1982. 87, C12. 9499.

*Thuan Duong Hai, Almar Rafael, Marchesiello Patrick, Viet Nguyen Trung.* Video Sensing

of Nearshore Bathymetry Evolution with Error Estimate // Journal of Marine Science and Engineering. VII 2019. 7, 7. 233.

*Tissier M., Bonneton P., Michallet H., Ruessink B. G.* Infragravity-wave modulation of short-wave celerity in the surf zone // Journal of Geophysical Research: Oceans. X 2015. 120, 10. 6799–6814.

*Torres-Freyermuth Alec, Lara Javier L., Losada Inigo J.* Numerical modelling of short- and long-wave transformation on a barred beach // Coastal Engineering. III 2010. 57, 3. 317–330.

*Trombetta T.B., Marques W.C., Guimarães R.C., Costi J.* An overview of longshore sediment transport on the Brazilian coast // Regional Studies in Marine Science. III 2020. 35. 101099.

*Tsukada Fumiya, Shimozono T., Matsuba Y.* UAV-based mapping of nearshore bathymetry over broad areas // Coastal Engineering Journal. IV 2020. 62, 2. 285–298.

*Tucker M.J.* Surf beats: sea waves of 1 to 5 min. period // Proceedings of the Royal Society of London. Series A. Mathematical and Physical Sciences. VIII 1950. 202, 1071. 565–573.

*USGS* . Total Water Level and Coastal Change Forecast Viewer. 2022.

*Usuyama Naoto.* Simple PyTorch implementations of U-Net/FullyConvNet (FCN) for image segmentation. GitHub, 2018.

*Van Thiel De Vries J.S.M., Van Gent M.R.A., Walstra D.J.R., Reniers A.J.H.M.* Analysis of dune erosion processes in large-scale flume experiments // Coastal Engineering. XII 2008. 55, 12. 1028–1040.

*Vanderstraete Tony, Goossens Rudi, Ghabour T.K.* Remote sensing as a tool for bathymetric mapping of coral reefs in the Red Sea (Hurghada – Egypt) // Belgeo. IX 2003. 3. 257–268.

*Vousdoukas Michalis Ioannis, Wziatek Dagmara, Almeida Luis Pedro.* Coastal vulnerability assessment based on video wave run-up observations at a mesotidal, steep-sloped beach // Ocean Dynamics. I 2012. 62, 1. 123–137.

*Webb Spahr C.* The Earth's 'hum' is driven by ocean waves over the continental shelves // Nature. II 2007. 445, 7129. 754–756.

Infragravity waves in the deep ocean. // . 1991. 14.

*Wengrove Meagan E, Henriquez Martijn, Schipper Matthieu A de, Holman Rob, Stive M J F.* MONITORING MORPHOLOGY OF THE SAND ENGINE LEESIDE USING ARGUS' cBATHY // Coastal Dynamics. 2013. 13.

Overview of seasonal sand level changes on southern California beaches. // . 2009. 77, 1.

*Yoo Jeseon, Fritz Hermann M., Haas Kevin A., Work Paul A., Barnes Christopher F.* Depth Inversion in the Surf Zone with Inclusion of Wave Nonlinearity Using Video-Derived Celerity // Journal of Waterway, Port, Coastal, and Ocean Engineering. III 2011. 137, 2. 95–106.

*Young Adam P., Flick Reinhard E., Gallien Timu W., Giddings Sarah N., Guza R. T., Harvey M., Lenain Luc, Ludka B. C., Melville W. Kendall, O'Reilly W. C.* Southern California Coastal Response to the 2015–2016 El Niño // Journal of Geophysical Research: Earth Surface. XI 2018. 123, 11. 3069–3083.

*Zhang Qinghui, Toorman Erik A., Monbaliu Jaak.* Shoaling of bound infragravity waves on plane slopes for bichromatic wave conditions // Coastal Engineering. VI 2020. 158. 103684.

*Zheng Zhenjun, Ma Xiaozhou, Ma Yuxiang, Huang Xuezhi, Dong Guohai.* Modeling of coastal infragravity waves using the spectral model WAVEWATCH // Coastal Engineering. XII 2021. 170. 104016.

*Zijlema Marcel.* MODELLING WAVE TRANSFORMATION ACROSS A FRINGING REEF USING SWASH // Coastal Engineering Proceedings. X 2012. 1, 33. 26.

*Zijlema Marcel, Stelling Guus, Smit Pieter.* SWASH: An operational public domain code for simulating wave fields and rapidly varied flows in coastal waters // Coastal Engineering. X 2011. 58, 10. 992–1012.

*Zuckerman Seth, Anderson Steven.* Bathymetry and Water-Level Estimation Using X-Band Radar at a Tidal Inlet // Journal of Coastal Research. IX 2018. 345. 1227–1235.